Dynamic Line-by-line Pulse Shaping

by

John Thomas Willits

B.S., University of Colorado, Engineering Physics, 2004

M.S., University of Colorado, Electrical Engineering, 2008

A thesis submitted to the

Faculty of the Graduate School of the

University of Colorado in partial fulfillment

of the requirement for the degree of

Doctor of Philosophy

Department of Electrical Engineering

2012

This thesis entitled:
Dynamic Line-by-line Pulse Shaping
written by John Thomas Willits
has been approved for the Department of Electrical Engineering

_____
Prof. Steven Cundiff

_____
Prof. Milos Popovic

Date_____

The final copy of this thesis has been examined by the signatories, and we find that both the content and the form meet acceptable presentation standards of scholarly work in the above mentioned discipline

Willits, John (Ph.D., Electrical Engineering)

Dynamic Line-by-line Pulse Shaping

Thesis directed by Prof. Steven Cundiff

Abstract

In pursuit of optical arbitrary waveform generation (OAWG), line-by-line pulse shapers use dynamic masks that can be modulated at the repetition rate of an input pulse train. The pulse-to-pulse control of the output pulse train with the waveform fidelity provided by line-by-line pulse shaping creates the most arbitrary waveform output possible, OAWG. This thesis studies the theoretical dynamic effects of such a pulse shaper and presents efforts towards realization of OAWG. Pulse shaping theory is extended to include rapid waveform update for line-by-line pulse shaping. The fundamental tradeoff between response speed and waveform fidelity is illustrated by several examples. Line-by-line pulse shaping is demonstrated at a repetition rate of 890 MHz on a mode-locked titanium sapphire laser. This pulse shaper relies on a virtual imaged phased array (VIPA) to obtain the necessary high spectral resolution. The details of the VIPA's ideal and nonideal performance are analyzed, simulated and tested. Individual frequency modes from the mode-locked titanium sapphire laser are also resolved using the same VIPA paired with a diffraction grating creating a 2-D spectral brush with a resolution of 357 MHz. The advantages and nonideal effects of VIPA-based pulse shaping are investigated. Analysis of several high speed modulation techniques are explored. The optical system required to separate adjacent comb lines into different

single mode (SM) fibers necessary for several modulation techniques is designed and tested.

**Dedication**

To my wife and parents,
for their endless love and support.

## Acknowledgements

This work would not have been possible without wonderful support of many instructors, technical wizards, and lab mates.

First and foremost, I would like to thank my advisor Steven Cundiff for his continued support through the many challenges of this project. Every week we would meet for project meetings where he always had excellent suggestions and directions to take this project. All the while helping me to become a better scientist by encouraging, supporting, and when necessary correcting my ideas.

JILA has excellent technical support. I'd like to thank Dave Alchenberger in the special techniques shop for his help in creating custom mirror masks and lithium niobate waveguides, as well as Terry Brown who helped design and build a power supply for high speed gain chips. It was also very useful to have a staff of machinists on hand to answer questions about exactly how to construct a specific mount I'm building. Kevin Silverman at NIST helped design and grew the saturable Bragg reflector discussed in this thesis.

Andrew Weiner's insights into the details of how a VIPA works was invaluable to this project. During his stay here at JILA he worked closely with me on this project designing and modeling the VIPA that is the heart of the high spectral resolution pulse shaper.

I'd also like to thank everyone in Cundiff's group. Although many of us work on completely separate projects, there are many times that some technical issue needs to be worked out and discussing the problem with others in the lab has led to very effective solutions. For instance, Jared Wahlstrand helped in analyzing the response of the saturable Bragg mirror using a pump-probe experiment. Galan Moody assisted me in measuring spectrum of the pulse shaper

output using a high resolution monochromator. Ryan Smith listened to many of the challenges of the project and offered excellent advice (often over lunch while playing chess = Chunch). Soobong Choi helped in the design and development of a high speed modulator array. Thanks again to everyone for their assistance with this project.

# Table of Contents

# Chapter 1

# Introduction

## 1.1 Overview

The ability to manipulate the shape of broadband optical pulses has impacted many fields such as coherent control of chemical processes, high field physics, nonlinear fiber optics, and ultrafast spectroscopy [1]. Many methods have been invented to shape pulses, but the most widespread and general method for pulse shaping is spectral decomposition. In this method, the spectral components of the laser pulses are spatially dispersed using an element such as a grating, and then a mask is applied to modify the phase and/or amplitude of each component. Finally, the components are recombined to reconstruct the new, modified pulses [1]. Using high resolution spectral dispersers such as a virtually imaged phased-array (VIPA) [2], the individual frequency modes that comprise the spectral comb produced by a mode-locked laser can be resolved [3]. In this regime one can fully control the shape of a stream of pulses with line-by-line pulse shaping [4,5].

Line-by-line pulse shaping is an important step toward optical arbitrary waveform generation (OAWG) [6,7], where the spectral mask is updated at the repetition rate of the input laser in addition to resolving individual comb lines (note that some authors use “static OAWG” to designate line-by-line shaping and “dynamic OAWG” to designate the more difficult goal of updating the mask for every input pulse). The ability to perform line-by-line pulse shaping on the output of a mode-locked laser has been enabled by the development of femtosecond comb techniques [8,9]. As elaborated in section 2.4 by stabilizing $f_{rep}$ and the offset frequency, $f_0$, of a femtosecond comb source, the frequency brush can be made stable enough to perform line-by-

line pulse shaping. Substantial progress has been made towards OAWG [10,11], although it has not been demonstrated yet due to the difficulty of simultaneously achieving high spectral resolution and high modulation rate. To balance these two extremes a 890 MHz repetition rate mode-locked titanium sapphire laser is used in this thesis, providing a high enough repetition rate that adjacent frequency modes can be separately controlled, yet low enough so it is within the reach of modulator technology.

Current line-by-line pulse shapers work for input pulse trains with high repetition rates around 10 GHz. Decreasing the repetition rate of the input pulse train requires an increase in the spectral resolution to resolve the individual comb lines. Previous high resolution setups resolved the individual modes from a 3 GHz pulse train [3]. The static line-by-line pulse shaping setup described here resolves the individual modes from an 890 MHz repetition rate mode-locked titanium sapphire laser, modifies them and recombines them into a pulse-shaped output. This line-by-line pulse shaper with 357 MHz resolution [12], corresponding to a resolving power of $\sim 10^6$, periodically maps a static mask pattern onto the optical spectrum. The spectral resolution demonstrated here is, to the best of our knowledge, the highest reported in pulse shaping. This is an important step toward OAWG.

The low repetition rate line-by-line pulse shaping must be combined with high speed modulation to realize OAWG. Several high speed modulation techniques capable of these modulation speeds are explored. Many of the high speed modulation technologies rely on the spatial confinement afforded by single mode (SM) fiber. The design, implementation and analysis of the optical system required to separate adjacent frequency modes into separate SM fibers is presented.

This thesis analyzes the dynamics of the shaped pulses as the update rate approaches the repetition rate of the laser, $f_{rep}$. Results illustrate that there is a fundamental tradeoff between response speed and waveform fidelity when high speed modulators are merged with line-by-line resolution. Central to this fundamental limitation is the spectral recombination of the pulse. For some pulse shaping schemes where few comb lines are modulated at high speeds, a pulse shaper with spectral-independent recombination of the pulse provides a novel approach that circumvents the waveform-fidelity and response-speed limitations enforced by a spectral recombination.

## 1.2 Thesis outline

Chapter 2 covers the fundamentals of pulse shaping. The basics of classic pulse shaping are explained through the development of static pulse shaping theory. As the limits are expanded to include control of a pulse train over the entire period of the pulse train (static OAWG), it becomes clear that the individual frequency modes that make up the pulse train spectrum must be controlled. This requirement leads to a description of frequency combs and specifically the laser source used in this project. Finally, other OAWG designs are presented to show the usefulness of this work and how it fits into the field of dynamic line-by-line pulse shaping.

Chapter 3 develops the dynamic pulse shaping theory and provides understanding of the theory's implications through the use of a dynamic pulse shaping simulation. The time-dependent output of the pulse shaper is modeled for several dynamic masks, showing a tradeoff between response speed and waveform fidelity.

Chapter 4 elaborates the details of a VIPA, the heart of the high spectral resolution pulse shaper. Everything from the optimized design of the VIPA to an analysis of its nonideal behavior is described. Finally, by analyzing the VIPA output, reasonable limitations on the allowed bandwidth of the pulse shaper are calculated.

Chapter 5 presents the VIPA-based pulse shaper with the highest known spectral resolution. The details of the cross-correlation technique used to measure the pulse shaper output are described. To illustrate how dispersion inside the VIPA-only pulse shaper works, a simulation is compared to the bursts of pulses measured from the high resolution VIPA-based pulse shaper.

Chapter 6 provides an overview of several current modulation techniques capable of GHz speeds required to perform OAWG for the pulse shaper described in chapter 5. The experiments and analysis exploring the potential of several of these modulation technologies are presented.

Chapter 7 offers a solution to separate adjacent groups of modes into fiber, a necessary step for several modulation technologies. The design takes advantage of a microlens array to individually image groups of modes into separate fiber channels. The performance of the physical setup is measured and analyzed.

Chapter 8 concludes the thesis with an overall discussion of the work presented and offers suggestions for future work.

# Chapter 2

# Fundamentals of pulse shaping

## 2.1 Classic pulse shaping

Pulse shaping is the art of transforming an input pulse train into a pulse train with controlled shapes. There are several ways to simply shape pulses. For example, when a short pulse passes through a material with normal dispersion, blue light travels slower through the material. This dispersion introduces chirp (low frequency light followed by higher frequency light), that has the effect of broadening the pulse. To compensate for this common phenomenon a prism pair can be used to introduce negative dispersion can be used to augment the shape of a train of pulses. These simple methods for controlling a train of pulses do not allow for much flexibility in creating a totally custom pulse train. This is why this thesis focuses on a more powerful and general method for pulse shaping: spectral masking.

The idea behind spectral masking is that by controlling the frequency composition, or spectrum, of a pulse train, the time domain output can be shaped. A simple diagram of this process is visualized in Figure 2.1.

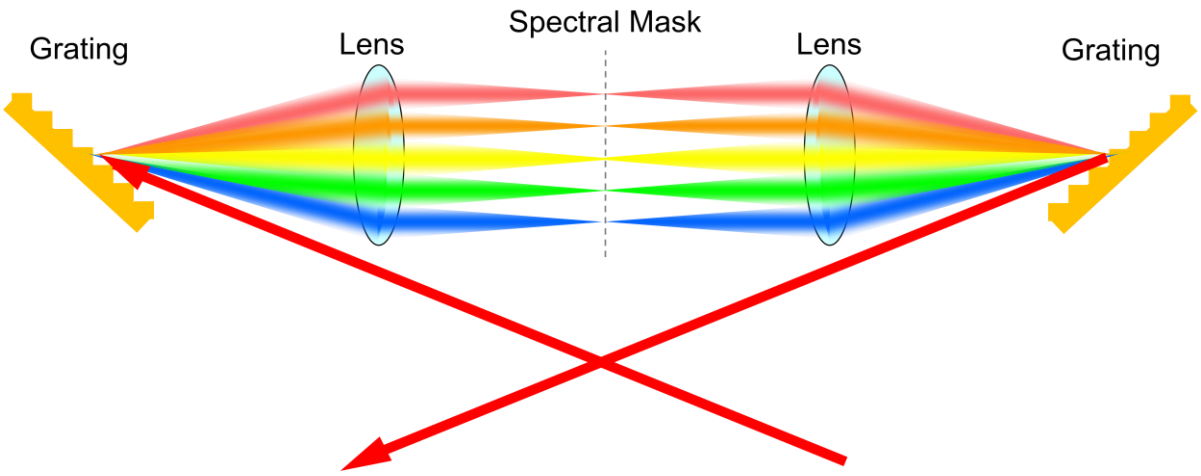


Figure 2.1: Spectral mask pulse shaper diagram.

The input pulse train first hits a spectrally dispersive device such as a grating. Different wavelengths leave the grating at different angles. So by placing a lens a focal length away from the grating, the angular wavelength dependence is converted into spatial dependence. Another way to consider this is that the lens is performing a Fourier transform of the grating output. By placing a lens one focal length away from a source, the Fourier response of that source is created a focal length away from the lens. A mask can be placed in this Fourier plane to selectively pass or block different frequencies or change their phases. Finally, when the pulse is reconstructed using another lens and grating the temporal output pulse train has been modified from the original as a result of the Fourier relationship between frequency and time.

Spectral mask pulse shaping is analogous to linear, time-invariant filtering. By selectively blocking certain frequencies the output can be controlled. Mathematically, spectral mask pulse shaping is described by the convolution of two time dependent signals [1]

$$e_{out}(t) = e_{in}(t) * h(t) = \int e_{in}(t')h(t-t')dt' \qquad (2.1)$$

where $e_{out}(t)$ is the output electrical signal for a given input signal $e_{in}(t)$ and $h(t)$ is a filtering function that acts on the signal. In the case of a spectral mask, it makes more sense to think

about the filtering function as a function of frequency instead of time. Because the physical mask blocks or passes frequencies it is already naturally a function of frequency. So an equivalent way to consider this convolution is multiplication in frequency space given by

$$E_{out}(\omega) = E_{in}(\omega)H(\omega) \tag{2.2}$$

where $E_{in}(\omega)$ is the input signal, $E_{out}(\omega)$ is the output signal and $H(\omega)$ is the filtering function as a function of frequency given by the Fourier transform pairs

$$H(\omega) = \int h(t)e^{-i\omega t}dt \tag{2.3}$$

and

$$h(t) = \frac{1}{2\pi}\int H(\omega)e^{i\omega t}d\omega \tag{2.4}$$

To better understand this convolution process, consider a few simple filters and their effects on an output signal. If the filtering function is simply a delta function in time, the frequency response is one that passes all frequencies. This corresponds to a signal output that is the same as the input, or the case where no filtering is performed. Another interesting case is one where the spectral filter is narrowed to only pass a small band of frequencies. The smaller the band of frequencies, the more blurred the output signal is from the original input in time. In other words, quick changes in the input signal become longer, slower changes in the output signal. The extreme case of this is when all but one frequency is filtered out of the original input signal. The result is an output signal that has a constant value equal only to the amplitude of that frequency in the input.

The spectrum of an input pulse train is a frequency comb as described in section 2.2 . If the resolution of the spectrally dispersive device inside the pulse shaper is lower than the repetition rate of the pulse shaper input, the discrete frequency modes of the comb will be

separately resolved in the mask plane of the pulse shaper. Since a narrow filter in frequency is required to have a long effect in time, as described in the previous paragraph, in order to achieve control over the entire period of an input pulse train, the individual frequency modes of the comb must be controlled. This limit is called line-by-line pulse shaping. Any repeating waveform, within the bandwidth of the input pulse train, can be produced by individually controlling the discrete frequency modes that comprise the pulse train [4].

## 2.2 Femtosecond combs

Spectral decomposition pulse shaping requires that the spectrum of an input pulse train be modified to create the desired output waveform. In order to have full control of a waveform over the entire period of the pulse train, the individual frequency components that make up that frequency spectrum must be controlled. The frequency spectrum of a pulse train of short pulses is often called a frequency comb or a femtosecond comb (when pulses that makeup the pulse train are approximately 5-100 fs in duration). The individual frequency modes that make up that comb are also referred to as comb lines. These terms are used throughout this thesis. The purpose of this section is to explain what a frequency comb is and how it is created for use in this project.

Although short pulse trains can be produced in a variety of ways, the source used in this project is a mode-locked Ti:sapphire (Ti:sapph) laser, as elaborated in section 2.4 Mode-locking a laser establishes a fixed phase relationship between all of the lasing longitudinal modes [9]. In other words, all the allowed frequencies of the laser are locked together with fixed phase resulting in pulsed laser operation. This process can be considered in time as well, where a narrow in time, but broad in frequency, pulse propagates through the laser cavity, resulting in an output of narrow pulses separated by the round trip time of the laser cavity. The repetition rate

of the laser, $f_{rep}$, can then be calculated by inverting this round trip time. Mode-locking a laser requires that loss inside the laser cavity is greater for continuous wave (CW) operation than for pulsed operation. To achieve this difference, typically Ti:sapph lasers rely on the nonlinear index of refraction of the Ti:sapph crystal: the Kerr-lens effect. Basically, the higher the intensity of light, the larger the index of refraction is inside the Ti:sapph crystal. This effect results in intense light of a pulse being self focused by the crystal, while less intense CW light is not focused. By misaligning the Ti:sapph cavity slightly so that light that is self focused by the crystal due to this effect has less loss than light that passes straight through, higher net gain for pulsed operation is achieved.

The spectrum of the ultra-short pulse train is the frequency comb. To understand how it is created, first consider a single pulse of light where the spectral width is inversely proportional to width of the temporal envelope, $\tau$, of that pulse. This means that short pulses in time have a broad spectral response. Consider the spectrum of a series of pulses all equally spaced by the pulse train period, $T$, pictured in Figure 2.2.

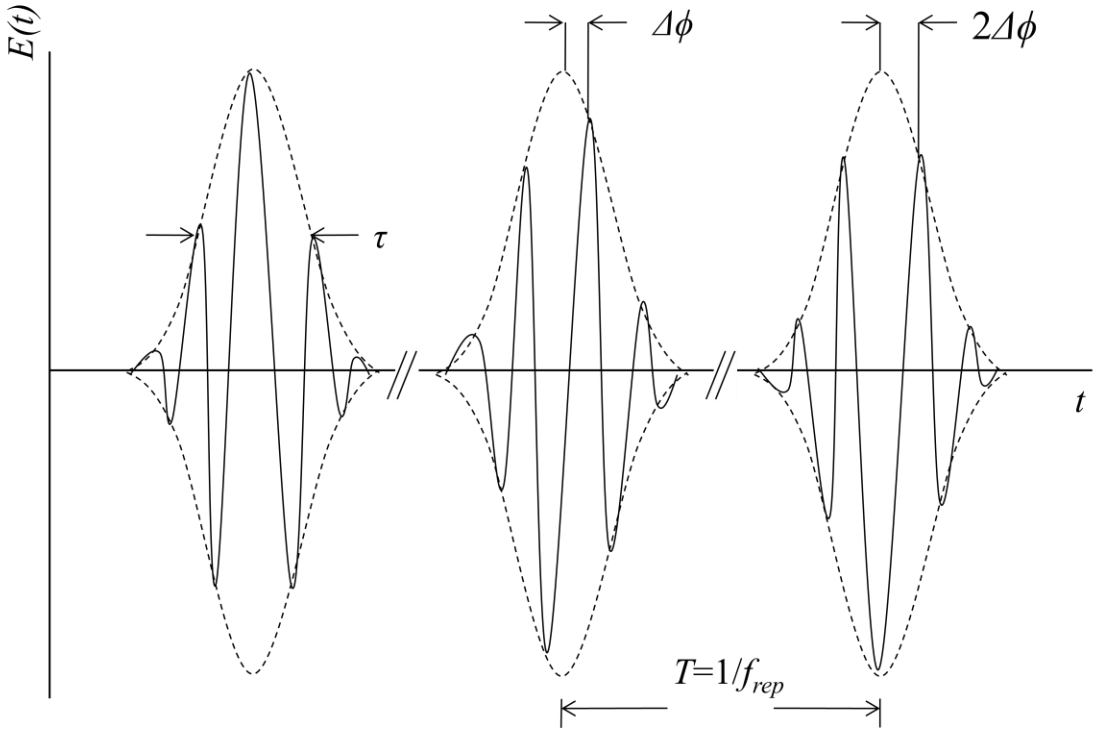


Figure 2.2: Time domain portrait of a pulse train, showing phase evolution of the electric field inside the Gaussian envelope of the narrow pulse train. Adapted from [9]

The carrier-envelope phase, $\varphi$, is the phase shift between the peak of the pulse envelope and the closest peak inside the carrier wave. If the pulse propagates through any dispersive material, the difference between phase and group velocities results in $\varphi$ evolving as the pulse propagates. The change in $\varphi$ from pulse to pulse is given by $\Delta\varphi$. The Fourier transform of the comb of pulses in time separated by the period $1/f_{rep}$, is a comb in frequency separated by $f_{rep}$. This comb is pictured in Figure 2.3. The evolution of the carrier envelope phase has the effect of shifting this comb in frequency. This offset frequency, $f_0$, can be calculated from the phase evolution of the pulse described in Figure 2.2 by

$$f_0 = \frac{1}{2\pi} f_{rep}\Delta\phi \tag{2.5}$$

The source of this offset frequency is the difference between group and phase velocities of the pulse, a result of the pulse propagating through any dispersive media. The frequency of a given mode is

$$\nu_n = nf_{rep} + f_0 \tag{2.6}$$

where $n$ is an integer that indexes the frequency of the $n^{th}$ mode. Note that optical frequencies are on the order of 370 THz (at $\lambda$ = 810 nm) and $f_{rep}$ is approximately 1 GHz. This means $n$ is approximately 370,000 for the mode in the center of the spectrum. Also, observe that the width of the Gaussian that encompasses the individual spectral modes is $1/\tau$, so the shorter the pulses are in time, the broader the spectrum.

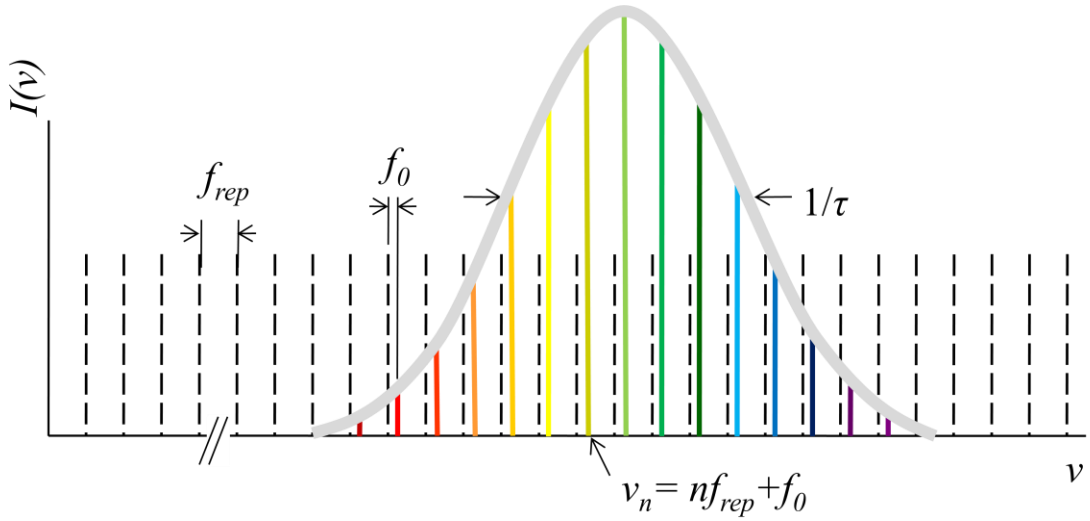


Figure 2.3: Frequency comb showing the spectral response of a pulse train. Adapted from [9]

The discrete frequencies that make up ultra-short pulse trains make them excellent sources for pulse shaping. The shorter the pulses of the input pulse train the finer the temporal control over the pulse shaper output becomes. This means that the ability of pulse shapers to create arbitrary waveforms is limited by the bandwidth of the input. The more broadband a pulse train

source, the more general waveforms that can be produced using a pulse shaper. In order to create an output with a fast response (short in time), large optical bandwidth is required.

## 2.3 Grating resolution

A key component to any spectral masking pulse shaper is the use of a spectrally dispersive element. A standard grating can be used for this purpose in classic pulse shapers where line-by-line pulse shaping is not necessary. In this section, the resolving power of a grating is explored and through calculations the necessity of another spectrally dispersive device is made apparent.

The resolution, $\Delta\lambda$, of a simple grating can be calculated by

$$\Delta\lambda = \frac{\lambda}{m\Lambda l} \tag{2.7}$$

where $\lambda$ is the center wavelength, $m$ is the grating order, $\Lambda$ is the spatial frequency of the grating, and $l$ is the width of the spot on the grating. This equation shows that the resolution of the grating can be improved by illuminating more lines on a grating ($\Lambda l$). A grating with $\Lambda$ = 1200 l/mm can achieve a resolution of $\Delta\lambda$ = 0.05 nm at $\lambda$ = 810 nm in the first grating order by illuminating a 12 mm spot on the grating. However, even this resolution is not nearly enough to resolve the individual frequency modes that make up the frequency comb for a laser running at 1 GHz. A quick calculation using $c = \lambda v$ shows that a change of 1 GHz for 810 nm light corresponds to a change of only .0021 nm. To illustrate why a grating is not used in the high resolution pulse shaper, consider how large a grating would have to be to achieve the necessary resolution. In order to achieve the high resolution necessary for line-by-line pulse shaping at 1 GHz using only a grating imaged in its first order with $\Lambda$ = 1200 l/mm at $\lambda$ = 810 nm, the size of

the imaged spot on the grating would need to be 32.1 cm. While it is not impossible to create such a grating, it would be very expensive and difficult to work with such large scale optics to acquire the necessary resolution. This grating size can be reduced by increasing the number of lines by increasing $\Lambda$ of the grating or by using a higher diffraction order of the grating. However both of these parameters increase the angle of diffraction from the grating given by

$$\theta_{out} = \arcsin\left[m\lambda\Lambda - \sin(\theta_{in})\right] \tag{2.8}$$

The maximum angle possible from the grating is 90° (input angle to the grating would is 90° and the output order would be 90° from that). At this limit the maximum grating frequency is $\Lambda$ = 2469 l/mm for first order diffraction. This means the illuminated spot size on the grating would still need to be 15.62 cm. Alternatively if the second order diffraction is used the maximum grating frequency $\Lambda$ = 1234 l/mm with input and output angles set to 90°. Meaning that to achieve enough resolution to resolve 1 GHz frequency modes from one another, still an illuminated spot size of 15.62 cm is required. The invariance of the necessary spot size to the diffraction order can be seen by plugging equation (2.8) into equation (2.7). Note that in addition to the large grating, a very large lens would also be required to image the grating to an output which would individually resolve the 20,000 individual modes that comprise the laser spectrum in a straight line. This is why a virtually imaged phased array is used to achieve the high spectral resolution required to achieve line-by-line pulse shaping at 1 GHz. See chapter 4 for more details on the VIPA.

## 2.4 Frequency comb source

The frequency comb source used for this project is a mode-locked titanium-sapphire (Ti:sapph) ring laser [13]. Before jumping into the specifics of this laser, consider typical

Ti:sapph lasers. The size of the laser cavity determines the amount of time it takes for a pulse to propagate through the cavity which in turn sets the repetition rate. So the repetition rate of the laser can be calculated by the inverse of the round trip time inside the laser cavity. Commonly Ti:sapph lasers are built to operate around 70-90 MHz. This typical repetition rate is the result of the laser cavity size built to accommodate a prism pair. This is so the normal dispersion from the Ti:sapph crystal can be mitigated through the use of a prism pair inside the laser cavity to introduce anomalous dispersion. By adjusting the spacing between the prism pair the dispersion inside the laser cavity can be carefully controlled. Additionally, the prism pair spatially separates the spectrum of the laser onto the back mirror allowing for control of $f_0$ by tilt of this back mirror, $f_{rep}$ by the length of the cavity, and through the use of a slit, the spectrum and bandwidth of the laser can be tuned. However, the small repetition rate of these lasers will make the individual comb lines close together in frequency (separated only by 70 MHz or so) which makes it difficult to achieve line-by-line pulse shaping where these individual modes must be separated from one another.

To make it easier to separate adjacent frequency modes from one another, a higher repetition rate laser is desired. The laser is designed to have with a repetition rate of 890.4 MHz by reducing the cavity length to about 33.7 cm. One convenient solution to creating a small laser cavity is to build it with ring geometry. In ring geometry the pulse inside the laser cavity can be made to bounce off of several mirrors in a small amount of space. Several negatively chirped mirrors are necessary to control the dispersion inside the laser cavity as described later. Also, unlike many other laser geometries where light is double passed through space (cavity length is two times the physical length), in ring geometry there is no retro-reflecting mirror. Light circulates through the cavity, meaning the length of one circulation is the cavity length (thereby

assisting in the goal of a shorter cavity). The ring configuration illustrated in Figure 2.4 shows how a pulse circulates when mode locked. Note, in the ring laser configuration, mode-locking behavior can occur for both clock wise (CW) and counter-clock wise (CCW) propagating pulse. There is a 50% chance that the laser will mode-lock CCW (desired output direction). In the event that the laser mode-locks CW, mode-lock can be broken by interrupting the beam and reacquired by perturbing the laser mirror again. Eventually, the laser will randomly mode-lock in the desired direction. Once the laser is mode-locked in one direction the laser is stable and the pulse train continues to propagate in that direction.

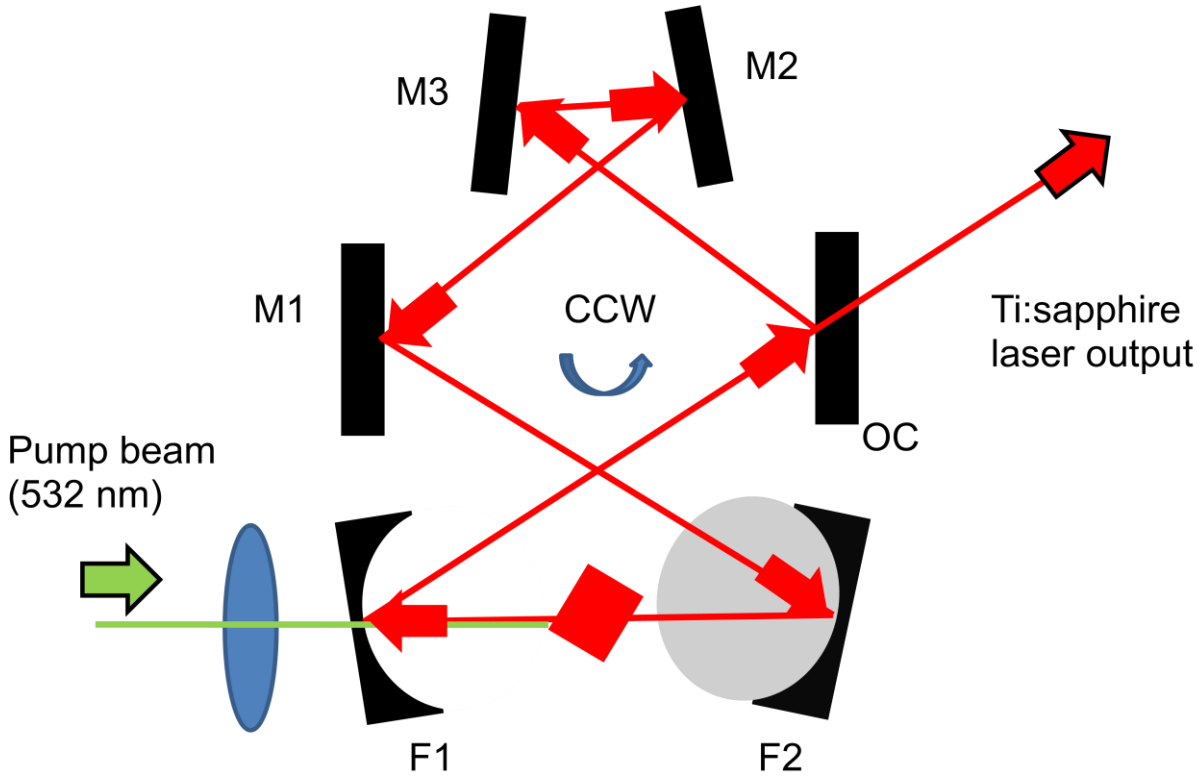


Figure 2.4: Ring laser diagram, showing how the direction of the Ti:saph output depends on the propagation direction of the pulse inside the laser cavity.

The limited amount of space in the laser cavity means there is no room for a prism pair to introduce the negative dispersion necessary to cancel out the dispersion from the Ti:sapph

crystal. This is why 5 negatively chirped dielectric mirrors are used instead to control the dispersion inside the laser cavity. The 2.2 mm Ti:sapph crystal induces approximately 148 $fs^2$ group delay dispersion (GDD) onto the pulse [13]. Each negatively chirped mirror provides -45 $fs^2$ GDD per reflection, corresponding to -225 GDD from the mirrors which means the total GDD for a round trip inside the ring cavity is -77 GDD. This means the ring laser is operating in the anomalous dispersion regime, a common and stable regime for mode-locked Ti:sapph lasers [9].

The bandwidth of the laser output can be used to estimate the width of pulses in time as shown in Figure 2.5. The center of the laser output spectrum is 815 nm with a FWHM of 40 nm corresponding to a pulse duration of approximately 54 fs. As explained in section 4.7 this is more bandwidth than can be used in the high resolution pulse shaper.

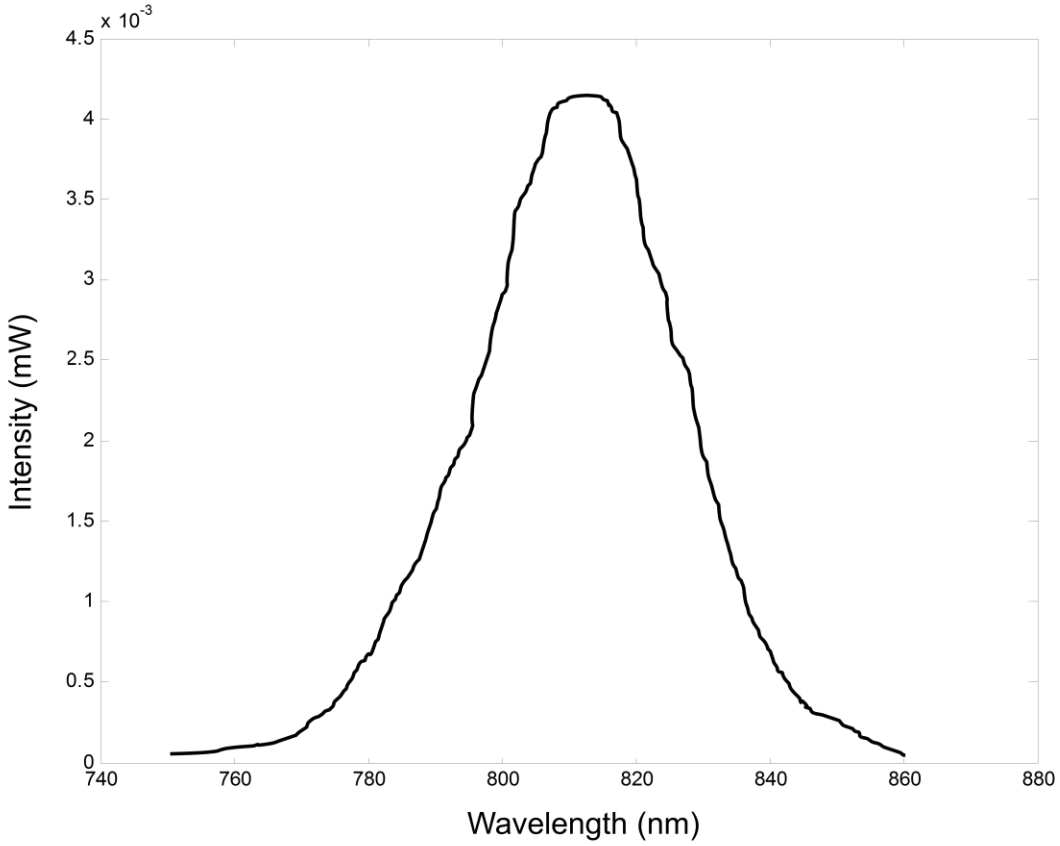


Figure 2.5: Pulse train source, 890.4 MHz Titanium sapphire laser, spectrum. The 40 nm FWHM corresponds to a pulse width of approximately 54 fs in time.

## 2.5 State of the art of pulse shaping

Many labs worldwide explore and advance the capability of pulse shaping. A common problem with telecommunication is the broadening of short pulses as they propagate through fiber due to dispersion. Since arbitrary dispersion can be applied to a pulse train using spectral mask pulse shaper, the dispersion of the fiber can be canceled by negative dispersion from the pulse shaper [14]. Using a pulse shaper to perform this pulse compression is superior to the use of a simple prism pair to introduce anomalous dispersion since a pulse shaper can program custom dispersion that better compensate for the fiber [15,16].

Line-by-line pulse shaping becomes possible when the individual frequency modes that comprise an input pulse train can be independently controlled. This limit enables the full time record, *T*, of the pulse train to be controlled. Creating static OAWG, a waveform that is as arbitrary as one can create only repeating every period. Repeating customized pulse trains have uses in ultrafast spectroscopy, nonlinear fiber optics and high field physics [17].

The current challenge in this field is to completely control the spectrum and have control over the spectrum at the repetition rate of the laser or OAWG. Several labs are currently working on dynamic pulse shaping systems. M. Akbult at University of Central Florida has done dynamic pulse shaping work using injection locked vertical cavity surface emitting laser (VCSEL) diodes as modulators [10]. Akbult's setup begins with a 12.5 GHz source and using a virtually imaged phased array (VIPA), the individual frequency modes of the source are separated from one another. Then each mode is reflected off different VCSELs in the array and by controlling the voltage of the VCSEL near threshold, the phase of the individual modes can be controlled between $-\pi/2$ to $\pi/2$. The fast response of the VCSEL array has been able to achieve update rates of up to 1 GHz. This rapid update rate is enough to perform OAWG in our setup since we have the high spectral resolution capable of resolving adjacent modes of a 1 GHz pulse train. Akbult's setup uses a fiber pigtailed VIPA with 100 GHz FSR. This only allows for 6.25 GHz channel separation between adjacent modes. In other words, his setup does not have the spectral resolution necessary to resolve adjacent modes from a 1 GHz source.

Another limitation of Akbult's setup is the use of the injection locked VCSEL diode array as the modulator. When a VCSEL is used as a modulator [18], the injection current is modulated very quickly which in turn modulates the phase and amplitude of the seed light that is incident to the VCSEL. The primary effect is phase modulation and this modulation is limited by only

being able to swing from $-\pi/2$ to $\pi/2$. This limits the full arbitrary nature of the waveforms that can be produced. To be fully arbitrary, one must be able to control the phase of each mode from $-\pi$ to $\pi$.

A completely different approach to achieving OAWG spectrally shapes alternating pulses independently from one another and then fuses the combined output to create a 5 ns window of arbitrary waveform output. This creative approach is the work of R. Scott at the University of California Davis [11]. First, three individual pulses of a 10 GHz pulse train are temporally separated from one another and sent down different fiber optic lines. Then, an electronic arrayed waveguide grating (eAWG) is used in each path to shape the spectrum of each pulse independently. The three pulses are brought into sync with one another by adding 10 ns of delay to the first pulse and 5 ns of delay to the second pulse. Finally, an output is created by combining the three pulses using an arrayed waveguide grating (AWG). By temporally separating out the pulses prior to modulating the spectrum of each one and using variable delays in each path to recombine the pulses temporally, Scott is able to make use of the additional information to create a more arbitrary optical waveform (33ps features) than would be possible at 10 GHz (100 ps features). This clever approach circumvents the limitations derived in chapter 3 since there is never any modulation at or faster than the spectral capacity of the input. In other words, by combining the spectra of three pulses, at 10 GHz, one is able to achieve the speed of a 30 GHz pulse train (30 GHz of optical bandwidth), but limited to a period of 5 ns.

The major limitation to this technique is that it is not continuous, the arbitrary nature of the output is limited to 5 ns every 15 ns. This is because it takes 3 pulses worth of information to produce only one period of output.

# Chapter 3

# Dynamic line-by-line pulse shaping

## 3.1 Dynamic line-by-line pulse shaping theory

The naïve expectation of pulse shaping is that the instantaneous optical pulse will correspond to the instantaneous spectral mask; however this is not the case. Fast modulation creates sidebands that should interfere with adjacent comb lines to create an instantaneous response. Line-by-line spectral mask pulse shaping relies on a high spectral resolution dispersive device to resolve the individual frequency modes of the input pulse train. When this high spectral resolution device is used to recombine the pulse, these sidebands are filtered out resulting in an output with a slow response. The Fourier time-frequency limit constrains how quickly the waveform can change given high spectral resolution.

In this section, a theoretical expression for Fourier transform pulse shaping with a time-varying mask is derived. This derivation begins by reviewing the theory for the familiar case of a time-independent mask, then showing how to extend the theory to include time variation. This treatment draws on previous publications analyzing grating pair compressors [19] as well as pulse shapers with static masks [20,21].

First, assuming the input field can be separated in space and time, the input field immediately before the first diffraction grating can be expressed as

$$e_{in}(x,t) = Re\left\{\hat{e}_{in}(x,t)e^{j\omega_o t}\right\} = Re\left\{a_{in}(t)s(x)e^{j\omega_o t}\right\} \tag{3.1}$$

where $x$ is spatial position in one dimension, $t$ is time, $a_{in}$ is the input pulse train, and $\omega_0$ is the angular frequency of the input carrier. For simplicity, the notation

$$F(x,t) = Re\left\{\hat{F}(x,t)e^{j\omega_o t}\right\} \tag{3.2}$$

is used. The spatial profile of the input can be approximated as Gaussian, a reasonable approximation for a typical laser source operating in (transverse electromagnetic) $TEM_{00}$ mode (lowest order or fundamental transverse mode). Then

$$s(x) = e^{-x^2/w_{in}^2} \tag{3.3}$$

where $w_{in}$ is the input spot radius. Consider the standard pulse shaping configuration, in which the grating and the pulse shaping mask are placed at the front and back focal planes of the lens, respectively. The field at the Fourier plane is

$$\hat{e}_1(x,t) = \int \frac{d\tilde{\omega}}{2\pi} A_{in}(\tilde{\omega}) e^{-\frac{(x-\alpha\tilde{\omega})^2}{w_0^2}} e^{j\tilde{\omega}t} \tag{3.4}$$

where $A_{in}(\tilde{\omega})$ is the Fourier transform of $a_{in}(t)$, $\tilde{\omega}$ is the optical frequency, and

$$w_0 = \left(\frac{f\lambda}{\pi w_{in}}\right)\left(\frac{\cos\theta_i}{\cos\theta_D}\right) \tag{3.5}$$

is the radius of the focused beam at the Fourier plane (for any single frequency component), and

$$\alpha = \frac{\lambda^2 f}{2\pi c d \cos\theta_D} \tag{3.6}$$

is the spatial dispersion parameter which describes the proportionality between spatial displacement and optical frequency. The grating input and output (diffraction) angles are $\theta_i$ and $\theta_D$ respectively for a reference ray at frequency $\omega_0$ traveling along the optical axis, $d$ is the grating periodicity, and $f$ is the focal length [1]. This analysis ignores chromatic aberrations by assuming the same focal length and spot size for all frequency modes imaged by the pulse shaper. This assumption is reasonable since experimentally only 10 nm FWHM of optical bandwidth are imaged and over such narrow optical bandwidth the effects of varying focal length

and spot size are negligible. The spatial mask, with a complex transmission, $M(x)$, is key to the pulse shaping action. The field directly after the mask is simply

$$\hat{e}_2(x,t) = M(x)\hat{e}_1(x,t) . \tag{3.7}$$

The spot size is always finite at the masking plane for any specific frequency. In general, the electric field subsequent to the spatial mask is a nonseparable function of space and frequency. This nonseparability occurs because the spatial profiles of the focused spectral components may be altered by the mask - i.e., some spectral components may experience spatially varying amplitude or phase, while others may not. This variation leads to different diffraction effects for different spectral components and results in an output field which couples space and time beyond the simple and reversible effects of spectral dispersion [21,22].

From an applications perspective, one is usually interested in generating a spatially uniform output beam with a single prescribed temporal profile. In order to obtain an output field that is a function of frequency (or time) only, one must perform an appropriate spatial filtering operation. In the following, consider the case where such spatial filtering is implemented by focusing into a single-mode optical fiber placed in a Fourier plane of the second diffraction grating [1,20] which is the pulse shaper output shown in Figure 2.1. This situation is of practical interest for applications related to optical communications. In a fiber-pigtailed reflection geometry pulse shaper, for example, the input beam is collimated from and the output beam is coupled back into the same physical fiber [23,24]. A similar mode selection operation could also be performed by coupling into a regenerative amplifier for high-power applications. Approximately, such spatial filtering can be performed simply by placing an iris after the pulse shaping setup.

In this analysis the masked field is propagated back to a second grating placed at the back focal plane of a second lens. Then the electric field is focused through a Fourier transforming lens into a single mode fiber. A Fourier transforming lens is a lens placed one focal length away from a source which creates the Fourier response of that source a focal length away from the lens. The portion of the field that corresponds to the single guided spatial mode of the fiber is transmitted; any remaining portion of the field is not guided and is therefore eliminated. Denoting the spatial mode of the fiber as $u_F$ and the field at the fiber plane as $\hat{e}_3$, the coupled field is

$$\hat{e}_{out}(x,t) = \frac{\int dx\, \hat{e}_3(x,t) u_F^*(x)}{\int dx\, u_F(x) u_F^*(x)}\, u_F(x) \tag{3.8}$$

Here the first factor gives the complex amplitude of the coupled field, and the second is the spatial mode. The most interesting case is when the input field as transformed by the pulse shaper and the subsequent lens is mode-matched to the fiber. In this case the output complex spectral amplitude function becomes

$$A_{out}(\tilde{\omega}) = \left\{ \sqrt{\frac{2}{\pi w_o^2}} \int dx\, M(x) \left[ \exp\left( \frac{-(x-\alpha\tilde{\omega})^2}{w_o^2} \right) \right] \right\}^2 A_{in}(\tilde{\omega}) \tag{3.9}$$

.

Note that in the absence of masking, the entire input field is successfully coupled into the fiber without loss. The effective filter in the frequency domain is the square of the convolution of the mask function $M(x)$ and the spatial field profile of the beam at the masking plane. The spatial field profile enters once through the spectral dispersion of the first grating and lens and a second time (together with an integral over *x*) through the mode matching with an assumed Gaussian fiber mode. Any physical features on the mask smaller than $w_0$ are smeared out by the convolution. This smearing limits what features can be transferred onto the spectrum. Only

features that are larger than $w_0$ can be transferred onto the spectrum. Wavelength components impinging on mask features that vary too fast for the available spectral resolution are diffracted out of the main beam and eliminated by the spatial filter. This process can lead to phase-to-amplitude conversion in the pulse shaping process [19,23]. Conversely, in the limit $w_0 \rightarrow 0$, the apparatus provides perfect spectral resolution, and the effective filter is just a scaled version of the mask.

The theory may now be extended to include a time-varying mask, $M(x,t)$, with Fourier transform

$$\tilde{M}(x,\omega) = \int dt\, M(x,t) e^{-j\omega t} \quad . \tag{3.10}$$

The complex spectral amplitude of the field immediately after the masking operation may be written as

$$A_2(x,\tilde{\omega}) = \int \frac{d\tilde{\omega}'}{2\pi} A_{in}(\tilde{\omega}-\tilde{\omega}') M(x,\tilde{\omega}') e^{-\frac{\left(x-\alpha(\tilde{\omega}-\tilde{\omega}')\right)^2}{w_o^2}} \quad . \tag{3.11}$$

Assuming an input field prior to the grating as given by equation (3.1), the field immediately after the grating may be written as [19]

$$e'_{in}(x,t) = \sqrt{\beta_a}\, Re\left\{ \int \frac{d\tilde{\omega}}{2\pi} A(\tilde{\omega}) s(\beta_a x) e^{-j\gamma\tilde{\omega}x} e^{j(\omega_o+\tilde{\omega})t} \right\} \tag{3.12}$$

$$\text{where} \qquad \beta_a = \frac{\cos\theta_i^{(o)}}{\cos\theta_D^{(o)}} \qquad \text{and} \qquad \gamma = \frac{2\pi}{\omega_o d \cos\theta_D^{(o)}} \tag{3.13}$$

Here $\theta_i^{(0)}$ and $\theta_D^{(0)}$ are the input and output (diffraction) angles for a reference ray at frequency $\omega_o$ traveling along the optical axis, and $d$ is the grating periodicity. The $e^{-j\gamma\tilde{\omega}x}$ factor imparts the variation in diffraction angle with frequency; and the beam size is scaled by the inverse of an astigmatism factor $\beta_a$, which results from the difference in input and output angles.

Propagation from the grating at the front focal plane of the lens to the masking plane at the back focal plane may be analyzed using the Fourier transform property of a lens [25,26]. This analysis is formalized for a one dimensional field in the direction the frequency modes are spread out by the spectrally dispersive device, in the *x* direction. In the *y* direction, the field is a Gaussian profile with no spectral dependence as it is orthogonal to the spectrally dispersive device. Specifically, for a scalar, monochromatic, one-dimensional field $s_{in}(x)$ at a plane a distance *f* in front of a thin lens with focal length *f*, the resulting field at an output plane a distance $f$ behind the lens is given by

$$s_{out}(x) = \sqrt{\frac{j}{\lambda f}} \int dx' \, s_{in}(x') e^{jkxx'/f} = S_{in}(\frac{kx}{f}) \tag{3.14}$$

Where $k = \omega / c = 2\pi / \lambda$, and $S_{in}(k_x)$ refers to the spatial Fourier transform of the input spatial profile $s_{in}(x)$, and the Fourier transforms are defined by

$$S(k) = \int dx \, s(x) e^{jkx} \qquad \text{and} \qquad s(x) = \frac{1}{2\pi} \int dk \, S(k) e^{-jkx} \tag{3.15}$$

.

Using this Fourier transform property in conjunction with equation (3.1) for the field just after the grating, the field at the masking plane of the pulse shaper, equation (3.4), is obtained.

The time-varying mask modifies the frequency content at the various spatial locations. Mode matching at the output of the pulse shaper is taken into account as earlier, giving

$$A_{out}(\tilde{\omega}) = \iint \frac{d\tilde{\omega}'}{2\pi} dx \, A_{in}(\tilde{\omega} - \tilde{\omega}') M(x, \tilde{\omega}') e^{-\frac{\left(x - \alpha(\tilde{\omega} - \tilde{\omega}')\right)^2}{w_o^2}} e^{-\frac{(x - \alpha\tilde{\omega})^2}{w_o^2}} \tag{3.16}$$

The interpretation is that for large frequency shifts, the new frequencies induced through the time variation of the mask will be focused at a position transversely shifted with respect to the fiber mode. This is a direct result of how the pulse is reconstructed. Since a spectrally dispersive device is used to combine the spectrum, a change in the frequency (from the modulation) results

in a shift in the location where the pulse is reconstructed. Since the output of the pulse shaper is restricted to be a Gaussian profile, higher modulation frequencies of the time-varying mask are partially suppressed.

To better understand how these high modulation frequencies are suppressed, consider the simple situation of a CW source being modulated in time. One observes sidebands in the frequency spectrum of this modulated light separated from the central frequency, $f_{cent}$, by the modulated frequency, $f_{mod}$, as pictured in Figure 3.1. Note that these sidebands carry essential information about the modulated beam. In other words if these sidebands are eliminated, the CW source would no longer be modulated in time. If this modulated CW signal is passed through a sufficiently narrow spectral filter, such as an interference filter, the sidebands will be suppressed.

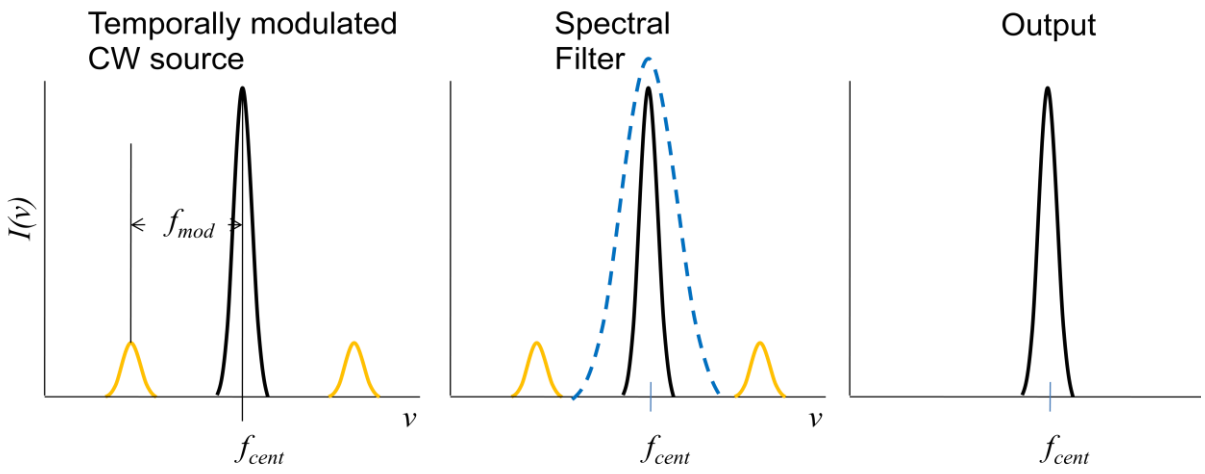


Figure 3.1: Temporally modulated CW light, solid black curve, carries modulation information in the side bands in frequency, solid orange curves, separated from the central frequency by the modulation frequency. The spectral filter, dashed blue curve, shows that a sufficiently narrow filter will filter out the sidebands and thereby eliminate the temporal modulation of the signal.

The faster the modulation, the farther these sidebands are from the central frequency and the more suppressed the sidebands are for a given spectral filter. This simplified situation is no

different from what happens inside a dynamic pulse shaper. The individual frequency modes that make up the laser are phase locked CW sources separated by $f_{rep}$. Modulations in the dynamic mask create sidebands on each of these CW sources. Since these sources are recombined using a spectrally dispersive device (i.e. VIPA), only frequencies close to the center frequency are imaged to the correct location in the VIPA output. By restricting the spatial output of the pulse shaper (such as into fiber, or using a spatial mode filter), incorrectly located outputs are eliminated. This has the effect of applying a spectral filter to each frequency mode with a width corresponding to the resolution of the spectrally dispersive device. The higher the modulation frequency, the less of an effect it has on the output.

A very simple case is when the mask is time-varying but uniform in space; the time-varying mask is simply a modulator placed into a pulse shaper. Replacing $M(x,\tilde{\omega})$ in equation (3.11) with $M(\tilde{\omega})$ yields

$$A_{out}(\tilde{\omega}) = \int \frac{d\tilde{\omega}'}{2\pi}\left(M(\tilde{\omega}')e^{-\alpha^2(\tilde{\omega}')^2/2w_o^2}\right)A_{in}(\tilde{\omega}-\tilde{\omega}') \qquad (3.17)$$

Here the modulation spectrum is multiplied by a low-pass filter function. As the radius of the spot size at the masking plane gets smaller, the low pass filter cuts off at lower frequencies (in the Fourier plane of the pulse shaper frequency is dispersed into space).

This analysis reveals a fundamental trade-off in pulse shaping: very high spectral resolution implies a limit to the rate at which the pulse shaping function may be modified. In line-by-line shaping, the implication is that one may not fully update pulse shapes at speeds corresponding to the laser repetition rate while simultaneously fully resolving individual comb lines.

## 3.2 Dynamic line-by-line simulation setup

The dynamic effects of a pulse shaper can be illuminated by numerical simulation. The simulation numerically calculates the double integral in equation (3.16). The input and output spectra are represented by arrays that contain the input and output frequency comb of the pulse train, while the spectral mask is a matrix that fully describes the mask in space and time. In the integral, the mask is represented as a space and $\omega'$ dependent matrix, which is equivalent to taking the one-dimensional Fourier transform of the temporal response of the mask at each spatial point. An array size of 256 pixels was chosen to balance resolution and computation time. The details of this simulation can be seen in appendix A. The input spectrum is an array of 0's with a spike of 1 every 8 pixels enveloped in a Gaussian. By taking the Fourier Transform of this array we can construct the input train of pulses as a function of time as shown in Figure 3.2.

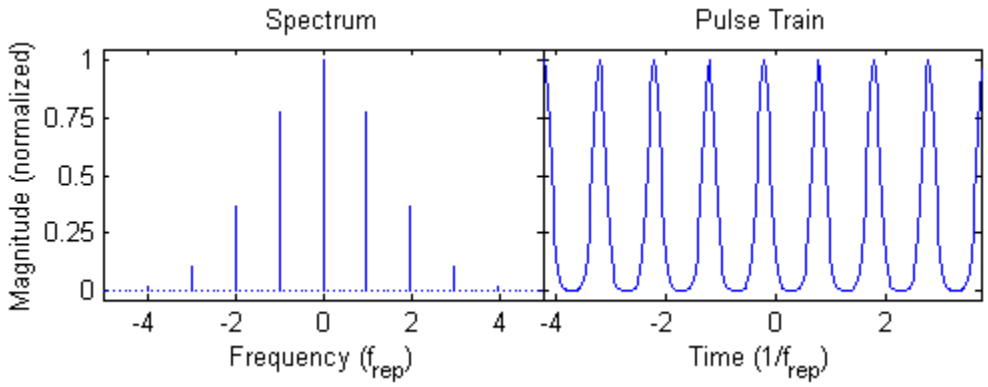


Figure 3.2: Input spectrum and pulse train.

The relationship between α and $w_0$ sets the width of the Gaussian "smearing" functions in equation (3.16) that determine the response of the pulse shaper. The narrower the Gaussians, the slower the response to changes in the mask. Conversely, the broader the Gaussians are, the more blurred or poorly resolved the spectral response of the mask. Poor resolution results in low

waveform fidelity and excessive resolution results in slow response speeds. The result is a fundamental trade-off between spectral resolution and response time.

To investigate the effects of the smearing functions on pulse shaping, $w_0$ is varied, which changes the width of the smearing functions. Both α and $w_0$ are set by the specific design of a given pulse shaper with a dependence on parameters like wavelength and focal length of the lens used in the pulse shaper as described by equations (3.5) and (3.6). Since we are looking at a narrow band of frequencies, the effect of wavelength on this ratio is not important to the illustrated fundamental trade-off. The variation of $w_0$ is can be realized by setting the spacing between the comb lines on a spectral mask then adjust the focus of the comb lines to change their size. For generality $w_0$ is expressed as a fraction of

$$w_{rep} = 2\pi\alpha f_{rep} \tag{3.18}$$

For example, for a 1 GHz laser with the individual comb lines by dispersed by 20 μm, $w_{rep}$ = 20 μm, and so, if $w_0$ is set to be 1/2 the distance between comb lines or 10 μm, the spatial dispersion parameter α can be calculated to be 10/π μm / GHz from the expression $w_0 = ½\ w_{rep} = \pi f_{rep}\alpha$.

## 3.3 Dynamic line-by-line simulation results

In a first set of test cases, dynamic effects are seen in the response of the pulse train to a step. A sample of pulses is analyzed by abruptly changing the spectral mask at time 0. Before time 0, the spectral mask allows the full spectrum to pass, and after time 0, it blocks every other comb line as shown in Figure 3.3.

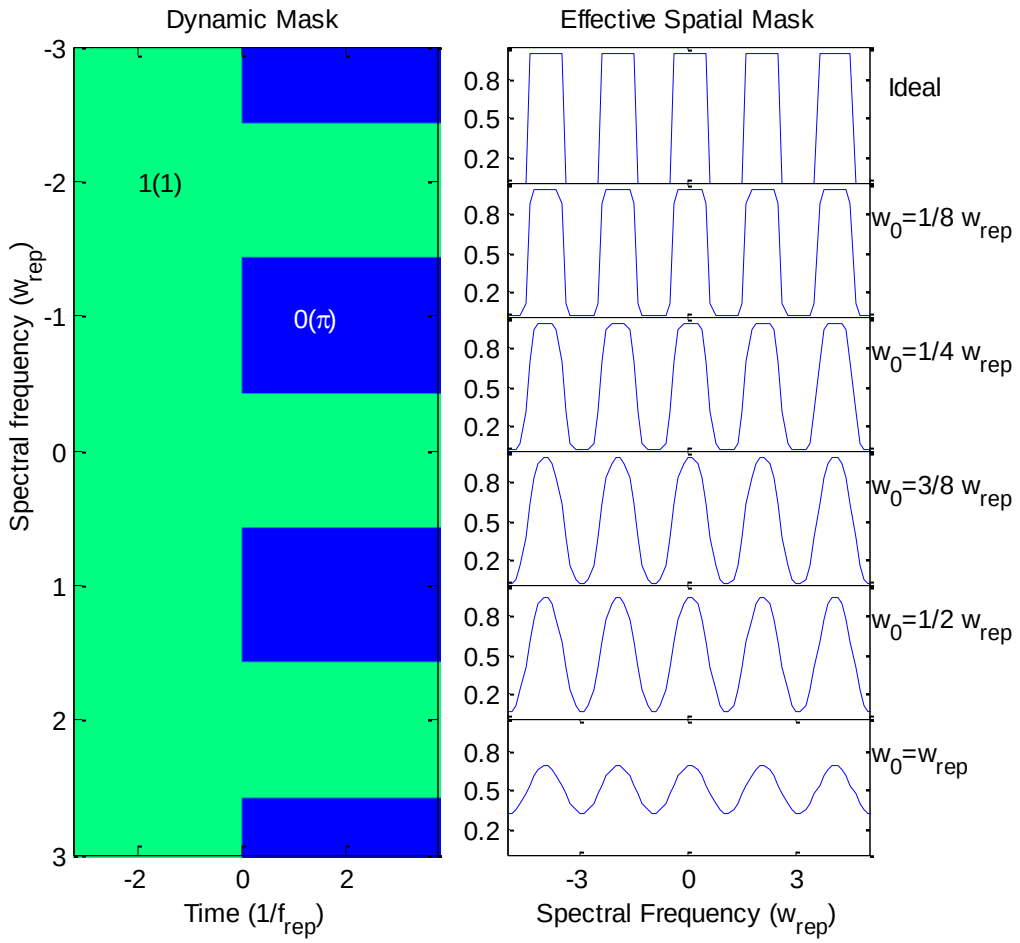


Figure 3.3: Dynamic mask and effective spectral filter functions. Left: the dynamic mask illustrates the abrupt change in the mask at time 0. Two cases are considered. For spectral amplitude masking, the mask is set to block every other comb line for $t > 0$; the blue regions in the figure correspond to a mask value of 0. For spectral phase masking, the mask is set to impart a phase shift of $\pi$ to every second comb line as illustrated by the blue regions in the figure. Right: the static filter functions corresponding to times $t > 0$ illustrate the blurring of the effective mask for larger spot sizes. The effective spatial masks are calculated by convolving the smearing function in equation (3.16) with the spatial mask.

The mask pattern for $t > 0$ doubles the separation between comb lines in frequency space, which makes the time between pulses half as long, or in effect doubles $f_{rep}$. This is referred to as double pulsing. Figure 3.4 shows the switching behavior of the pulse train at various smearing function widths or spot sizes, $w_0$. Due to the periodic nature of the Fast Fourier Transform algorithm, transient effects were observed at both edges of time aperture used in the simulation. These

expected edge effects are cropped out of the final pulse trains in order to simplify the appearance of Figure 3.4. This simplification was done by doubling the sample size of the input and then cropping the final output by deleting the first and last quarter leaving the same number of pulses. For large spot sizes such as $w_0 = w_{rep}$, the spectral blurring due to a broad smearing function is quite evident. In the spectral domain, this effect is seen in Figure 3.3, which plots the effective static filter functions corresponding to the mask at time $t > 0$. The edges of the filter function become increasingly rounded for increasing $w_0$ due to the convolution of the mask with the smearing function. In the time domain, as the spot size increases and the smearing function becomes broader, the ability of the shaper to produce clear double pulses is diminished. In Figure 3.4, observe the red dotted line for the larger spot sizes and how it peaks at two different heights; this poor waveform is due to the overlapping of the power associated with different comb lines at the same position on the mask. At smaller spot sizes the spectral resolution is improved, with the result that the pulses in the doubled repetition rate region ($t > 0$) have equal intensities. However, the dynamic response suffers. The $w_0 = 1/8\ w_{rep}$ case shows how slowly the pulse train responds to change when the smearing function is narrow; the system takes about 4 repetition periods to shift to double pulsing while at $w_0 = w_{rep}$ it shifts almost instantly. The key point is that response to an abrupt change in the mask occurs over a time duration that scales inversely with the spectral resolution. Qualititatively speaking, the optimum spot size for the system described above that balances speed and spectral resolution (waveform fidelity) is approximately $w_0 = 1/3\ w_{rep.}$ This qualitative observation agrees well with numerical optimizations for $w_0$ performed in section 3.4 This means that the spot size of the comb lines on the spectral mask should be approximately 1/3 the distance between comb lines, although the exact choice will depend on the specific merit function of interest.

It is worth mentioning that this analysis assumes infinitely fast modulation. Even with ideal instantaneous modulation, the response is far from instantaneous. This means that with a spot size of $w_0 = 1/3\ w_{rep}$ the modulator speed need only a rise time of 1/4 the period ($1/f_{rep}$). A faster modulator will not improve the temporal response of the pulse shaper output.

We note that the pulse train output appears to be affected prior to the step in the mask at time 0. However, due to the large delay in propagating through the pulse shaper (not portrayed in the figures), there is no violation of causality. Apparent changes in the output waveform prior to $t = 0$ simply correspond to the components of light being deflected or diffracted to shorter paths through the shaper. Consistent with this interpretation, the analysis in [21] for a static pulse shaper shows a direct linkage between delay time in the shaped output waveform and spatial offset in the output beam (here without spatial filtering). Angular dispersion from a grating or other spectral disperser is linked fundamentally to delay gradients across the beam [27]. Waveform changes in response to a step in the mask occur within a time region approximately equal to the inverse of the spectral resolution, which is consequently within the total time variation across the beam just after the spectral disperser.

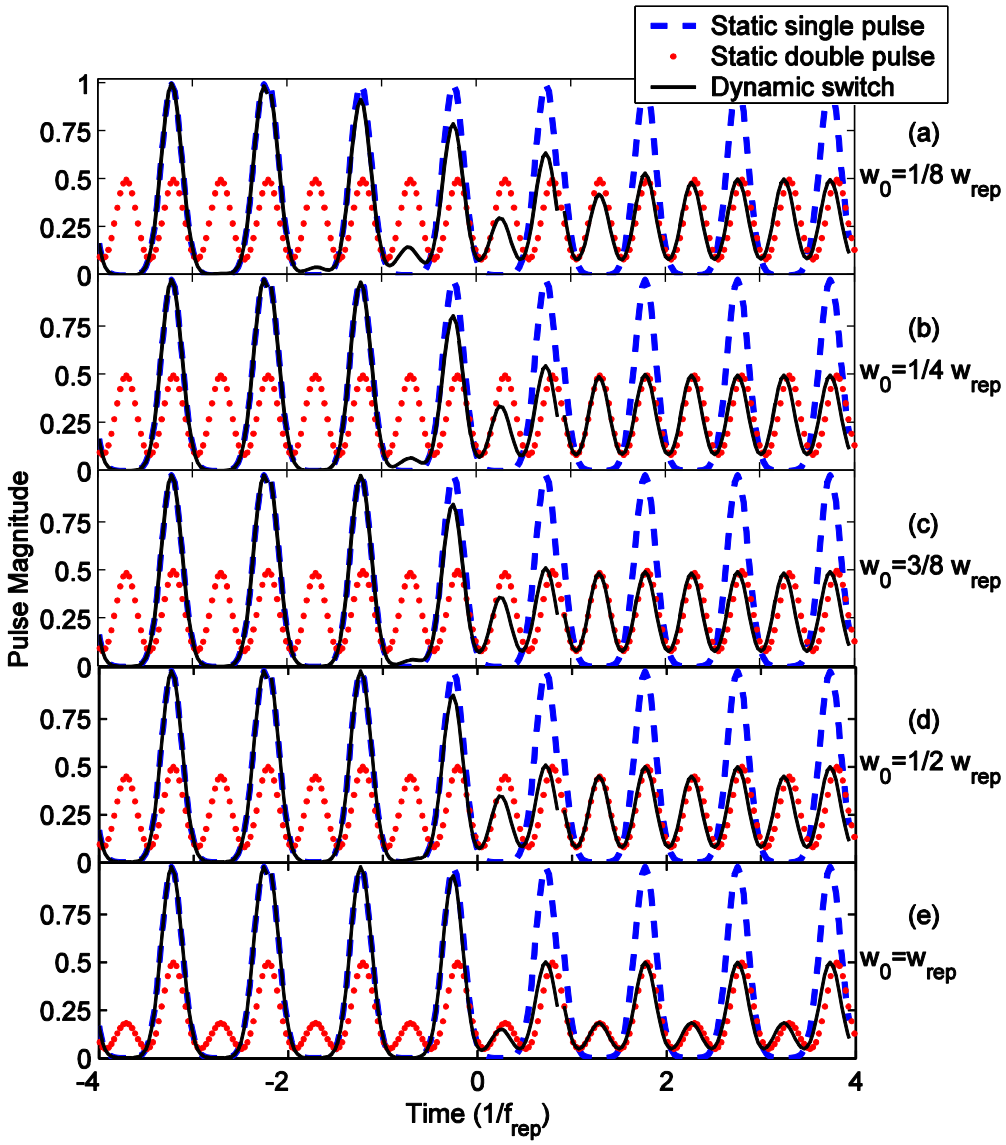


Figure 3.4: Response of the pulse train to an alternating amplitude mask, turned on abruptly at $t = 0$, at various spot sizes, $w_0$. The dashed blue line shows the static pulse train where the full spectrum is allowed to pass which yields the expected single pulsing behavior. The dotted red line shows the static pulse train when every other comb line in the spectrum is masked out. This results in double pulsing behavior, with waveform fidelity that depends on $w_0$. The solid black line shows the dynamic response of a pulse train to the mask that abruptly switches at $t = 0$.

In a second example, we consider a stepped phase mask. A phase shift of $\pi$ between alternating comb lines is turned on abruptly at $t = 0$. Both the physical phase mask and the static spectral filter function (corresponding to $t > 0$) are also shown in Figure 3.3. The filter function is

the same as for the amplitude mask case, but only with a slight change to the vertical axis: instead of alternating between 0 and 1, the phase of the mask alternates between 0 and $\pi$ (complex transmission alternates between (1,0) and (-1,0)). The output pulse train can be seen in Figure 3.5. For high resolution static pulse shaping, the mask is expected simply to shift the output in time by half the period of the pulse train. Similar to what was seen in the amplitude case, we have fast response for large $w_0$ but with waveform fidelity compromised (this is evident in this case as a reduction in intensity). Conversely, for small $w_0$ there is high spectral resolution and good waveform fidelity (negligible loss of intensity), but a slow response. Again the optimum spot size appears to be approximately 1/3 the distance between comb lines verified in section 3.4

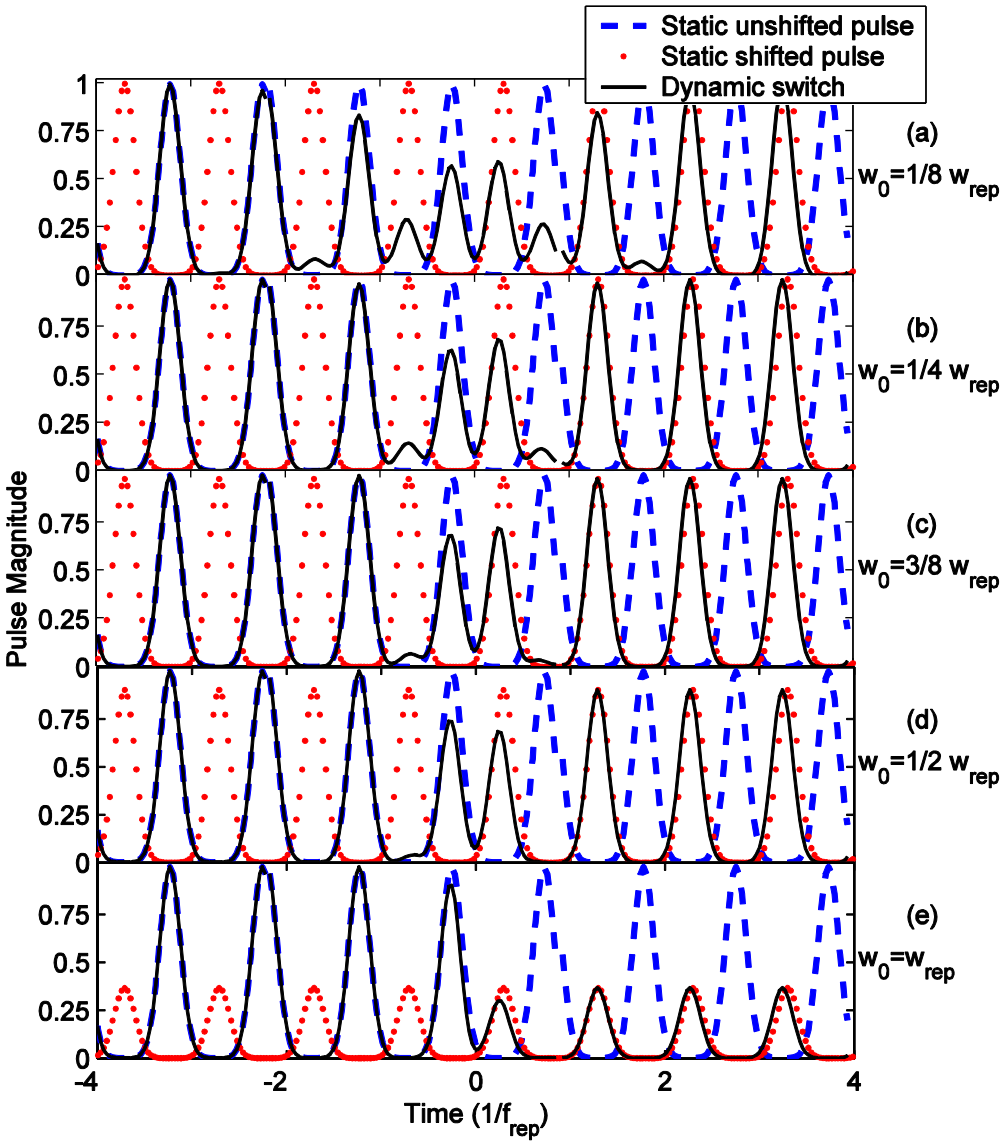


Figure 3.5: Response of the pulse train to an alternating phase mask, turned on abruptly at $t$ = 0, at various spot sizes, $w_0$. The dashed blue line shows the static pulse train where the full spectrum is allowed to pass with no phase shift. The dotted red line shows the static pulse train when every other comb line in the spectrum is phase shifted by π; this yields the expected shift of half the period in the output pulse train. The solid black line shows the dynamic response of a pulse train to a mask that abruptly switches between the two at $t$ = 0.

Another test case that illustrates the dynamic behavior of the pulse shaper is its response to a sweeping bandpass spectral filter. Here the mask blocks the full spectrum except for a square window. This pass window is then shifted spatially as a function of time allowing different

portions of the spectrum to pass at different times. The window scans through the center of the spectrum at a rate of 2/9 $w_{\text{rep}}f_{rep}$. For this case, a larger α was used to give greater separation of the comb lines. Thus, instead of having a comb line every 8 pixels, there is a comb line every 24 pixels. For this calculation, all the input comb lines were set to unity amplitude, so the spectral envelope is flat rather than Gaussian. The width of the window was set to 24 pixels corresponding to $w_{rep}$ in space or $f_{rep}$ in frequency, such that ideally, one comb line is allowed through the mask at a time. The response of the pulse train to this sweeping filter can be seen in Figure 3.6. At the top of this figure is the ideal case, a pseudo-spectrogram that shows how one might naïvely expect the system to respond to the moving filter, allowing one comb line through at a time. This pseudo-spectrogram is created simply by multiplying the input spectrum by a scaled version of the time-dependent mask (no smearing taken into account), and then the comb line is broadened appropriately by the inverse time window chosen to construct the figure.

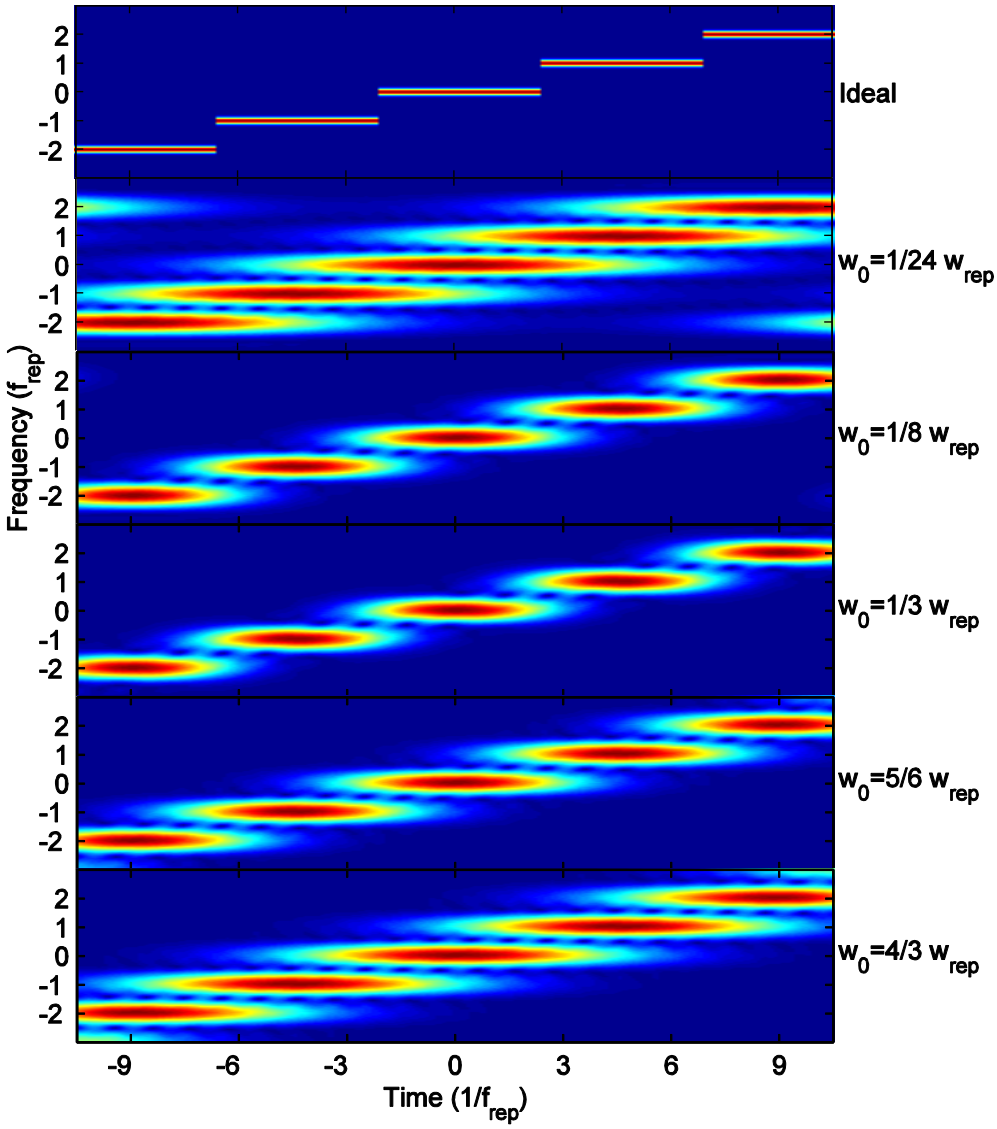


Figure 3.6: Spectrogram response of a pulse train with equal size comb lines to a sliding spectral window of size $f_{rep}$ for various spot sizes, $w_0$. The ideal case is a pseudo-spectrogram of what one would naively expect from a moving spectral filter.

The spectrograms for the actual simulated output signals at various spot sizes were created using a gate function set equal to the Hanning window [28] with a size of 32 pixels; this means that the spectrogram at each point in time is the result of the frequency response of the sample inside this window 16 pixels before and 16 pixels after the point in time being calculated. The behavior of these spectrograms may be explained in terms of the smearing function, as

previously discussed. When the spot size is small, the static filtering function that would be obtained for a stationary bandpass mask is sharp, as seen in Figure 3.7. On the other hand, the narrow smearing function slows the response of the pulse train to changes in the mask. This slowing of the response is evident in the $w_0$=1/24 $w_{rep}$ spectrogram where the traces are elongated along the time axis. As $w_0$ increases, the spectrograms initially shrink along the time axis, attaining a minimum extent around $w_0$=1/3 $w_{rep,}$ but then elongate once again. This minimum in duration is explained on the basis of the blurring of the equivalent static filtering functions depicted in Figure 3.7. For large $w_0$ the equivalent static filters are unable to resolve individual lines, and the filter must be tuned over a larger frequency range (which requires more time) before a given comb line is cut off. Thus, the seemingly slow response at $w_0$ = 4/3 $w_{rep}$ arises due to the rounded edges of the effective mask. Since the system is responding to a moving filter, the spectral blurring affects how the system appears to respond in time.

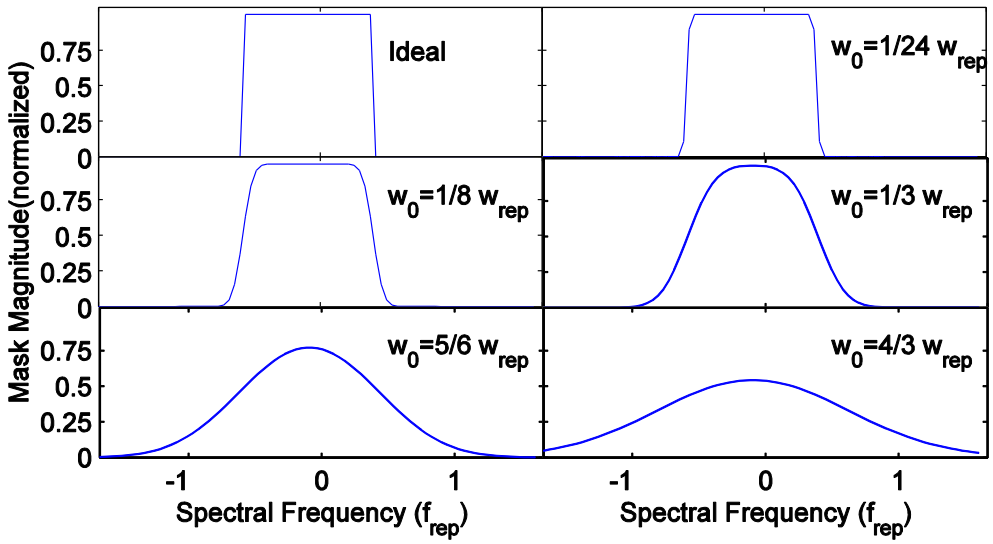


Figure 3.7: Sliding filter effective masks at various $w_0$ as the window crosses the center of the spectrum.

The magnitude of the output waveform is shown in Figure 3.8 for three spot sizes. The ideal case where only a single frequency is selected at a time would result in a constant, time-independent field amplitude. Again, this behavior is most closely approximated by the $w_0$=1/3 $w_{rep}$ test case. However, in all cases where multiple frequencies are present there is modulation in the time domain field magnitude. This effect is minimized for intermediate values of spot size such as $w_0$=1/3 $w_{rep}$. When the spot size is either substantially decreased or increased, more frequencies are simultaneously present. More structure is then observed in the time domain waveforms.

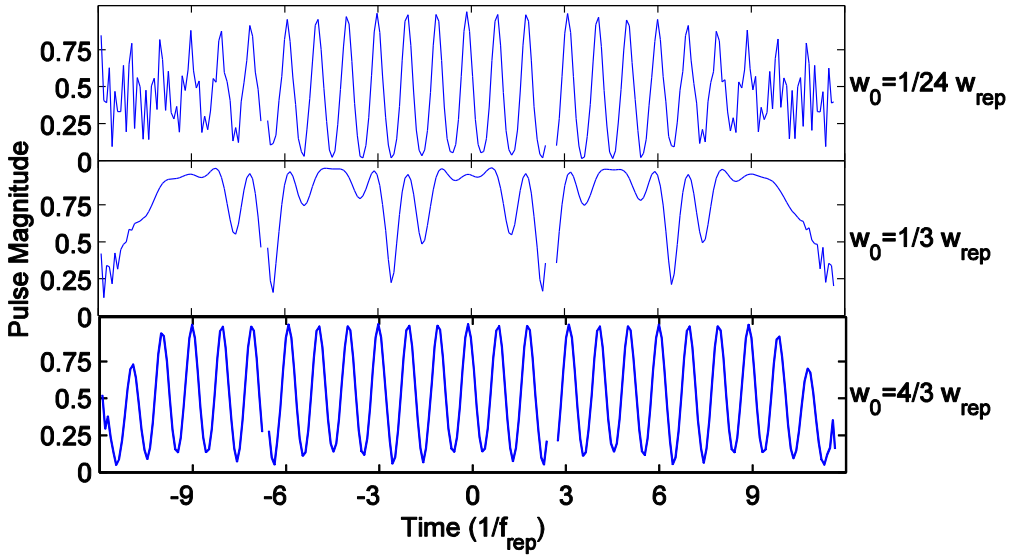


Figure 3.8: Electric field magnitude of a pulse shaper output with a sliding spectral window of size $f_{rep}$ for various spot sizes, $w_0$. Since the tunable filter ideally allows only one comb through at a time, the ideal pulse train would be converted to a constant magnitude, with no oscillation. $w_0$=1/3 $w_{rep}$ is the closest to this ideal response with minimal oscillations in the region where the tunable filter shifts between comb lines.

The dynamic effects of fast pulse shaping have been analyzed and explored in three representative cases. In all these test cases, the spot size of the comb lines on the spectral mask is varied to adjust the width of the smearing function and thereby observe the effects on the output pulse train. The first case is a step in amplitude of alternating comb lines. By removing

every other comb line, the shaper produces a double pulsing output. The pulse train responds quickly with poor spectral resolution when the smearing function is broad. The second case also illustrates this effect by an abrupt phase shift in alternating comb lines by $\pi$, which shifts the output pulse train by half the period. Again, we see similar dynamic effects. The final case describes the response of the pulse train to a sliding spectral filter. Interestingly, we see similar effects for broad and narrow smearing functions; this is explained through the dynamic spatial nature of the mask. All these test cases demonstrate that there is an optimum spot size or width of the smearing function that balances speed and spectral resolution. This optimum is achieved when the radius of the spot size of the comb lines on the spectral mask is approximately one third the distance between comb lines.

It is worth emphasizing that our analysis applies specifically to the case where the output Gaussian mode filter is precisely matched to the field that propagates through the pulse shaper in the absence of masking. Usually this will be the most interesting case, as it minimizes loss. However, new effects may be possible for other choices of the output mode filter. For example, if the mode filter is spatially offset from the optimum position, it will lead to bandpass rather than low-pass filtering action of a rapidly varying pulse shaping mask. In this case, a simple time-varying amplitude or phase mask could be used, for example, to impose single-sideband modulation in parallel onto an entire set of optical comb lines.

## 3.4 Solving for the optimum spot size

The optimum spot size, $w_0$, chosen for a pulse shaper depends on the demands of the pulse shaper output. Maximum response speed is achieved with spot sizes greater than $w_{rep}$, however crosstalk between adjacent mode adversely affects the ability of the pulse shaper to perform line-by-line pulse shaping. Maximum waveform fidelity is achieved with very narrow

spots sizes with $w_0$ smaller than 1/24th $w_{rep}$. A reasonable ideal waveform to strive towards is an idealized output that instantly changes from one mask to another with perfect waveform fidelity pictured in Figure 3.9 and Figure 3.10.

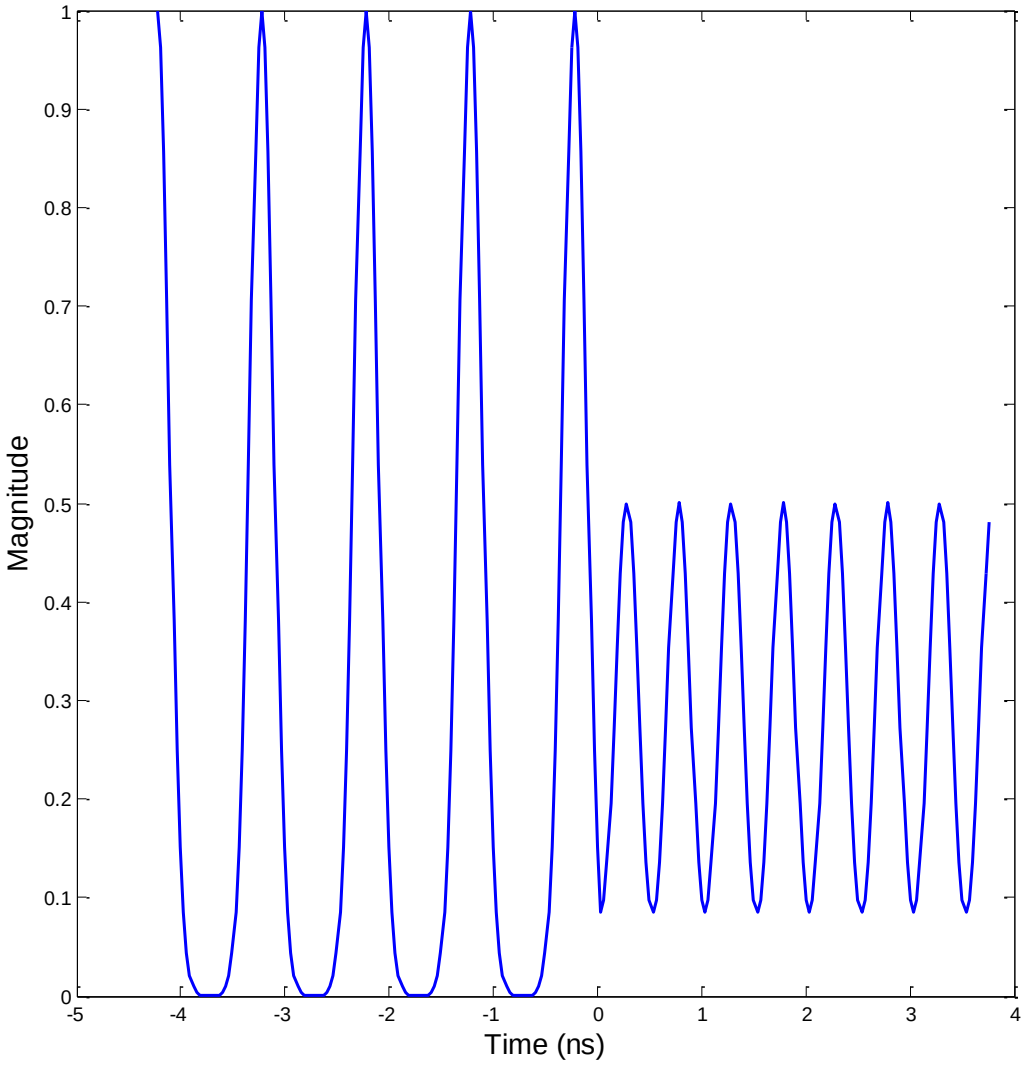


Figure 3.9: Artificial idealized magnitude output of a pulse shaper that instantly switches, at time 0, from single pulsing to double pulsing output with perfect waveform fidelity.

While this ideal waveform cannot be produced as described by the smearing function in section 3.2 , the difference between the idealized output and a realistic output can be minimized. Poor

response speed or poor waveform fidelity will increase the difference between realistic and idealized waveforms. Since $w_0$ affects both of these parameters the optimum spot size that balances these competing effects can be solved.

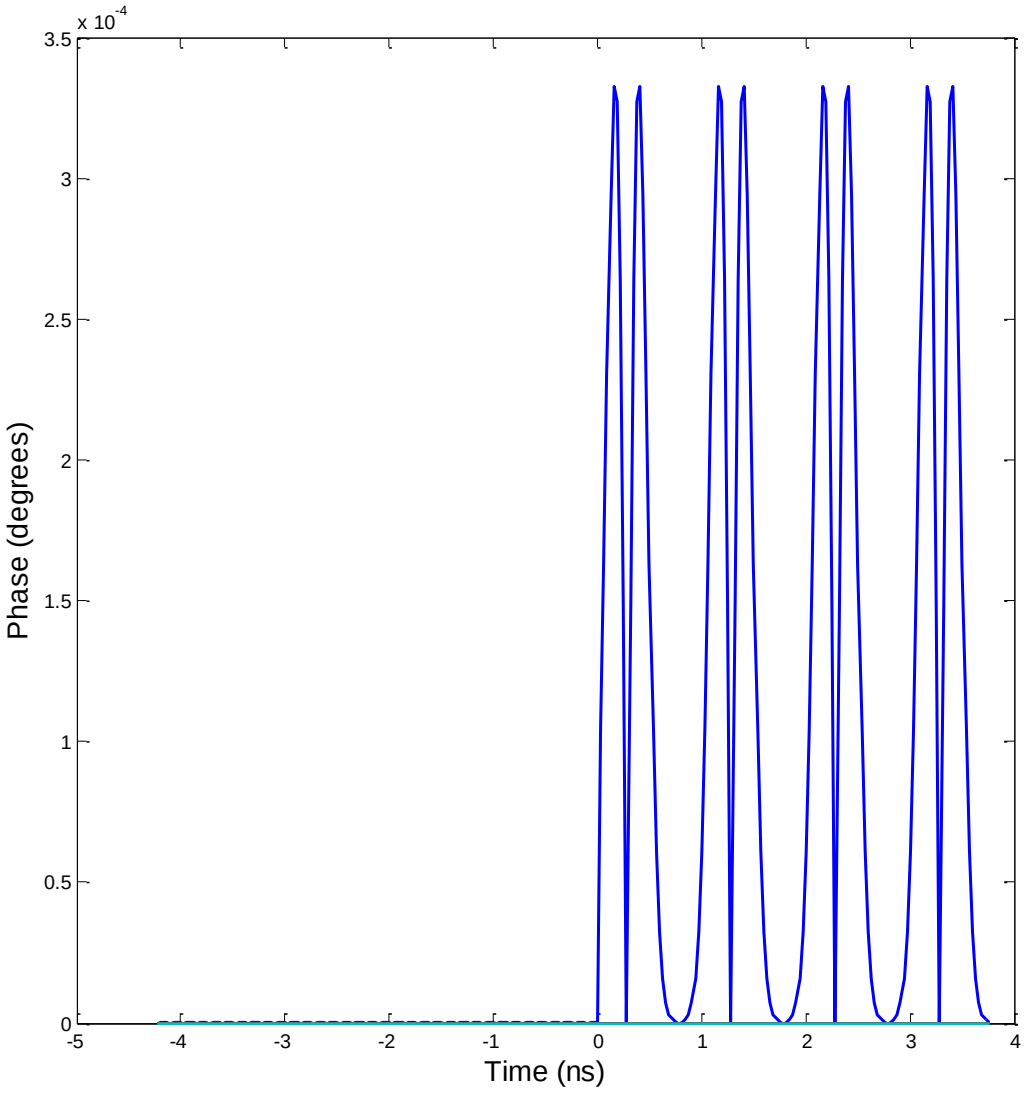


Figure 3.10: Artificial idealized phase output of a pulse shaper that instantly switches, at time 0, from single pulsing to double pulsing output with perfect waveform fidelity.

A minimization routine is run on the pulse shaper simulation described in section 3.2 . While keeping all values set except for the free parameter, $w_{0,}$ the optimum spot size is found

when a minimum is found for a given merit function. Four normalized merit functions are explored: difference in complex spectra (CS), difference in complex electric field (CE), difference in magnitude of the spectra (MS), and difference in the magnitude in the electric field (ME). CS and MS compare the output spectra in frequency while CE and ME compare the output in the time domain. Depending on the application, optimizing for either the spectral or temporal response may be of more importance. This analysis explores both. The optimum spot size for CS is $w_0 = 0.4575\ w_{rep}$ and for MS is $w_0 = 0.4659\ w_{rep}$. As expected, both of the spectral difference merit functions return similar optimum values for $w_0$. The optimum spot size for CE is $w_0 = 0.2503\ w_{rep}$ and for ME is $w_0 = 0.2498\ w_{rep}$. Again the temporal difference merit functions return similar values for the optimum spot size. The temporal response of the optimized spot size to $w_0 = 0.25\ w_{rep}$ is illustrated in Figure 3.11. This optimized spot size allows for rapid response and high waveform fidelity. All four merit functions are important when evaluating the overall response of the pulse shaper. The average of the four merit functions explored is $w_0 = 0.3558\ w_{rep}$ which is close to the ideal spot size of $w_0 = 1/3\ w_{rep}$ estimated from observations of the many simulations in section 3.3 .

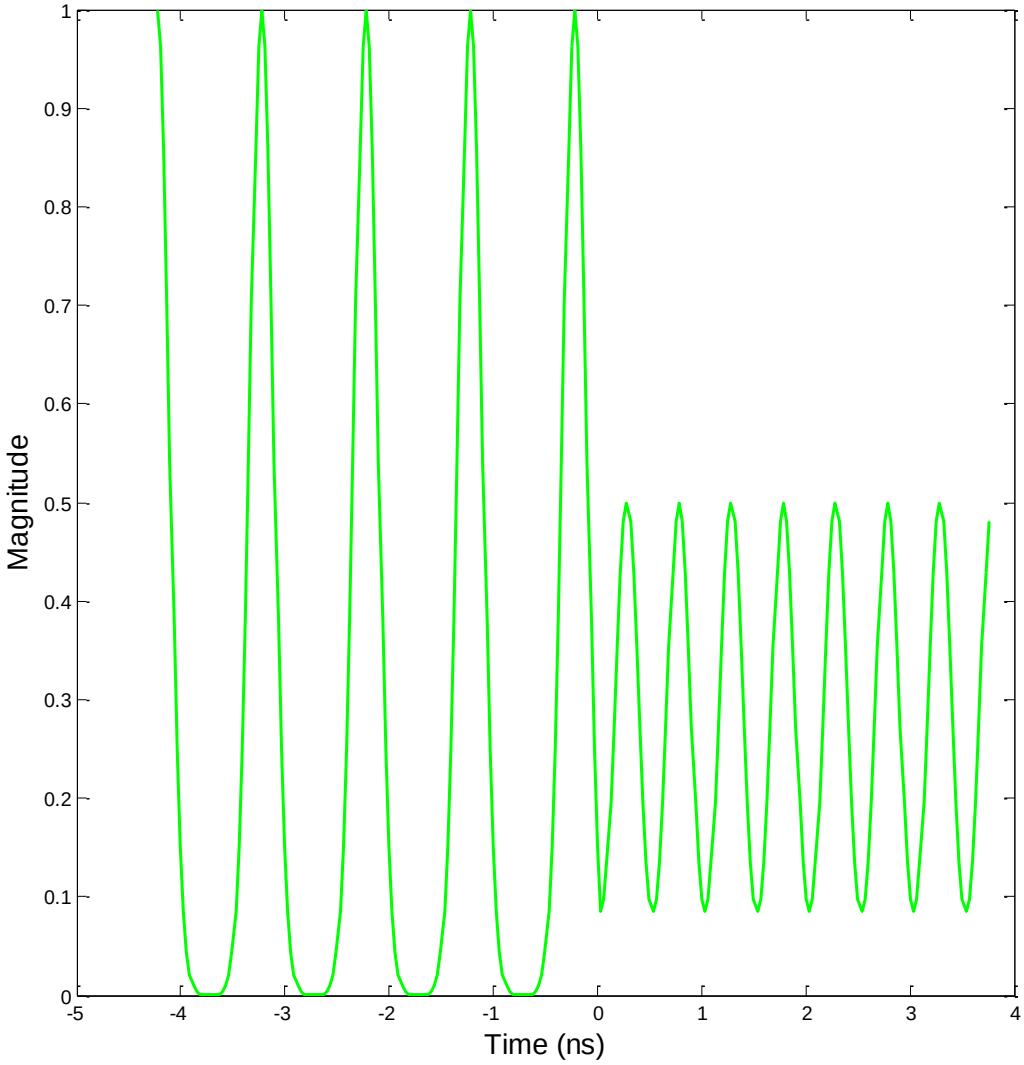


Figure 3.11: Temporal response for optimized spot size, $w_0 = .25\ w_{rep}$

# Chapter 4

# Virtually imaged phased arrays

## 4.1 Virtually imaged phased array theory

In order to achieve the high spectral resolution necessary for line-by-line pulse shaping [1], a virtually imaged phased array (VIPA) is used [29]. Although it is possible to get high spectral resolution from other spectrally dispersive devices, see section 2.3 , a VIPA provides large angular dispersion with high resolution in a practically sized device. The excellent spectral resolution comes at the cost of efficiency. Typical insertion loss of a VIPA is 6 db and when used in a pulse shaper with reflective geometry, this loss is doubled.

A VIPA can be thought of as a tilted Fabry-Perot etalon [30] with a window. By imaging a focus over and over inside the etalon, an array of virtual images is produced. These images then constructively and destructively interfere with one another resulting in an output with angular dependence on wavelength see Figure 4.1.

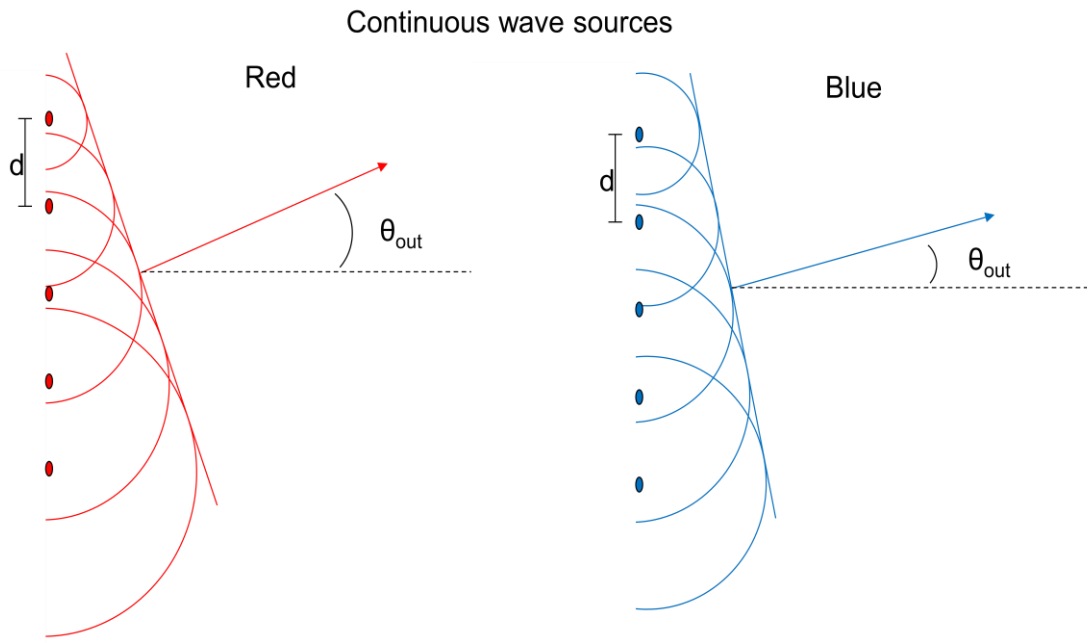


Figure 4.1: Phased array of sources, showing constructive interference at a particular angle, $\theta_{out}$, that depends on wavelength. For a given array of sources with a set distance between each source, *d* and a set delay between each source, φ, observe how the shorter wavelength of blue CW light results in constructive interference of the blue sources at a smaller output angle than that of the red CW light. Phase fronts for a given wavelength add up at a particular angle allowing for high resolution spectral dispersion.

This technique is analogous to what is done with phased radio antenna arrays [31], where by controlling the delay of a given radio signal between each antenna the direction of the radio beam can be controlled. Instead of having real sources (antennae), a VIPA has virtual sources (images) and with a broadband input signal the result is an output direction that depends on wavelength. The output direction, $\theta_{out}$, of a phased antenna array

$$\theta_{out} = \arcsin\left(\frac{\phi\lambda}{2\pi d}\right) \tag{4.1}$$

depends upon the wavelength, $\lambda$, of the signal, the spacing between antennae, *d*, and the delay or phase shift of the signal between each antennae, $\varphi$. Since the wavelength of the radio signal and physical spacing of the array are set, it is the phase delay of the signal between each antenna in

the array that is used to control the direction. In many situations it is useful to use a single antenna array to broadcast multiple frequencies, but emit them in the same direction (i.e. sending radio / TV signals to a city). In this case, it is essential that the delay of each signal be set independently from one another so that all signals are emitted in the same direction. However, if the delay is set to be the same for multiple frequencies (as is the case for the VIPA), then the antenna array would operate much like a VIPA where different frequencies are emitted at different angles.

The delay between each source in the VIPA is set by the thickness of the Fabry-Perot etalon. The more space between the reflective surfaces, the more time delay there is between each successive source. The tilt of the VIPA, illustrated in

Figure 4.2, allows light into the VIPA and provides an offset of each source from one another creating the vertical distance, *d*, between each source

$$d = 2t\sin(\theta_i), \tag{4.2}$$

where $t$ is the thickness of the VIPA and $\theta_i$ is the input angle. The reflectivity of the front of the VIPA is denoted by *R*, typically this reflectivity is chosen to be 100% and the reflectivity of the back reflector is denoted by *r*, typically around 98% this parameter is optimized to maximize resolution and VIPA efficiency in section 4.2 . The combination of the two reflectivities determines the intensity of subsequent images created inside the VIPA as described by equation (4.35).

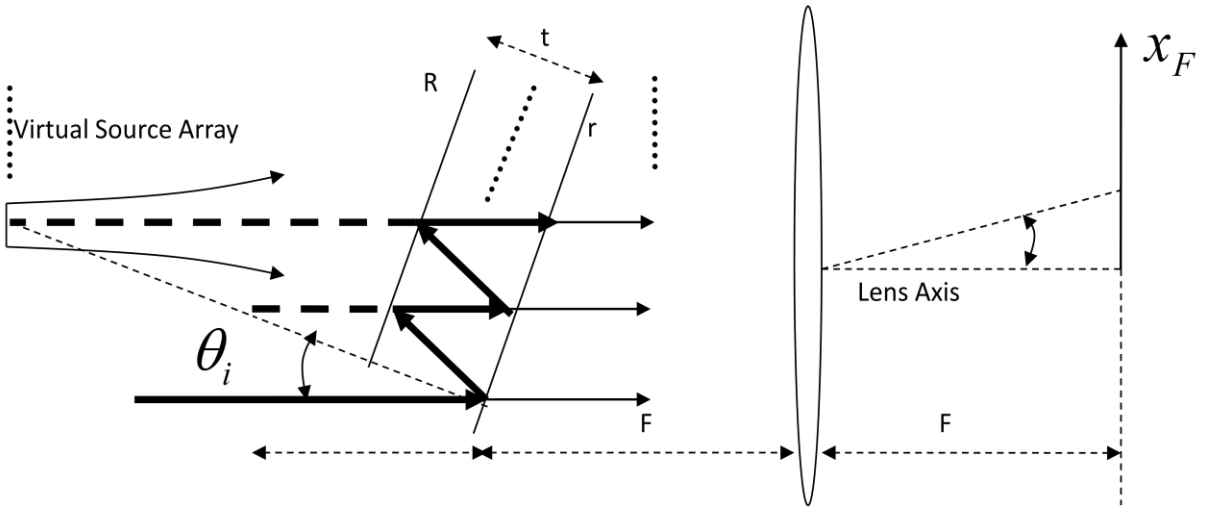


Figure 4.2: VIPA diagram showing how virtual sources are formed inside the VIPA.

The thickness of the VIPA along with the input angle determine the horizontal spatial distance between each image, or the additional space light must travel to form each successive image

$$\Delta z = 2t\cos(\theta_i) \tag{4.3}$$

The time it takes light to travel between images can also be thought of as the round trip time light travels inside the VIPA as described by,

$$T_{round} = \frac{2nt\cos(\theta_i)}{c} \tag{4.4}$$

where $n$ is the index of refraction of the material inside the VIPA and $c$ is the speed of light in a vacuum. The inverse of the time delay between images gives the free spectral range (FSR) of the VIPA:

$$FSR = \frac{1}{T_{round}} = \frac{c}{2nt\cos(\theta_i)} \tag{4.5}$$

Commonly, the FSR of the VIPA is chosen to be small (~25-100 GHz) in comparison to the large optical bandwidth (~20 THz) associated with ultra-short pulses. The periodic structure of the VIPA causes wavelengths separated by exactly the VIPA FSR to be imaged to the same location. This means in order to fully separate all frequencies from one another, a second spectrally dispersive device is necessary. A detailed analysis of this can be seen in section 4.4 . Further, due to the periodic nature of the images produced inside the VIPA, a single frequency is imaged at multiple angles. Similar to what is seen in the many diffraction orders from a simple grating, the VIPA too creates multiple orders in the axis the VIPA is tilted (vertical direction in Figure 4.3).

To transform the angular wavelength dependence of the VIPA output to position, $X_f$, a lens is placed a focal distance away from the VIPA. This produces an image a focal length away from the lens that has a positional dependence on wavelength. In addition to having the expected spectral dependence on position there is power dependence resulting from the imaging optics that form the VIPA output.

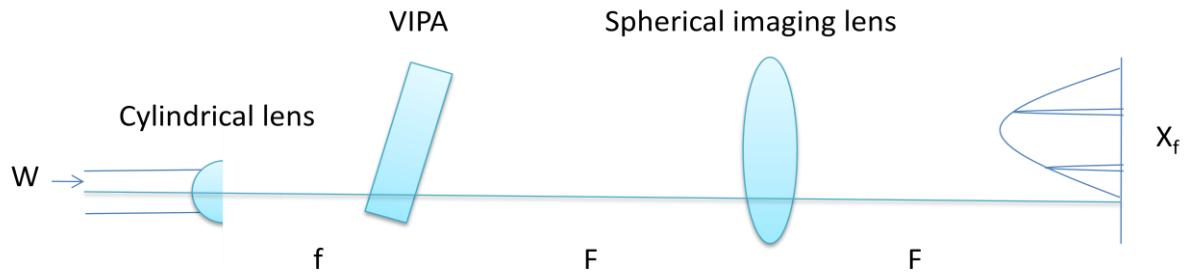


Figure 4.3: Diagram relating parameters necessary for calculating the envelope function of the VIPA output.

In Figure 4.3 *W* is the radius of the collimated input laser, *f* is the focal length of the cylindrical lens that focuses the input into the VIPA and *F* is the focal length of the spherical imaging lens. A cylindrical lens is used to at the input of the VIPA to create a line focus that when repetitively

imaged by the VIPA creates a collimated output from the VIPA, more detail on how this is produced can be seen in section 4.5 . A spherical imaging lens creates a wavelength dependent image a distance *F* after the spherical lens. The f-number of the spherical lens used is about 20 so spherical aberration in the Fourier plane is minimal. The envelope that defines how much power peak power is in each mode is

$$U = e^{\left(-\frac{2f^2 x_F{}^2}{F^2 W^2}\right)} \tag{4.6}$$

The intensity profile of the VIPA for infinite bounces, infinite number of virtual images inside the VIPA, is given by the paraxial wave model [32, 33] of a VIPA

$$I_{out}(x_F,\lambda) \propto \left|E_{out}(x_F,\lambda)\right|^2 \propto U \frac{1}{(1-Rr)^2 + 4(Rr)\sin^2\left(\frac{k\Delta}{2}\right)} \tag{4.7}$$

where

$$k = \frac{2\pi}{\lambda} \tag{4.8}$$

in free-space and

$$\Delta = 2t\cos(\theta_i) - \frac{2t\sin(\theta_i)x_F}{F} - \frac{t\cos(\theta_i)x_F{}^2}{F^2} \tag{4.9}$$

This intensity profile of the VIPA output can then be used to calculate the wavelength dependence. When the argument to the sine function is equal to some integer times *2π* the next VIPA FSR is imaged,

$$k\Delta = k\left[2t\cos(\theta_i) - \frac{2t\sin(\theta_i)x_F}{F} - \frac{t\cos(\theta_i)x_F{}^2}{F^2}\right] = 2m\pi \tag{4.10}$$

where *m* is an integer. The paraxial approximation

$$\frac{x_F}{F} \approx \theta_o \tag{4.11}$$

where $\theta_0$ is the output angle for some the central wavelength, $\lambda_{0,}$ yields

$$k\left[2t\cos(\theta_i) - 2t\sin(\theta_i)\theta_o - t\cos(\theta_i)\theta_o^{\,2}\right] = 2m\pi \tag{4.12}$$

By plugging in

$$m\lambda_0 = 2t\cos(\theta_i) \tag{4.13}$$

an expression for the VIPA angular dependence of wavelength can be derived

$$\Delta\lambda = \lambda - \lambda_0 = -\lambda_0\left[\tan(\theta_i)\theta_\lambda + \frac{1}{2}\theta_\lambda^{\,2}\right] \tag{4.14}$$

where $\theta_\lambda$ is the output angle of the VIPA for some wavelength $\lambda$. The resolution can then be calculated by taking the derivative of equation (4.14) with respect to the central wavelength, $\lambda_0$, which yields

$$\frac{d\theta_o}{d\lambda/\lambda_0} = -\frac{1}{\tan(\theta_i) + \theta_\lambda}. \tag{4.15}$$

This analysis can be extended for a solid VIPA where the internal angle, $\theta_{int}$, inside the VIPA is slightly different from the input angle, $\theta_i$, as calculated from Snell's Law

$$n_{air}\sin\theta_i = n\sin\theta_{\text{int}} \tag{4.16}$$

where $n$ is the index of refraction of the solid VIPA. The angular dependence of a solid VIPA [32] becomes

$$\Delta\lambda = \lambda - \lambda_0 = -\lambda_0\left[\frac{\tan(\theta_{\text{int}})\cos(\theta_i)}{n\cos(\theta_{\text{int}})}\theta_\lambda + \frac{1}{2}\frac{\theta_\lambda^{\,2}}{n^2}\right]. \tag{4.17}$$

Incorporating this internal angle for a solid VIPA into equation (4.15) yields the angular dispersion for a solid VIPA

$$\frac{d\theta_o}{d\lambda/\lambda_0} = -\frac{1}{\frac{\sin(2\theta_i)}{2\left[n^2-\sin(\theta_i)\right]}+\frac{\theta_\lambda}{n^2}}. \tag{4.18}$$

Note that equations (4.17) and (4.18) for a solid VIPA reduce to previous equations (4.14) and (4.15) when n=1 for an air spaced VIPA.

The intensity profile can be generalized for finite bounces to yield the following expression [32]

$$\mathrm{I}_{\mathrm{out,finite}} \propto U_{envelope}\frac{(1-(Rr)^b)+4(Rr)^b\sin^2\left(\frac{k\Delta}{2}\right)}{(1-Rr)^2+4Rr\sin^2\left(\frac{k\Delta}{2}\right)}, \tag{4.19}$$

where *b* is the number of bounces inside the VIPA calculated by the limited size of the VIPA by equation (4.26). By comparing the two expressions for the intensity profile of the VIPA equations (4.7) and (4.19), illustrated in Figure 4.6, it is evident that more images are created inside the VIPA. More images improve the resolution and intensity of the VIPA output. This is explained in detail in the next section where the intensity profile of the VIPA is used to optimize the VIPA design.

## 4.2 Design and optimization

Using the theory outlined in the previous section, a solid fused silica VIPA is designed to have enough spectral resolution to resolve the individual comb lines separated by 890.4 MHz. Many parameters must be considered – the chosen thickness *t*, the reflectivities, *R*, *r* and the window size of the VIPA.

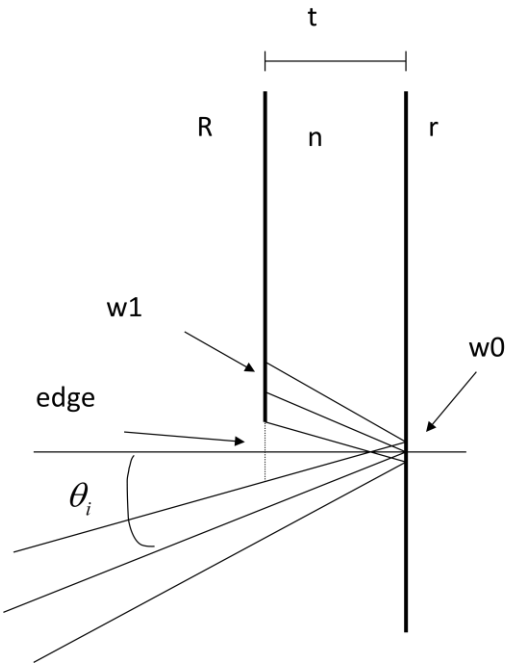


Figure 4.4: VIPA input window detail.

The edge of the window that allows the input into the VIPA is very important as it determines the smallest input angle to the VIPA. With a smaller input angle, more virtual images are created inside the VIPA, and therefore the resolution of the VIPA is higher and there is more power in the resolved peaks. Typical fabrication techniques dictate that the window edge will have a transition length of approximately 100 μm (at the company Precision Photonics), meaning that it takes 100 μm to transition between having no reflective edge to having the designed *R* reflectivity of the back surface see Figure 4.4. Gaussian beam propagation is used to calculate the radius of the beam at the edge $w_1$ as compared to the radius of the image at the focus, $w_0$

$$w_1 = w_0 \sqrt{1 + \left( \frac{t}{z_0} \right)^2} \tag{4.20}$$

where

$$z_0 = \frac{n\pi w_0^{\,2}}{\lambda} \tag{4.21}$$

To maximize the number of images the beam waist at the window edge needs to be minimized. The smaller $w_1$ is the more images that can be packed into the limited size of the VIPA resulting in higher efficiency and resolution of the VIPA. This happens when the thickness of the VIPA, *t*, equals the Rayleigh range of the input beam.

$$t = z_0 = \frac{n\pi w_0^{2}}{\lambda} \tag{4.22}$$

Since any loss of light from the first reflection at $w_1$ is propagated to all the VIPA images it is important to not clip this first spot. Clipping of the first spot can be reduced by minimizing $w_1$. The smaller $w_1$ is, the smaller the input angle into the VIPA can be without losing light from the window edge. Solving for $w_0$ results in the ideal spot size:

$$w_0 = \sqrt{\frac{t\lambda}{\pi n}} \tag{4.23}$$

Using this value for $w_0$, $w_1$ is calculated to be the expected value for the waist a Rayleigh range away from the $w_0$

$$w_1 = \sqrt{\frac{2t\lambda}{\pi n}} = w_0\sqrt{2} \tag{4.24}$$

This is left as an expression in terms of VIPA thickness, *t*, so the resolution of the VIPA can be studied as a function of VIPA FSR. The spot size along with the length of the transition of the edge of the window, *h*, yields the vertical separation of images inside the VIPA:

$$x = 2w_1 + h \tag{4.25}$$

This places the 1/e value of the Gaussian spot $w_1$ at the edge where the window fully transitions to being 99.9% reflective. The length of the VIPA, *L*, is another parameter that is set by the

limitations of the fabrication of the VIPA at Precision Photonics. The more variance there is in how parallel the two reflective surfaces are to one another, the larger the resolved mode shape of the VIPA output. To reduce this variance to λ/10 and keep fabrication costs reasonable, the length of the sides is set to 1 cm. Larger structures can be produced at additional costs and larger tolerance (λ/5) in the parallelism between the two reflective surfaces. From this, the number of images, *b*, produced inside the VIPA is calculated by

$$b = \frac{L}{x} = \frac{L}{2w_1 + h}. \tag{4.26}$$

The VIPA output intensity and resolution are calculated for varying FSR and *r*. Using equation (4.19) the output intensity of the VIPA is plotted as a function of FSR in Figure 4.5. The larger the FSR, the smaller the thickness of the VIPA which results in a smaller waist ($w_1$) after traveling through the VIPA. This means the VIPA can be placed at a smaller angle and more images are created inside the VIPA, and as shown in Figure 4.5 a more intense output is the result.

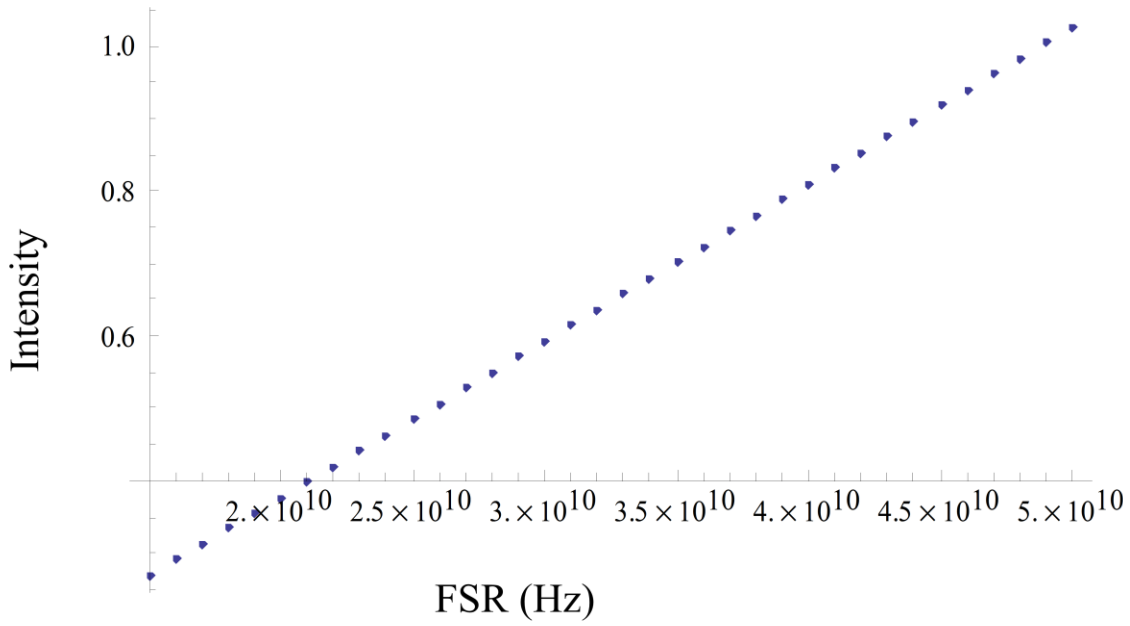


Figure 4.5: VIPA output intensity as a function of FSR. Output intensity is normalized to the intensity of the VIPA output with a 50 GHz FSR. Plotted with back reflectivity, $r = 0.985$

The increase in output intensity with increasing VIPA FSR must be balanced with the loss in resolution. A plot of equation (4.14) with varying FSR shows decreasing resolution with increasing FSR, see Figure 4.6. Note, resolution is measured in frequency and the larger the value the larger the FWHM resolved modes, the worse the resolution. In order to resolve adjacent modes separated by 1 GHz, a resolution of at least 500 MHz is necessary. Of course this assumes that the VIPA is made perfectly to design specifications; even a slight error in the parallelism of the two reflective surfaces has an adverse affect on the resolution. Further, having higher resolution allows the modes to be better separated from one another which reduces the amount of cross-talk between adjacent modes. For these reasons the VIPA was designed to have a resolution, $\Delta\nu$, of 250 MHz, corresponding to a FSR of 25 GHz as shown by the finite bounce calculation in Figure 4.6. From this the Finesse of the VIPA is $F = FSR / \Delta\upsilon = 100$.

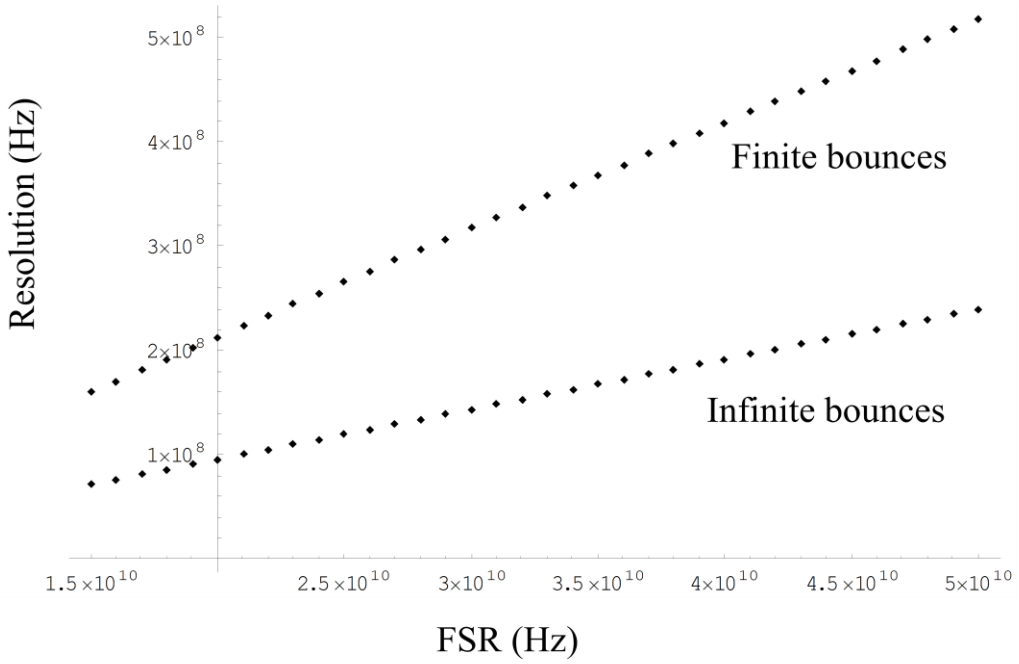


Figure 4.6: VIPA resolution as a function of FSR. Both finite and infinite bounce calculations are shown with varying FSR.

This provides more than enough resolution to resolve adjacent modes at 1 GHz with margin for fabrication imperfection without suffering too much loss as shown by the output intensity Figure 4.5. Other solid VIPAs have been designed at 50 GHz and typically have 6 db of insertion loss, meaning for a VIPA at 25 GHz using equation (4.19) there is about half the total intensity as for a 50 GHz VIPA. This additional 3 db of loss for the 25 GHz VIPA means the 25 GHz VIPA has an estimated insertion loss of 9 db.

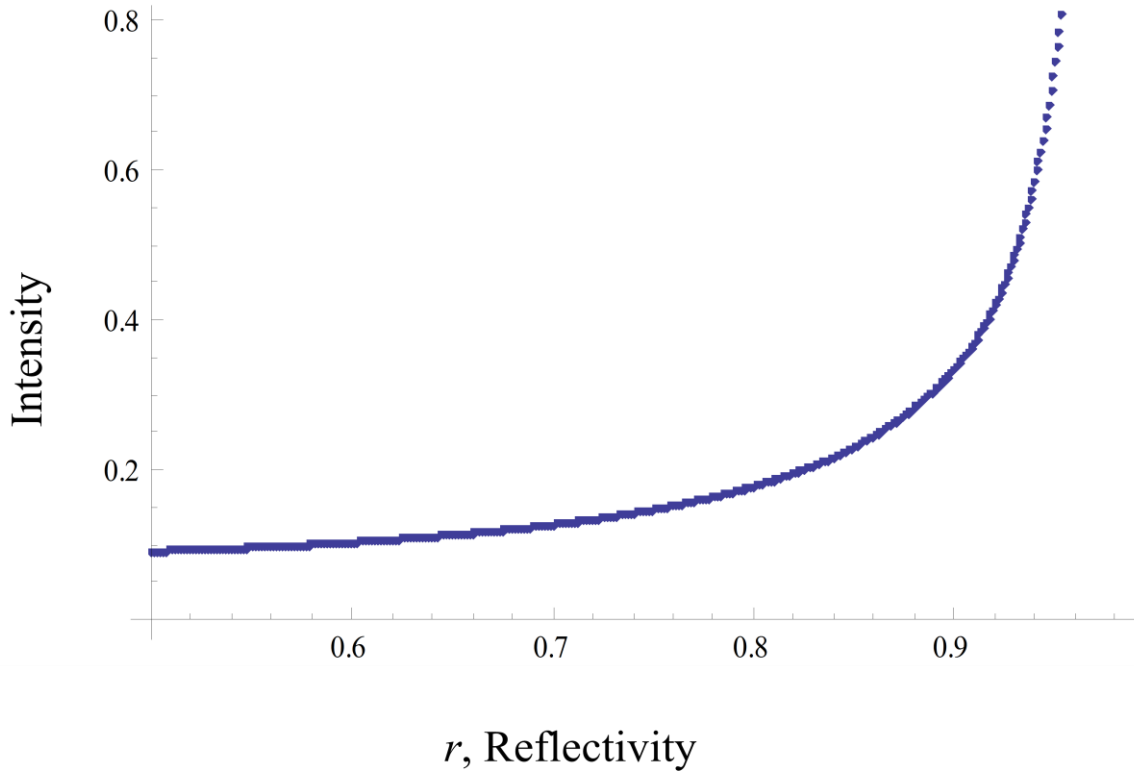


Figure 4.7: VIPA output intensity as a function of back surface reflectivity, *r*. VIPA output intensity is normalized to the output intensity when $r = 1$. The FSR is set to 25 GHz.

Another parameter to be considered is the reflectivity of the output surface of the VIPA, *r*. Increasing *r* increases the output intensity as shown in Figure 4.7. However increasing *r* also reduces resolution of the output as shown in Figure 4.8. Therefore a compromise must be made between output intensity and resolution. Since the output intensity grows as the reflectivity *r* approaches 1, *r* needs to be as large as possible but not so large that the resolution of the VIPA gets larger than the necessary 250 MHz. With the FSR set to 25 GHz, the largest value for *r* that can be chosen to yield the necessary 250 MHz resolution is $r = 0.985$.

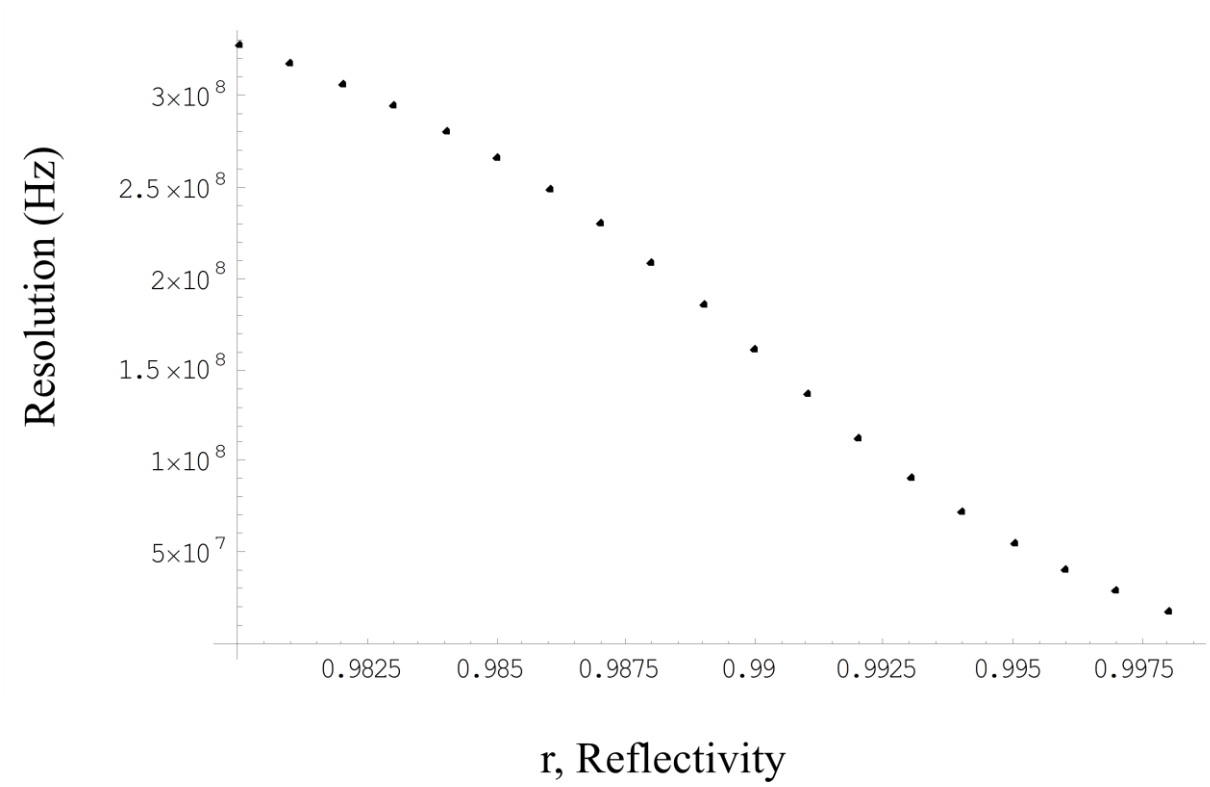


Figure 4.8: VIPA resolution as a function of back surface reflectivity, *r*. The FSR is set to 25 GHz

Combining design constraints set by Precision Photonics fabrication techniques along with the calculated optimizations creates the overall VIPA design. The solid fused silica VIPA is 10 mm wide by 10 mm high. With an index of refraction for fused silica of 1.453 at 810nm a thickness of 4.13 mm is necessary to get a FSR of 25 GHz with an optimal input angle of 1.21°. As a result of a fabrication error, the thickness of the VIPA is slightly thicker than the necessary 4.13 mm necessary to achieve a 25 GHz VIPA. The measured FSR is 24.931 GHz at 810 nm; the additional thickness is calculated to be approximately 11.4 μm using equation (4.5). The transition between the high reflector and window on the input surface is less than 100 μm. Thus the optimal spot size to maximize light coupled into the VIPA $w_0$ is calculated to be 27.1 μm and

the waist at the back reflector $w_1$ = 38.3 μm. 56 virtual images are produced inside the VIPA as calculated from $w_1$ and the length of the VIPA using equation (4.26). The reflectivity of the output surface was designed to be 98.5% while the input side is over 99.9% reflective. These parameters result in a theoretical resolution of 250 MHz and an estimated 9 db insertion loss.

## 4.3 Measuring VIPA resolution

To validate the design of the VIPA the resolution of the VIPA was tested. One method to measure how well different wavelengths are separated from one another is to image the output of the VIPA onto a single mode fiber and use a tunable continuous wave (CW) source [33]. When the wavelength is varied, the location of the imaged spot is shifted as a result of the wavelength dependence of the VIPA and the geometry of the setup. By monitoring the optical power coupled into the single mode fiber as a function of wavelength, the resolving power of the VIPA can be tested.

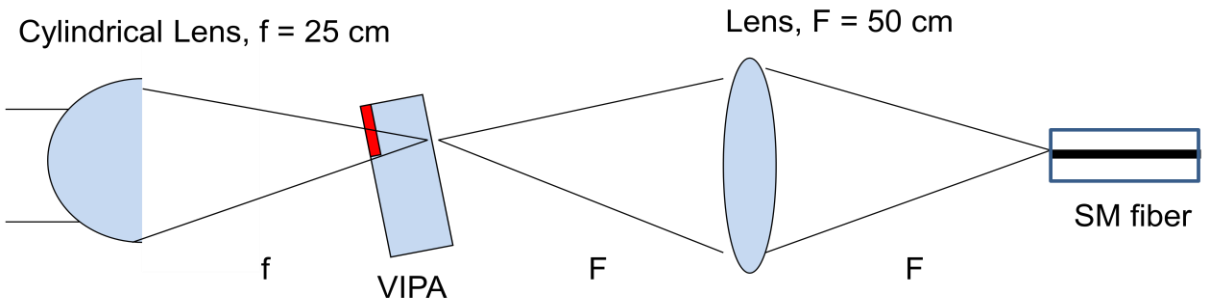


Figure 4.9: VIPA resolution measurement setup

The layout of the VIPA measurement setup is illustrated in Figure 4.9. A collimated 5 mm diameter beam is focused into the VIPA tilted at 1.21° using a 25 cm focal length cylindrical lens (corresponding to an f number of 50 to reduce aberrations). The output of the VIPA is then imaged by a 50 cm focal length lens placed 50 cm from the VIPA and 50 cm before the fiber.

By using a Toptica DL 100-L external cavity laser diode as a light source one can make small changes to the wavelength of the laser diode by adjusting the current through the diode. The wavelength being imaged by the VIPA is monitored using a Burleigh Wavemeter WA-100.

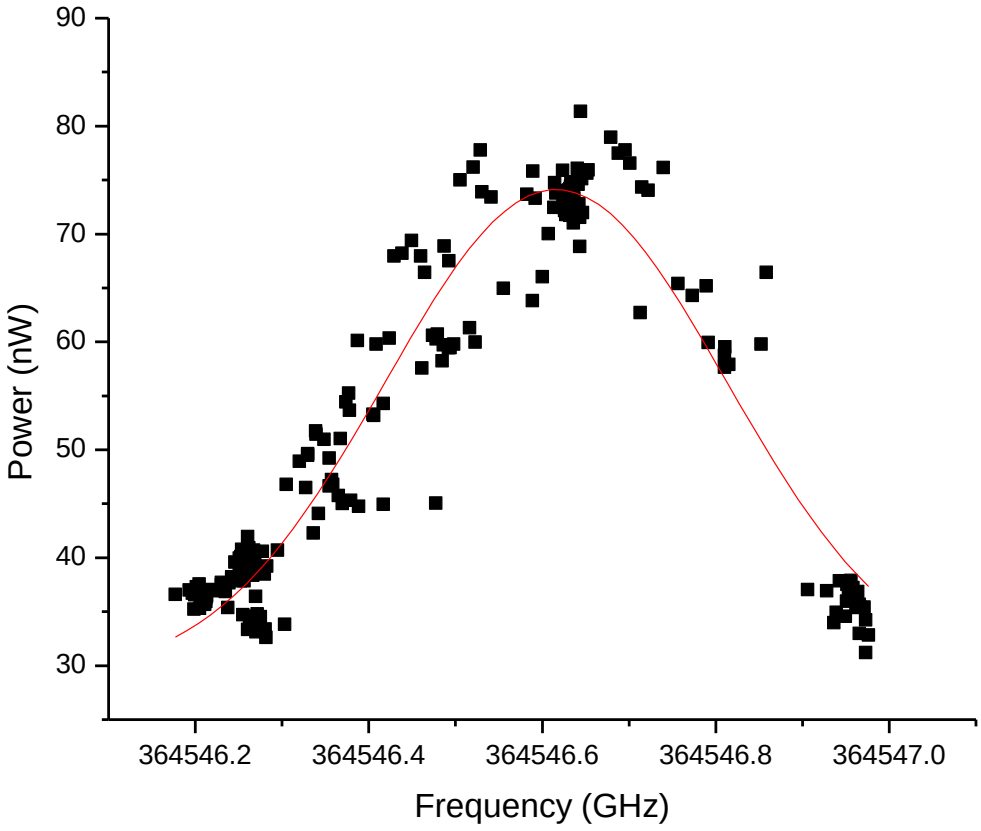


Figure 4.10: VIPA resolution measurement. Black squares represent data points of measured power through detection fiber as a function of frequency. The red line is a Gaussian fit to the data with a FWHM of 393 MHz. The Gaussian function does not go to zero due to an offset in the measured power of approximately 30 nW.

Figure 4.10 shows the results of monitoring the power coupled into the fiber as a function of frequency of the laser. Due to mode hops in the external cavity laser diode, it is difficult to continuously tune wavelength; hence why Figure 4.10 shows clusters of data grouped near specific frequencies as well as gaps in measured frequencies. Although the resulting plot represents a convolution of the Gaussian mode accepted into the fiber and the actual resolved

VIPA mode, the VIPA mode is quite large in comparison to the core of the SM fiber. The VIPA mode is 88 μm wide in the *y* axis and 572 μm wide in the *x* axis due to the asymmetric mode shape of the VIPA output. The fiber core is only 5.6 μm in diameter. The large mode shape is the expected size given the 50 cm focal length lens used to view the Fourier plane of the VIPA. This mode shape is by design so the accepted light into the fiber can be approximated as a delta function which when convolved with the VIPA mode simply returns the VIPA mode itself. The small core size in comparison to the mode size is also the source of huge loss in the measured spot, hence why the measured power is so low in comparison to the source. The red line in Figure 4.10 is a Gaussian fit to the data with a FWHM of 393 MHz with a reasonable R-squared value of 0.92. Obviously, this measured resolution is worse than the ideal calculated resolution of 250 MHz. This discrepancy is likely due to the tolerance in the parallelism of the two reflective surfaces of the VIPA (λ/10). The angular wavelength dependence of the VIPA is dependent upon the array of virtual images spaced a regular distance apart from one another with a regular time delay. Any change in the parallelism of the VIPA changes both of these parameters and results in a single wavelength being output at several angles or in other words, a blurring of the ideal spot width. An alternate method for measuring the resolution of the VIPA is carried out in the following section where the individual comb lines of an 890.4 MHz repetition rate laser are imaged onto a charge coupled device (CCD) camera.

## 4.4 Imaging the 2-D spectral brush at 890 MHz

The high spectral resolution setup shown in Figure 4.11 uses two spectrally dispersive elements to resolve the individual lines of an 890 MHz frequency comb. The input pulse train is focused by a 25 cm focal length cylindrical lens into the window of the VIPA designed in section

4.2 . While a VIPA provides very high spectral resolution, it overlaps comb lines separated by integer multiples of the FSR [34]; if individual comb lines are to be resolved, another dispersive element is necessary. A grating is used to separate the repeated modes of the VIPA, where the dispersive directions of the grating and VIPA are orthogonal. The grating must have a resolution better than 25 GHz = 0.05 nm at 800 nm in the horizontal direction ($x$) to resolve the repeated modes of the VIPA. To achieve this resolution for a grating with 1200 lines/mm, at least 12 mm of the grating must be illuminated. This requirement is met by inserting a horizontal beam-expanding telescope before the grating. It is important to avoid expanding the beam in the

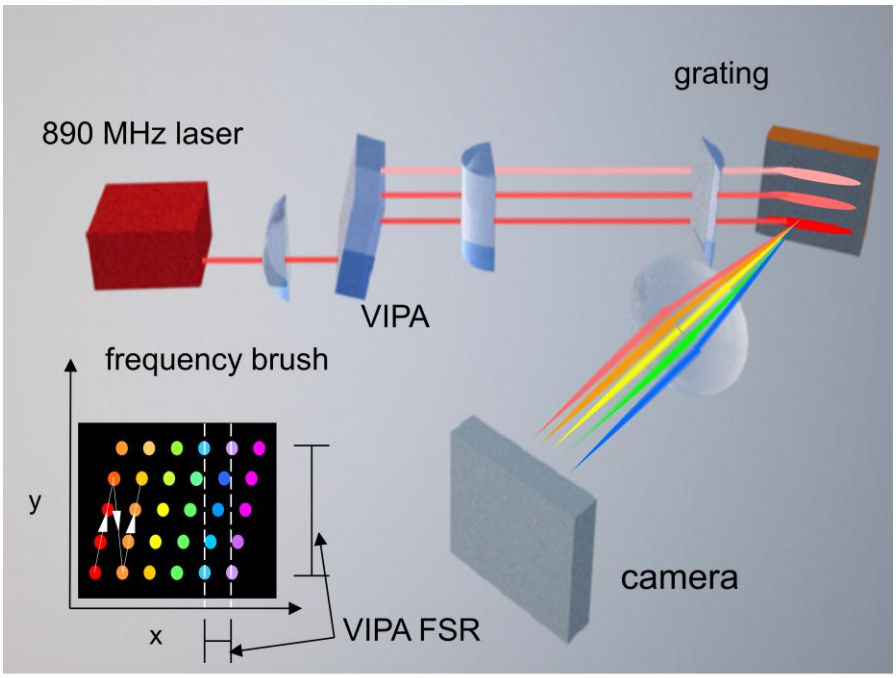


Figure 4.11: The high resolution 2-D setup resolves individual comb lines spaced by 890.4 MHz. The VIPA with a FSR of 25 GHz separates adjacent comb lines in the $y$ direction and the grating separates repeated orders of the VIPA along the $x$ direction. The white arrows show adjacent comb lines with increasing frequency.

vertical direction ($y$) after the VIPA as expansion before the spherical imaging lens affects the separation of comb lines in $y$. For this reason, cylindrical lenses, separated by the sum of their focal lengths (10+100=110 cm), are used to expand the beam by a factor of 10 in the horizontal

direction only. Finally, the light from the grating is imaged with a 50 cm focal length spherical lens onto a CCD camera. Figure 4.12 is an image of these individually resolved frequencies. Using the fine resolution of the VIPA to separate adjacent comb lines in *y* and the coarse resolution of the grating to separate repeated modes of the VIPA in *x*, a two-dimensional frequency 'brush' is created [35, 36, 37].

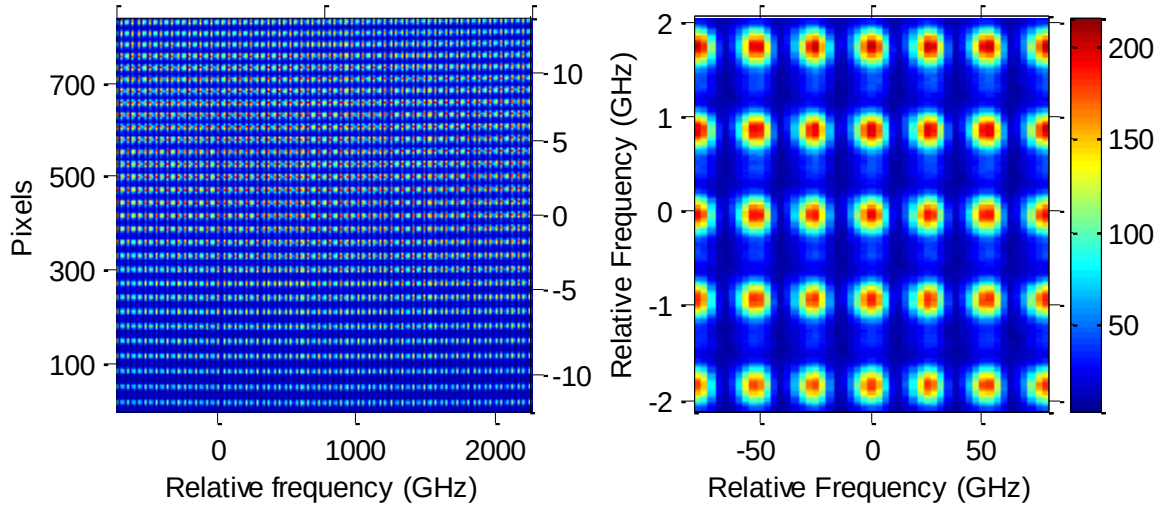


Figure 4.12: Images showing a frequency brush of the resolved discrete frequencies of an 890 MHz pulse train. The image on the left shows the entire VIPA FSR and the image on the right shows a zoomed-in section of the spectrum.

### 4.4.1 Measuring VIPA FSR using the 2-D brush

The FSR of the VIPA can be measured very accurately in the 2-D brush setup when imaging the spectral brush of a source with a known repetition rate. Since the frequency spacing of a pulsed source is so regular, $f_{rep}$, the spacing between modes can be used as a standard. The regular grid-like pattern in Figure 4.12 is no accident; in fact the repetition rate of the input titanium sapphire laser was tuned to be exactly 1/28th of the VIPA FSR in order to generate such a pattern. When the FSR is exactly an integer number of modes ($N$) times $f_{rep}$, the 2-D setup images a regular grid; thus the FSR can be measured,

$$FSR = Nf_{rep} \tag{4.27}$$

However, if the FSR is a non-integer times $f_{rep}$ the grid becomes skewed. When the grating resolves a repeated order of the VIPA in the horizontal direction (every VIPA FSR), if there is a non-integer number of $f_{rep}$ in the VIPA FSR there will be a shift in $y$ as well as the shift in $x$ from the grating. This results in a grid with a slope in the horizontal lines as illustrated in Figure 4.13.

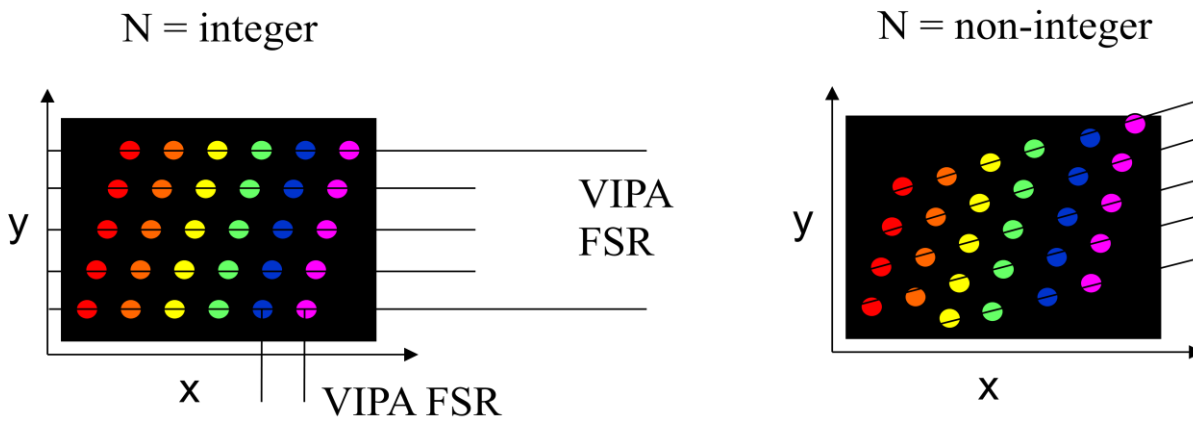


Figure 4.13: Effects of having an integer and non-integer number of $f_{rep}$ in the VIPA FSR. Observe how a non-integer number forms a slanted grid while when the $f_{rep}$ is tuned to exactly 1/N of an integer, a regular grid is formed.

Small changes in the repetition rate of the laser have a noticeable effect on this pattern, a change in $f_{rep}$ of merely 10 kHz is enough to be measureable. Because the slant of the grid is very sensitive to the repetition rate of the laser, the repetition rate of the source laser can be tuned while monitoring the slant of the grid; only when the FSR of the VIPA is an integer number of $f_{rep}$ does the grid become horizontal. In other words the modes align themselves with the $x$ and $y$ axis set by the dispersion directions of the grating and VIPA respectively. Using equation (4.27) the FSR of the VIPA can be calculated to within 10 kHz*N = 280 kHz. This effect is also sensitive enough to observe effects of dispersion on the VIPA FSR as elaborated in section 4.7 .

### 4.4.2 2-D brush calibration

A tunable continuous wave (CW) laser is used to calibrate the frequency sensitivity, measure the resolution and analyze the crosstalk between frequency modes of the brush image. First, the frequency sensitivity of the brush image can be calculated by measuring the number of pixels between repeated orders of the VIPA in the *y* axis. Figure 4.14 shows an image of the camera imaging a single CW frequency. Dividing the known VIPA FSR (measured to be 24.93 GHz at 810nm in section 4.4.1 ) by the number of pixels between the two peaks (702 pixels) yields the average frequency sensitivity (28 pixels / GHz).

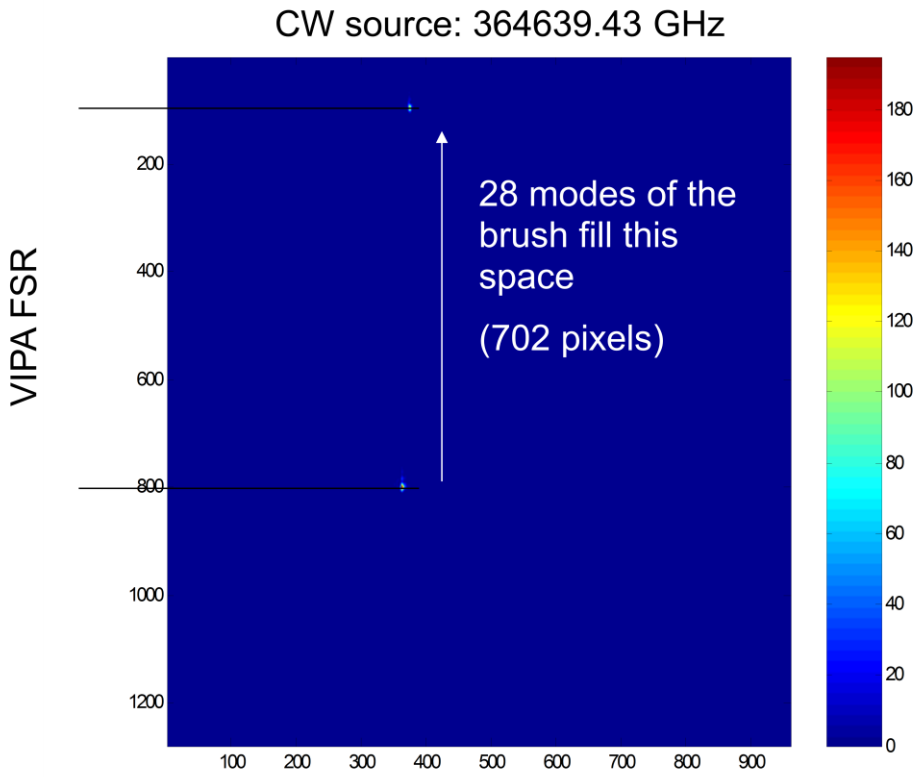


Figure 4.14: Camera image of a CW source. The vertical space between the two spots corresponds to one VIPA FSR. By dividing the known VIPA FSR by the measured number of pixels between the two peaks, an average frequency sensitivity is calculated to be 28 pixels / GHz.

Next, the spectral resolution can be measured from the FWHM of the lineshape. The FWHM in Figure 4.15 is 10 pixels, which corresponds to a resolution of 357 MHz. Finally, by comparing two wavelengths separated by the comb spacing, 890 MHz, the crosstalk between adjacent comb lines can be estimated. As seen in Figure 4.15, each line has a tail toward higher frequency (for reference, the tail can be seen in the brush in Figure 4.12, the tail of a lower frequency comb line almost touches the higher frequency comb line directly above it). This asymmetric tail, also visible in other publications [33], is a result of the asymmetric power dependence of the array of VIPA images. For more details see section 4.5 . This tail is the main cause of crosstalk between modes. 4% of the peak intensity of each comb line appears at the location of the adjacent higher frequency line. In contrast, each mode only images 0.5% of its peak power to the adjacent comb line lower in frequency.

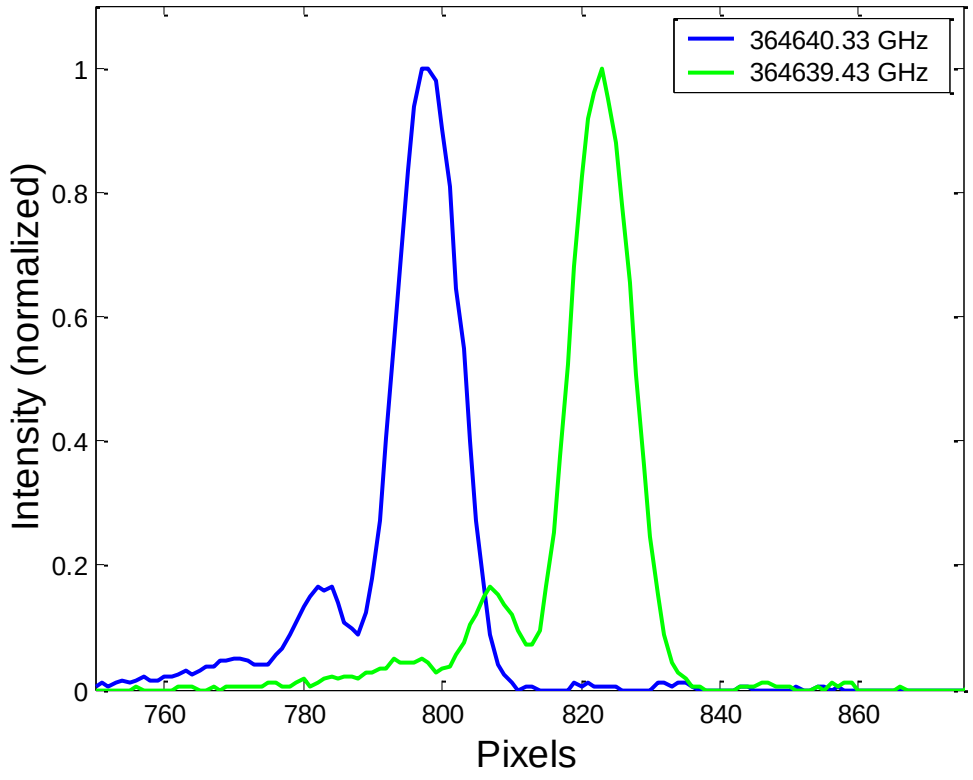


Figure 4.15: Camera image slices of two CW sources separated by 900 MHz. The resolution of the VIPA is apparent in the width (357 MHz) of each resolved mode. Also, the amount of cross-talk between adjacent modes can be measured. 4% of the peak power is imaged to the adjacent mode of higher frequency.

## 4.5 VIPA mode shape analysis

To explore the non-ideal effects of the VIPA as well as to verify the approximations made in the optical design, a simulation was made. The model (code can be seen in appendix B) works with one CW frequency at a time and constructs the VIPA by creating a tilted array of Gaussian modes. This is done by constructing the electric field as a function of *z*, beam propagation direction, and *y*, plane of the VIPA tilt. Since the behavior of the VIPA is the same in the *y* axis, this simulation only maps out a 2-D electric field. A single Gaussian mode takes the form

$$E(z_0, y) = e^{-\frac{(y-y_0)^2}{w_0^2}} \tag{4.28}$$

where $x_0$ is the location in $y$ and $z_0$ is the location in $z$ of a Gaussian mode with a width of $w_0$ in $y$. Using values for ideal VIPA performance calculated in section 4.2 such as spot size and VIPA input angle, the location of each Gaussian mode is placed as the simulation steps forward in $z$. At every step the simulation calculates the diffraction and refraction of the electric field to calculate the next slice in $z$ as the beam propagates. The electric field at the next slice of $z$ from diffraction is

$$E(z + \Delta z, y) = E(z, y) * e^{-jk_z \Delta z} \tag{4.29}$$

where * stands for the convolution, $\Delta z$ is the step size in the $z$ direction, and $k_z$ is wave vector in the $z$ direction given by

$$k = \sqrt{k_0^2 + k_x^2} \tag{4.30}$$

where wave vectors $k_0$ and $k_y$ are given by

$$k_0 = \frac{2\pi}{\lambda} \tag{4.31}$$

and

$$k_y(y) = \frac{2\pi n(y)}{Y} \tag{4.32}$$

where $Y$ is the total distance simulated and $n(y)$ describes the index of refraction as a function of $y$. In the simulation the convolution at each step is performed by taking the fast Fourier transform (fft) of both E and $e^{-jk_z \Delta z}$ then multiplying the two together before taking the inverse Fourier transform to reconstruct the E of the next slice. Note the simulation is written in Matlab and it is very important that shifts are performed to properly take the convolution of the two

signals. For more details on this, see the simulation source code in appendix B. Finally, the effects of refraction are then taken into account by

$$E(z+\Delta z, y) = E(z, y)e^{-\frac{j2\pi\Delta z n(y)}{\lambda}}. \tag{4.33}$$

This refraction is how the imaging lens is simulated. 75 cm after the last image of the VIPA the effect of a lens is given by

$$E(z+\Delta z, y) = E(z, y)e^{-\frac{j2\pi y^2}{\lambda(2f)}} \tag{4.34}$$

where f is the focal length of the lens. Figure 4.16 shows the 2-D electric field as the angled array of Gaussian modes interfere with one another. The tilted array of Gaussian modes is imaged by a thin lens at the red line to form spots in the Fourier plane at the blue line. Note only a CW source is used. This means each spot formed in the Fourier plane is an order of the VIPA.

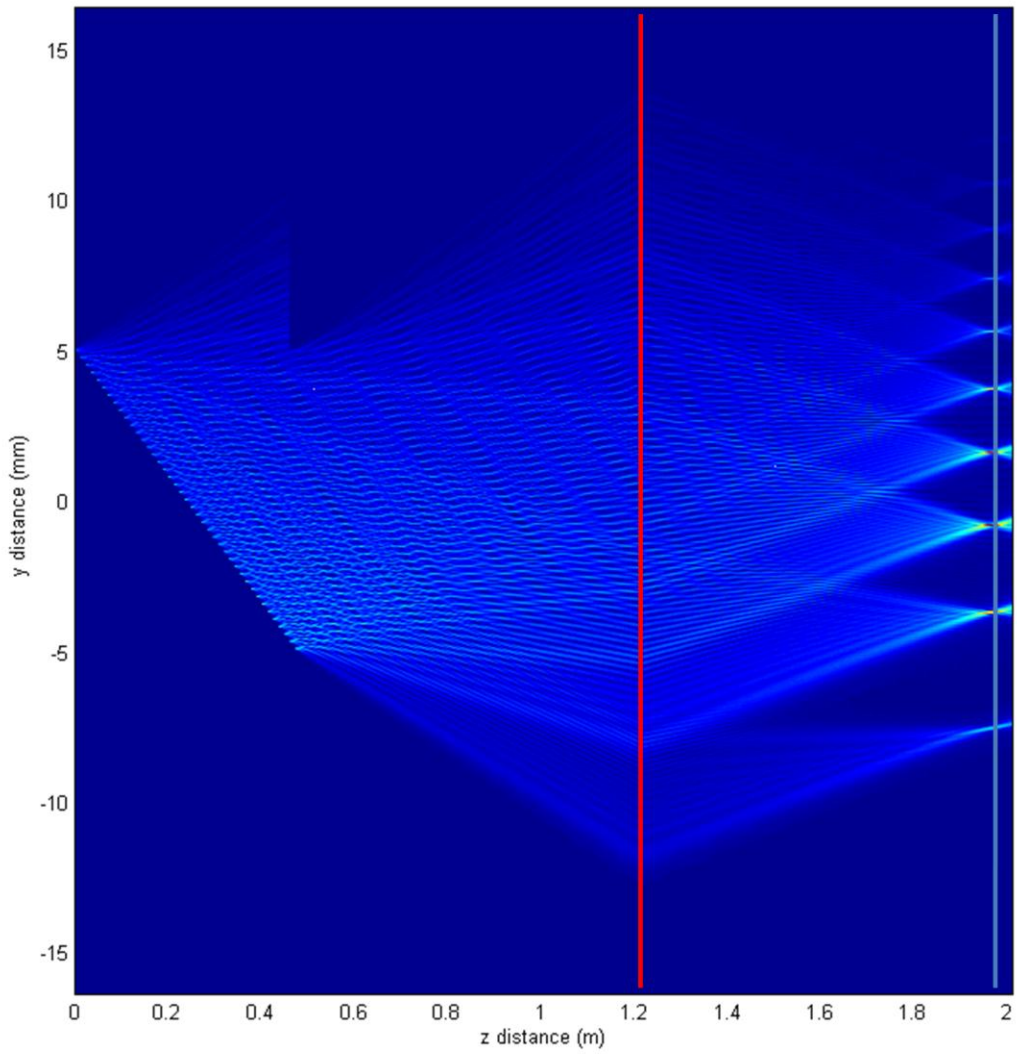


Figure 4.16: VIPA simulation: 810 nm CW light is dispersed by the VIPA and imaged using a 75 cm focal length spherical lens. The red line emphasizes the location of the spherical lens 75 cm after the last VIPA image and 75 cm before the Fourier plane shown by the blue line.

The edge of the VIPA is simulated by multiplying the electric field at the output of the VIPA by a mask that only passes light within the length of the VIPA, 1 cm in the *y* axis. Light that extends past the finite size of the VIPA is reflected out the top of the VIPA and is lost. The mask in the simulation effectively simulates this effect by eliminating light lost by the edge.

The Fourier plane shown by the blue line in Figure 4.16 shows where the CW input to the VIPA forms images. Each spot is another order of the VIPA. The expected nonlinear dispersive behavior of the VIPA is evident in the change in distances between these VIPA orders. A similar spreading of the modes is evident inside each order when multiple frequencies are plotted.

By running the simulation for two different CW wavelengths and plotting a slice of the electric field at the Fourier plane (blue line in Figure 4.16), the separation and mode shape of the resolved modes is investigated. Figure 4.17 shows the slice of the modes at the Fourier plane. The two CW wavelengths are chosen to have a separation of 890.4 MHz, the same as the repetition rate of the laser. Details of the center VIPA order shown in Figure 4.18 illustrate the asymmetric mode shape seen in the experiment.

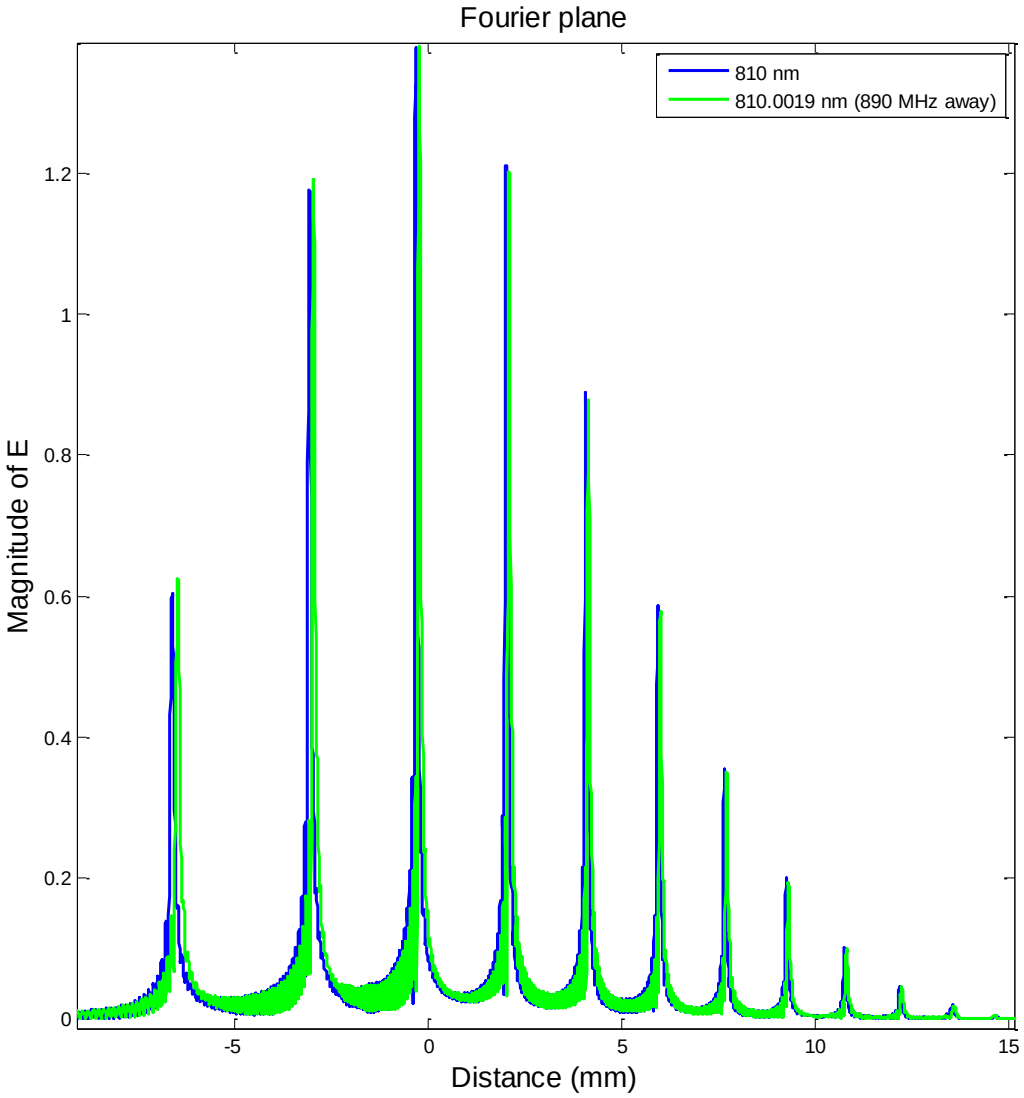


Figure 4.17: Full image plane of two frequencies showing how modes separated by 1 GHz are dispersed by the VIPA.

Observe the array of Gaussian sources in Figure 4.16, sources closer to the top of the array are weaker than spots at the bottom. This is due to the reflectivity of the two surfaces of the VIPA. The reflectivity of the output surface, *r*, is 98.5% while the input surface reflectivity,

R, is 99.9%. As the spots are created inside the VIPA light is lost so the intensity of the images gets successively weaker. The intensity of the $n^{th}$ image is

$$I_n = I_0 (rR)^n \tag{4.35}$$

where $I_0$ is the intensity of the first image. This asymmetry in the intensity of the array of images that form the VIPA is the source of the asymmetry in the mode shape. Simulation results show that the asymmetry in the mode shape is directly related to the reflectivity chosen for the VIPA. Higher reflectivity reduces the asymmetry of the mode shape as all Gaussian spots become more identical, while reducing the reflectivity exaggerates the asymmetry of the resolved spots from the VIPA.

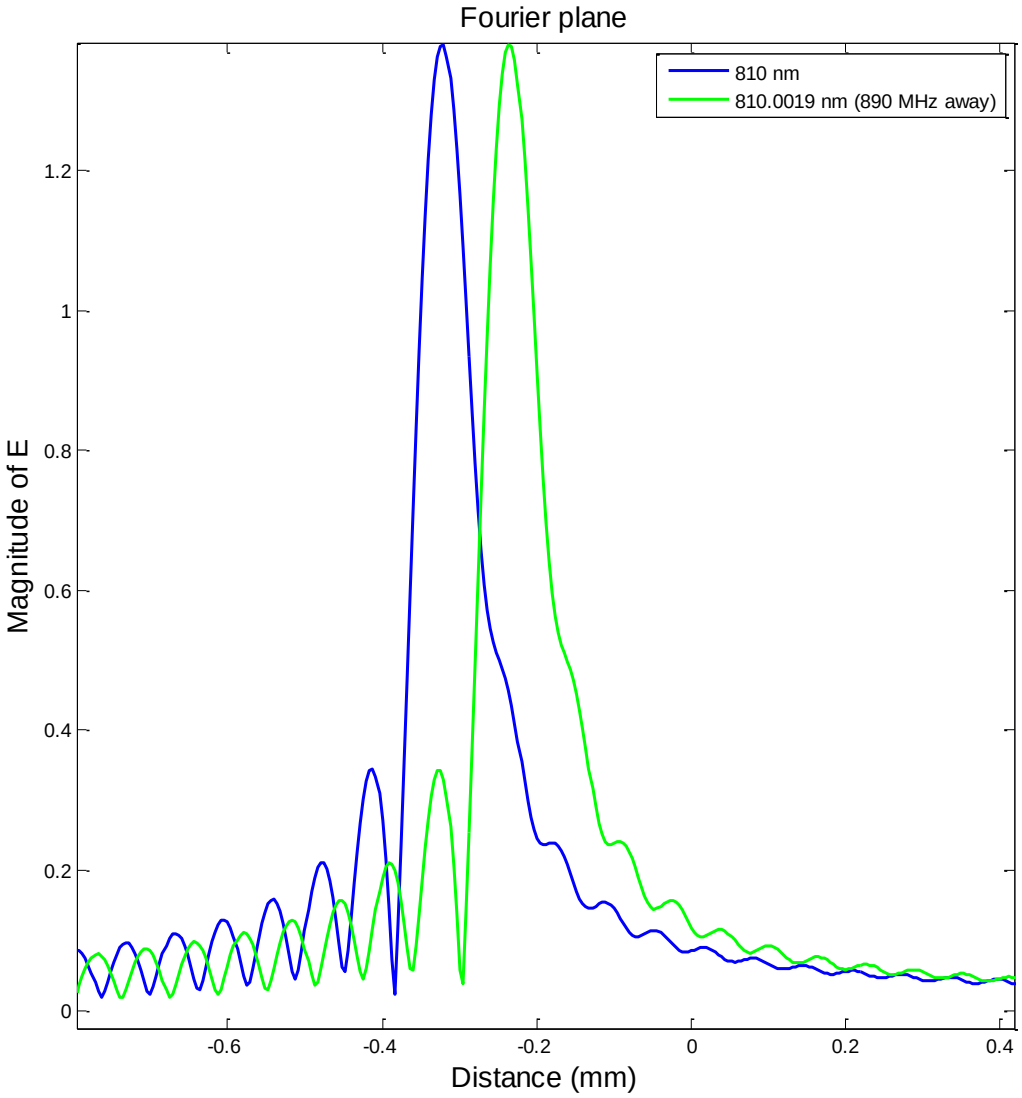


Figure 4.18: Close up of how well resolved the two frequencies are separated from one another in the first order of the VIPA.

## 4.6 Non-linear output analysis

Careful inspection of the entire VIPA FSR brush image in Figure 4.12 reveals that modes near the bottom of the image are farther apart from one another in comparison to modes near the top of the image. Although these modes are equally spaced in frequency, the paraxial dispersion

equation for the VIPA output angle has a nonlinear dependence on frequency [32]. To verify that the spacing between modes is as expected, the brush data is fit to the expected dispersion relation equation (4.14). This fit is done by first taking a vertical slice of the brush to measure the separation between modes dispersed by the VIPA as shown in Figure 4.19.

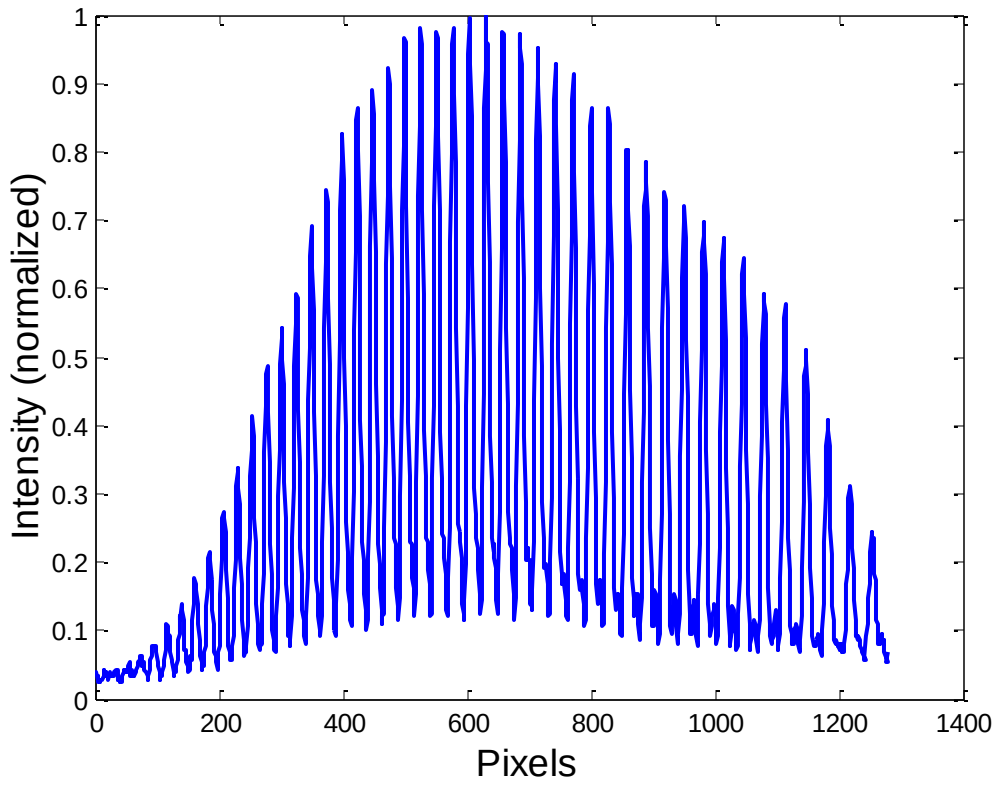


Figure 4.19: Vertical slice of the camera image following peaks of 890.4 MHz spectral brush. Observe how these peaks of regular frequency spacing ($f_{rep}$) are not equally spaced in the *y*-axis of the image. This expected effect is described by the non-linear dispersive behavior of the VIPA derived from paraxial wave theory [32,33].

The physical peak position of each mode is found by finding the maximum value of each peak. Then the location of each peak is measured by multiplying the size of each pixel, 4.65 μm, by the number of pixels it is away from a starting peak. This position is then converted into the angle that the mode left the VIPA by using the thin lens approximation for a lens and standard ray tracing formalism. Since this analysis only considers the vertical effects of the VIPA

dispersion, there is no need to take the horizontal beam expanding cylindrical lenses into account. The array of peak angles are given corresponding wavelengths since the spacing of each mode is known to be $f_{rep}$ = 890.4 MHz. The center frequency is set to 808 nm and each mode is separated by 890.4 MHz = 0.0019 nm (at 808 nm). Figure 4.19 shows a plot of the measured wavelength versus angle as well as a fit to the paraxial VIPA dispersion equation (4.14). The fit yields an angle of incidence of 1.0102° which is consistent with the measured angle of incidence of 1.01°.

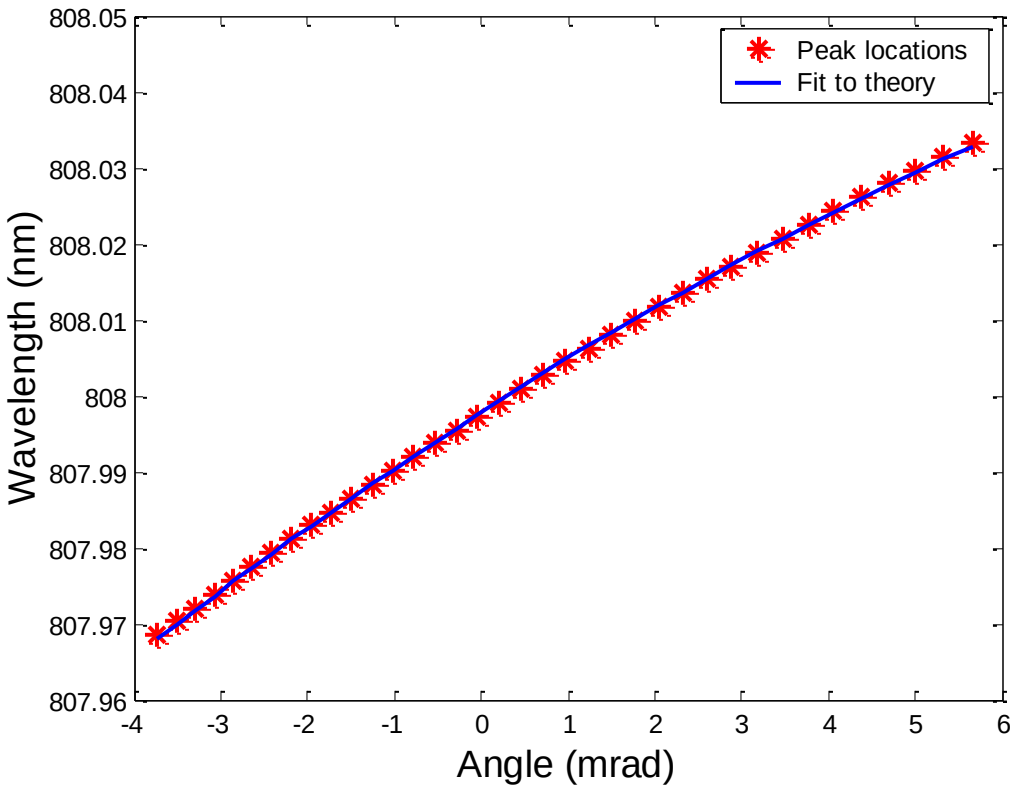


Figure 4.20: VIPA output wavelength vs. angle showing the expected non-linear behavior as described by the paraxial wave theory of VIPA dispersion [32,33].

## 4.7 Solid VIPA dispersion effects

The dispersion of fused silica inside the solid VIPA results in a wavelength dependence of the FSR of the VIPA. While this effect is small over narrow regions of the spectrum (what is captured by the camera), when imaging the full spectrum (40 nm FWHM as seen in Figure 2.5), this effect is significant and cannot be ignored. The camera in the 2-D brush setup images approximately 100 VIPA orders or 2500 GHz which corresponds to merely 5.7 nm. While ideal VIPA-based pulse shapers can be used to correct for chromatic dispersion [38], the effect described in this section explains how nonideal effects of a solid VIPA limit the VIPA's ability to perform pulse shaping. In other words, the effect of a wavelength dependent VIPA FSR is very different from dispersion introduced by the pulse shaper. This analysis begins with the wavelength dependence of fused silica. The index of refraction of fused silica can be described by the Sellmeir equation [39]

$$n^2(\lambda) = 1 + \frac{0.696750\lambda^2}{\lambda^2 - .069066^2} + \frac{0.408218\lambda^2}{\lambda^2 - 0.115662^2} + \frac{0.890815\lambda^2}{\lambda^2 - 9.900559^2} \qquad (4.36)$$

where n is the index of refraction and λ is the wavelength in microns visualized in Figure 4.21.

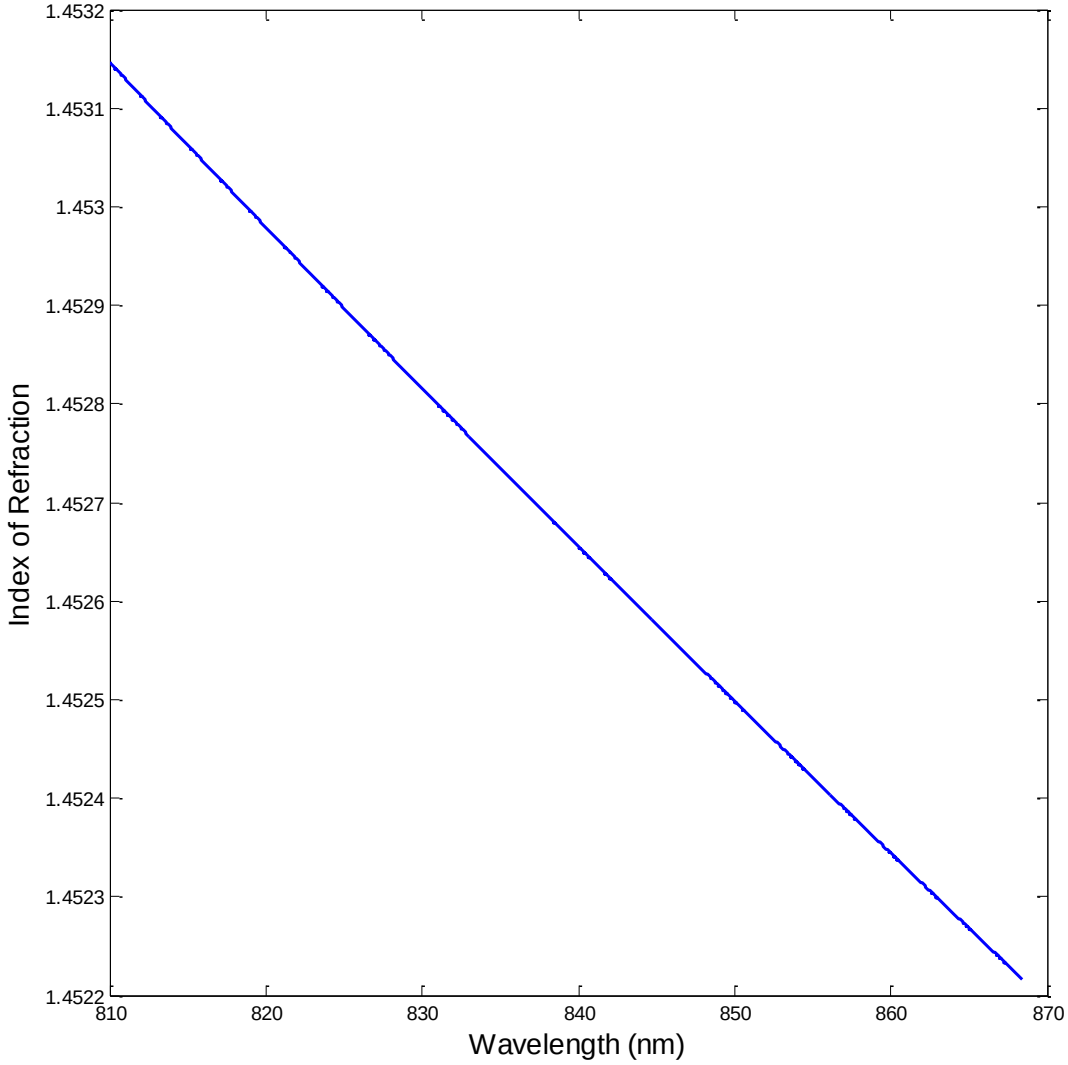


Figure 4.21: Index of refraction of fused silica as a function of wavelength

By plugging in the wavelength dependent index of refraction into equation (4.5) the wavelength dependent FSR is assembled to be

$$FSR(\lambda) = \frac{c}{2\sqrt{1+\frac{0.696750\lambda^2}{\lambda^2-.069066^2}+\frac{0.408218\lambda^2}{\lambda^2-0.115662^2}+\frac{0.890815\lambda^2}{\lambda^2-9.900559^2}}\,t\cos(\theta_i)} \qquad (4.37)$$

Small changes in the VIPA FSR, shown in Figure 4.22, result in a shift in the VIPA output. The details of these calculations can be seen in appendix C.

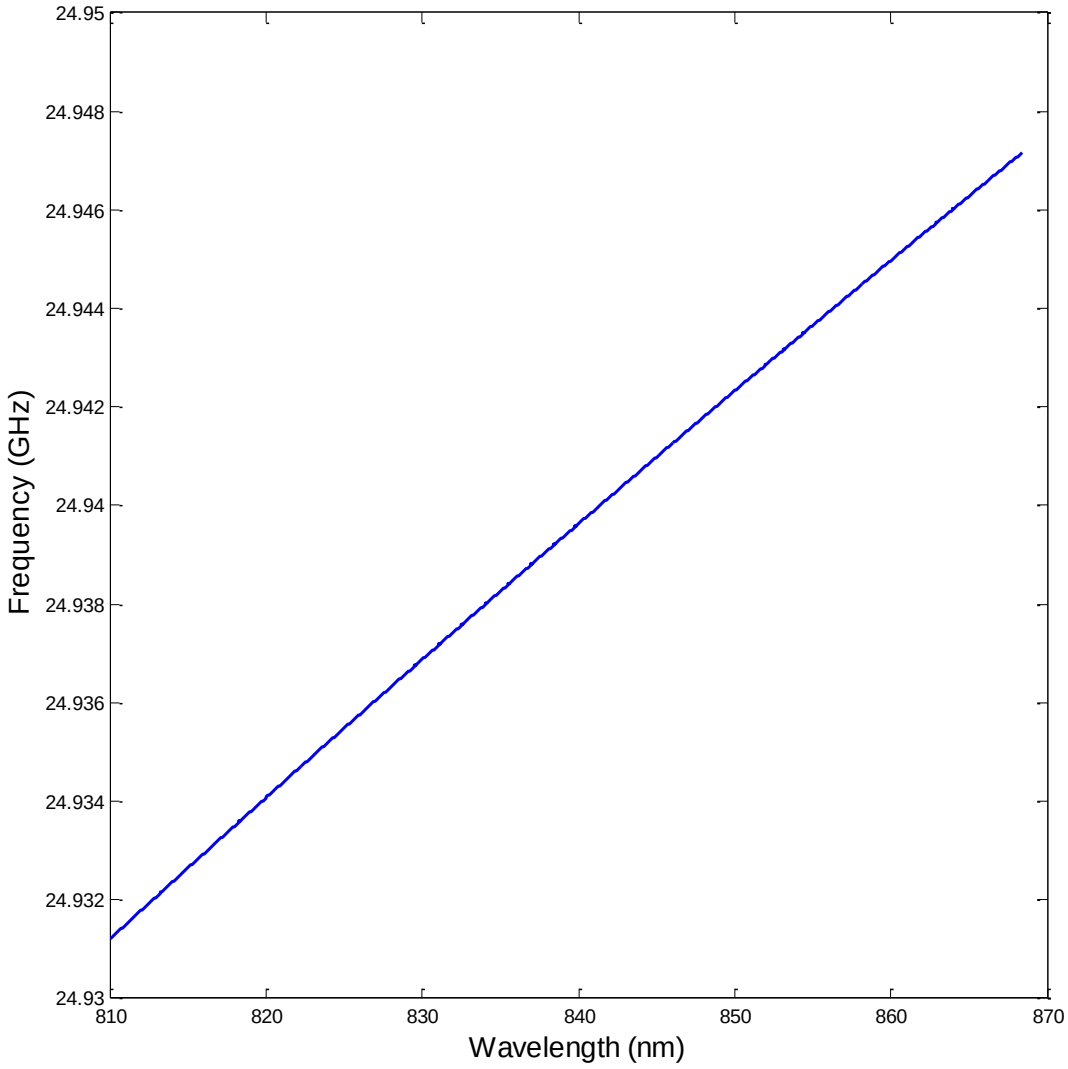


Figure 4.22: VIPA FSR as a function of wavelength

It is important to determine how much change in the VIPA FSR is acceptable. In the 2-D frequency brush setup, the individual modes are resolved in 2 axes so the change in FSR is evident by a bending of the 2-D grid of modes. Instead of regularly spaced modes in the

horizontal and vertical axes, the spacing of vertical modes changes as one scans through the spectrum in the horizontal direction. This effect is very small over the 5.7 nm bandwidth captured by the camera imaged in Figure 4.12, so a cartoon (Figure 4.23) better emphasizes this effect:

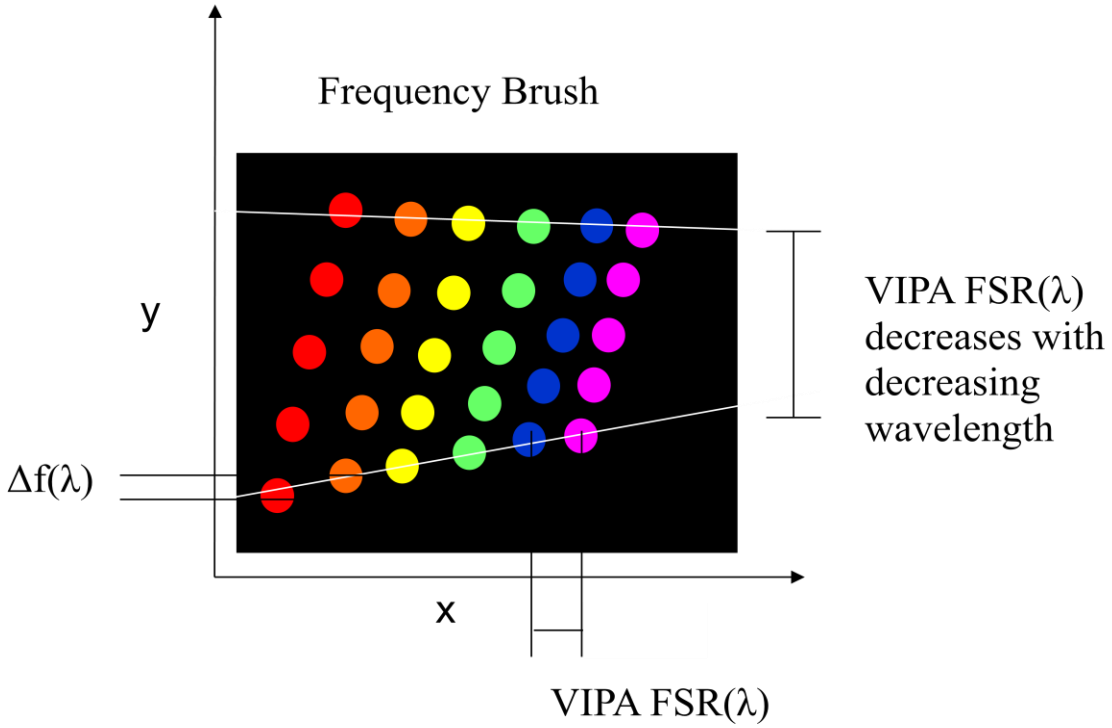


Figure 4.23: Change in mode placement in each VIPA order, $\Delta f(\lambda)$, is a measure in frequency of the skew of the grid.

Recall in previous descriptions of the 2-D brush where the FSR of the VIPA is considered to be constant, the FSR can be calculated from the repetition rate, $f_{rep}$, by equation (4.27). When the number of modes, $N$, is an integer and the FSR of the VIPA is unchanging, repeating VIPA orders are separated in only the $x$ dimension creating the square grid seen in Figure 4.13. This grid becomes skewed when the FSR of the VIPA depends on wavelength as illustrated in Figure 4.23. The difference between where a perfectly horizontally resolved spot would be and where the actual spot is can be thought of as the offset, $o$,

$$o = \frac{FSR(\lambda)}{f_{rep}} - N \tag{4.38}$$

If the offset is equal to 0.5, the horizontal mode (repeated VIPA order) that should be just to the right of the original mode is instead half of the distance to the next vertical mode. This is close to the exaggerated picture in Figure 4.23. If the difference were off by an integer the grid would become square again only with fewer repetition rates in every VIPA FSR. The separation between adjacent modes is the repetition rate of the input laser. Using this calibration, *o* can be used to find the skew value *Δf(λ)*

$$\Delta f(\lambda) = \left( \frac{FSR(\lambda)}{f_{rep}} - N \right) f_{rep} \tag{4.39}$$

*Δf(λ)* is cumulative, every time the VIPA repeats it is shifted by *Δf(λ)*. This means if one compares the location of the second imaged mode (separated horizontally), it will be offset from the first imaged mode by 2* *Δf(λ)*. So to calculate where a spot is imaged, the sum *Δf(λ)* of each VIPA FSR (repeated VIPA order) must be totaled. In a 2-D pulse shaper where one uses a 2-D spatial light modulator (SLM) with a regular square grid of pixels to control the spectral mask it is important to know when this skew results in spots being imaged to improper pixels in the regularly spaced grid. When the total skew or sum of *Δf*, visualized in Figure 4.24, is equal to the repetition rate of the laser, the location of the VIPA mode will vertically shifted by the repetition rate of the laser. Since this is the original location of the mode that should be just above it one uses a regularly spaced grid, modes will be improperly shaped. The mask that should be applied to one mode will be applied to its adjacent mode instead. Obviously, this would have less than desired effects on the resulting shaped output. To control this effect the spectral bandwidth of the input can be reduced.

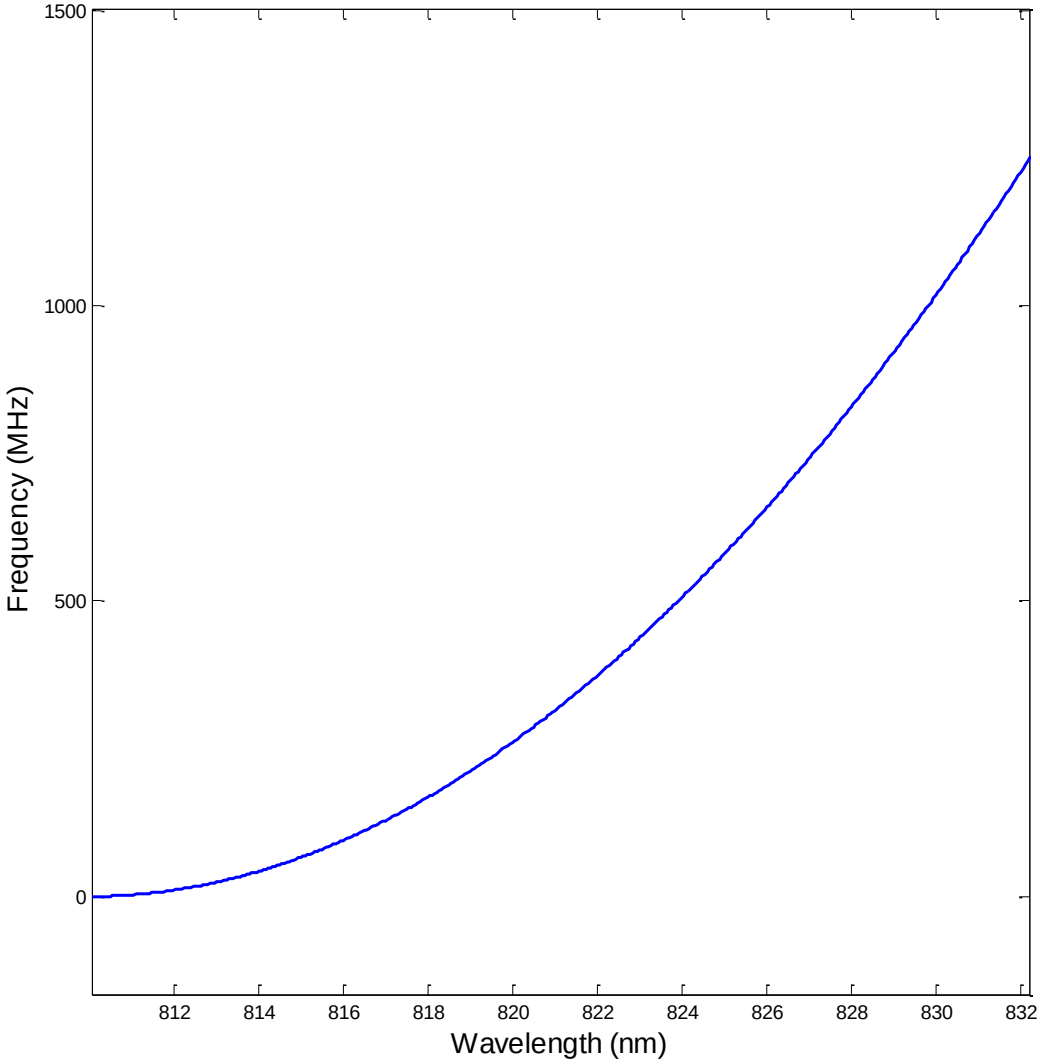


Figure 4.24: Calculated total skew for a 4.14 mm thick fused silica VIPA with 1.01° input angle as a function of wavelength

A reasonable limit to how much total skew is acceptable is when an adjacent mode is imaged a FWHM away from the next location. This is the point where one mode crosses into the expected location of its adjacent mode. This limit is chosen because the rest of the spectrum will still be imaged properly and at this point only a few modes at the wings of the spectrum begin to improperly masked. This occurs when the total skew = $f_{rep}$-FWHM, using numbers from this

experiment 890 - 357 MHz = 533 MHz. To calculate the acceptable bandwidth, find the wavelength that results in this skew using Figure 4.24. 533 MHz corresponds to 824 nm which is 14 nm away from the center wavelength of 810 nm. Since this skew effect is quadratic and symmetric, this is only half the acceptable bandwidth. So the total FWHM of the input spectrum is calculated to be 28 nm.

In the VIPA only pulse shaper where repeating orders of the VIPA overlap one another described in Chapter 5, it is essential that the change in VIPA FSR does not change the position of output modes by enough to cause adjacent mode groups to be mixed together. This is analogous to the 2-D pulse shaper described previously when only a regularly spaced grid can be used. Once adjacent mode groups are mixed together, the line-by-line pulse shaping condition will not be met. So to still achieve line-by-line pulse shaping one can limit the bandwidth of the input pulse, which reduces how much the FSR changes and results in better separation of the mode groups. The more cross-talk there is between adjacent modes the less control there is on how arbitrary of a waveform can be formed. When this location is off as a result of the total skew, see Figure 4.24, by $f_{rep}$ FWHM, too much of adjacent modes will be mixed to the mode above. Again, this results in an acceptable input bandwidth of 28 nm. While this is a reasonable limit to the maximum optical bandwidth for this solid fused silica VIPA, at this limit in the VIPA-only pulse shaper there is no dead space between mode groups in the Fourier plane of the VIPA. This makes it difficult to diagnose pulse shaping issues like how well the mask aligns with the periodicity of the groups of modes. For this reason only 10 nm FWHM of bandwidth is used in the following pulse shaping experiment. This provides separation of the groups of modes necessary for diagnostic purposes. This reduced bandwidth also effectively eliminates (mode

groups are well separated from one another) any nonideal effects from the dispersion of fused silica inside the VIPA.

# Chapter 5

# VIPA-only-based pulse shaping

## 5.1 VIPA-only pulse shaping advantages

Static OAWG requires that each frequency that makes up an input pulse train be independently controlled from one another. However, many useful waveforms can be produced using masks with a repeating spectral pattern. For example, if one would like to produce a pulse train at twice the repetition rate of the original pulse train, every other spectral component of the input pulse train should be masked out. To achieve this output waveform, line-by-line pulse shaping is necessary to separate adjacent lines from one another, only the very simple pattern is repeated over the entire spectrum.

In the case where the desired output waveform is created from a repeating spectral pattern, it is not necessary to separately control each of the thousands of individual comb lines that make up spectrum, rather groups of comb lines can be controlled together. Recall from chapter 4 that another spectrally dispersive device such as a grating is necessary to separate repeated orders of the VIPA. A frequency mode that is separated by exactly one VIPA FSR from another will be emitted at the same angle from the VIPA. This repetitive nature of the VIPA is useful in how it naturally creates groups of modes illustrated in Figure 5.1.

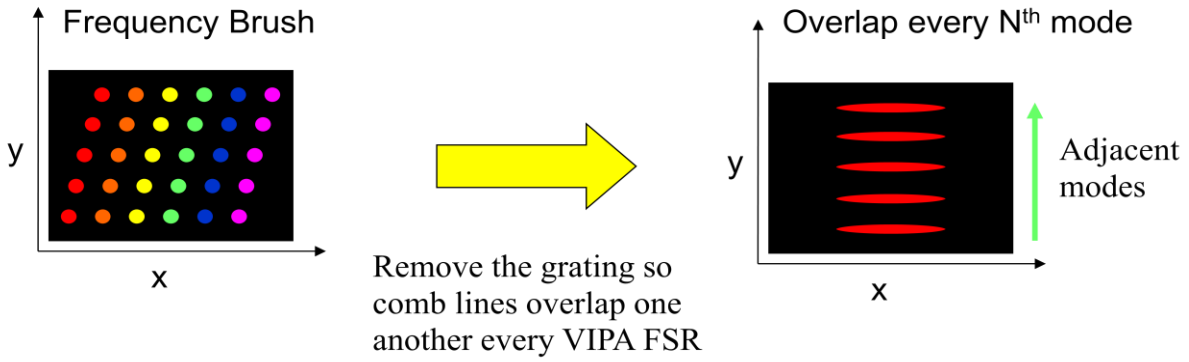


Figure 5.1: 2-D spectral brush being collapsed so that modes spaced by the VIPA FSR overlap one another. Using a spectral mask with this setup creates an output with a repeating spectral pattern every VIPA FSR.

This means using a VIPA-only pulse shaper, any mask that repeats every VIPA FSR over the entire spectrum of the input laser can be applied. Note, that line-by-line pulse shaping is still being achieved since adjacent comb lines are controlled independently from the next. The modes in each group are separated from one another by the VIPA FSR. Figure 5.2 illustrates how adjacent comb lines are in different control groups, meaning they can be modulated independently from each other. This is not the case for non line-by-line pulse shapers.

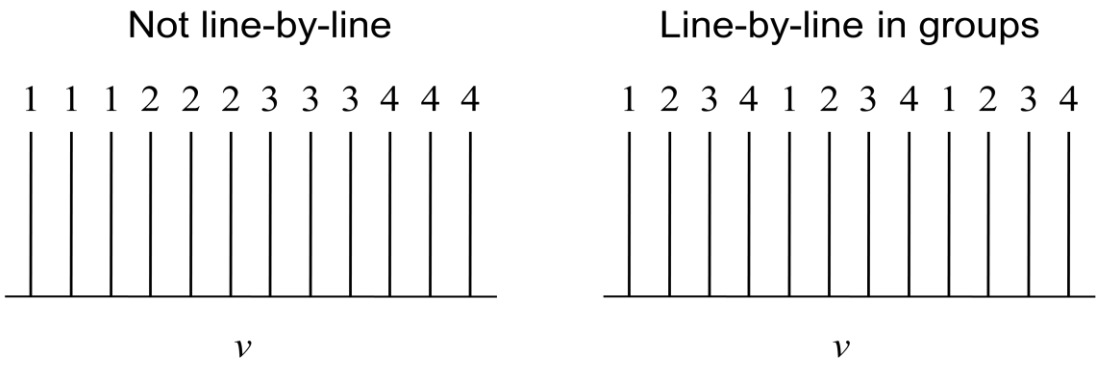


Figure 5.2: Line-by-line pulse shaping in groups is different from non line-by-line pulse shaping. Numbers above comb lines show control groups. Observe how adjacent frequency modes are controlled independently from one another in the line-by-line pulse shaping in groups, while adjacent modes are in the same control group for non line-by-line pulse shaping.

In order for the groups of modes to be well separated from adjacent groups of modes, it is essential that the condition described by equation (4.27) is met. This requirement is met by tuning the repetition rate of the laser to be 1/28th that of the VIPA FSR. This integer number of repetition rates that add up to the FSR of the VIPA is important to so that a square grid pattern shown in Figure 5.1 is produced when using two spectrally dispersive elements to create the 2-D spectral brush. That way when only the VIPA is used, modes that are a VIPA FSR away from one another will overlap in the same location. If the VIPA FSR is not equal to an integer number of repetition rates the skewed 2-D spectral grid shown in Figure 4.13 will collapse into a blob and adjacent groups of modes will not be separated from one another. For this reason, the repetition rate of the laser is tuned to 1/N of the solid VIPA FSR, where N is an integer.

## 5.2 VIPA-only pulse shaping setup

The VIPA-only pulse shaping setup is similar to the 2-D spectral brush setup described in section 4.4 only without the horizontal beam expander or the grating. As explained in the previous section, removing the grating overlaps repeating orders of the VIPA. The groups of modes can be modulated and allow for line-by-line pulse shaping with a spectral mask that repeats every VIPA FSR over the spectrum of the input pulse train.

The setup begins with the 890.4 MHz repetition rate Ti:sapph laser described in section 2.4 . The optical bandwidth of the input to the pulse shaper is reduced 10 nm to eliminate effects from dispersion of the VIPA as described in section 4.7 by passing the output of this laser through an interference filter centered at 808 nm. This reduction in bandwidth is important so that adjacent groups of modes do not mix together due to the dispersion inside the solid fused silica VIPA. The details of this phenomenon as well as the calculations of acceptable bandwidth are expounded upon in section 4.7 . This spectrally filtered laser beam is passed through a

spatial mode filter to pass only a $TEM_{00}$ spatial profile of the beam (Figure 5.3). Since the VIPA-only pulse shaper operates in reflection geometry, the output must be separated from the input. To accomplish this separation, a polarizing beam splitter (PBS) is used in conjunction with a quarter-wave plate with its fast axis rotated 45° from the polarization of light passed by the PBS as illustrated in Figure 5.3. Together these elements separate the retro-reflected output of the pulse shaper from its input.

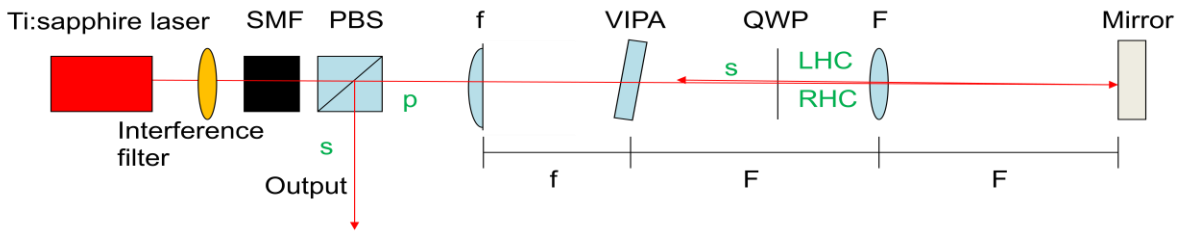


Figure 5.3: Diagram of polarization routing inside the VIPA-only pulse shaper output used to separate the retro-reflected output from the input. Polarization is noted in green, dimensions and devices in black, and the beam path in red. The 890 MHz Ti:sapph laser output is spectrally filtered down to 10 nm FWHM centered at 808nm then a spatial mode filter (SMF) provides a clean mode shape to the polarizing beam splitter (PBS) that reflects the s-polarized pulse shaper output generated from the 45° tilted quarter-wave plate (QWP).

The rest of the pulse shaper setup is very similar to the 2-D brush setup where a 25 cm focal length cylindrical lens is used to create a line focus into the VIPA and a 50 cm focal length spherical lens images the output of the VIPA onto a mirror where a mask may be placed to augment the retro-reflected output as pictured in Figure 5.4.

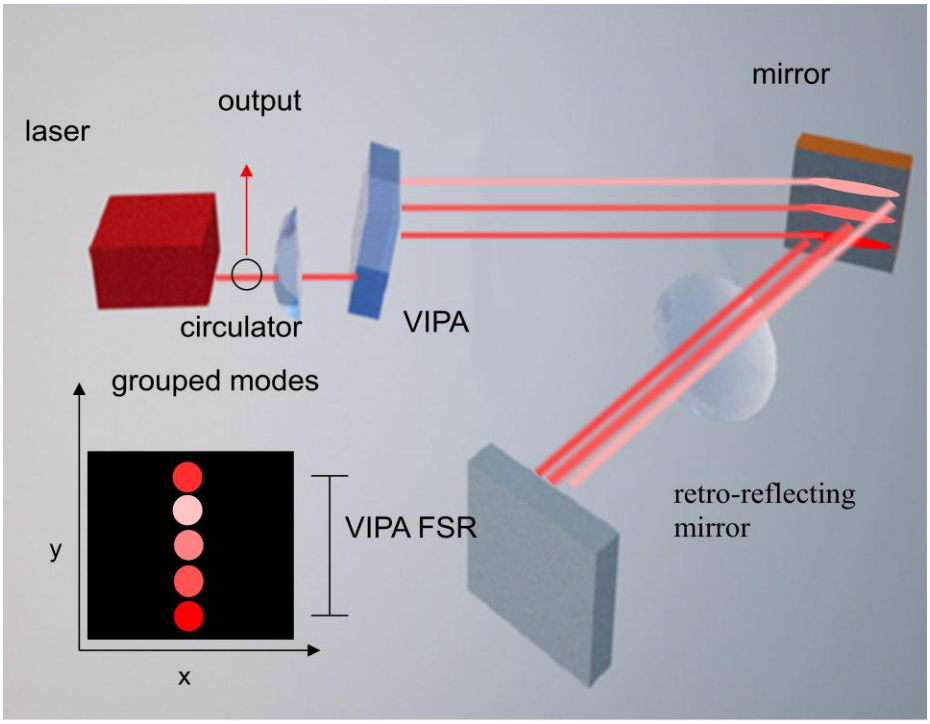


Figure 5.4: The 1-D VIPA-only-based pulse shaper shows how by removing the grating and horizontal beam expander from the 2-D brush setup, Figure 4.11, adjacent frequency modes are resolved into separate groups. These groups of comb lines can then be modified to perform line-by-line pulse shaping with spectral masks that repeat every VIPA FSR.

Several different retro-reflecting mirrors were used in this setup to observe the effects of static line-by-line pulse shaping using the VIPA-only pulse shaper. In addition to a fully reflecting mirror, mirror masks were created to selectively retro-reflect frequency mode groups. These selective mirror masks were created by depositing reflective chrome on an anti-reflection coated window with different patterns to create a desired output. More details on these mirror masks and the results can be seen in section 5.7 .

## 5.3 Solid VIPA temperature sensitivity

As explained in section 4.7 , a small change in the index of refraction or thickness of the VIPA results in a change in its FSR. Temperature changes affect both of these parameters and

therefore change the FSR of the VIPA. Small changes in VIPA FSR result in a vertical shift in the VIPA output location of images a first order effect. The skew effect described in section 4.7 is a result of changing FSR as a function of wavelength a second order effect.

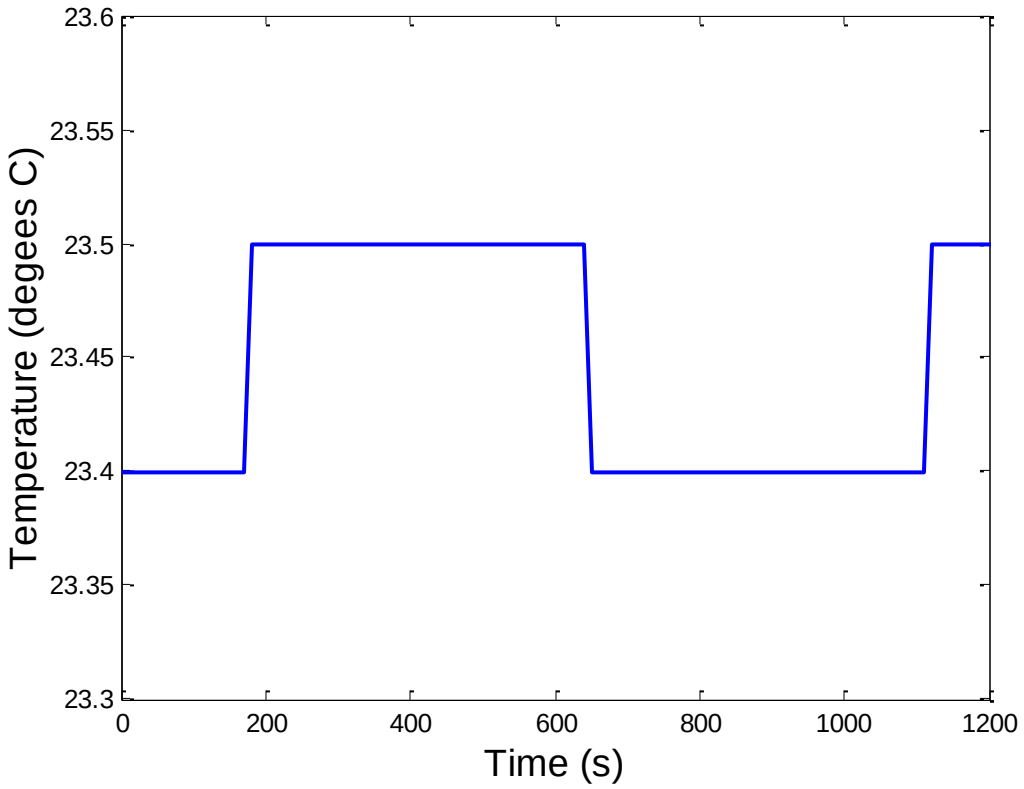


Figure 5.5: Typical air temperature fluctuations in the lab.

The typical change in temperature in the lab is only about 0.1°C every 8 minutes due to air conditioning cycle (Figure 5.5). A small and slow drift in the location of imaged comb lines in the 2-D brush can be corrected for by taking images quickly. However this drift is a serious problem when building a pulse shaper that depends on the location of these images. In this situation, the efficiency of the pulse shaper will drift over time as the location of VIPA modes drift into and out of alignment. This effect was observed in the lab by measuring the power

coupled into a fixed fiber. Drift in the location of the output modes results in a dip in coupling efficiency as measured in Figure 5.6.

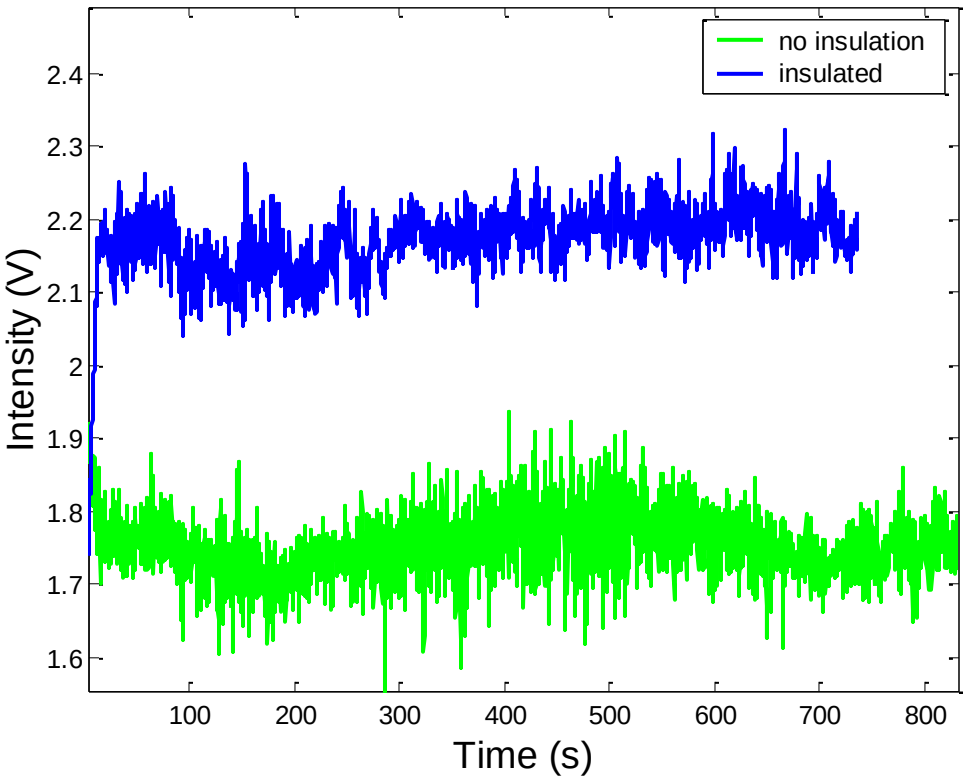


Figure 5.6: Non-insulated (green) and insulated (blue) VIPA output power coupled into stationary SM fiber as a function of time demonstrating changes in VIPA FSR from temperature fluctuations in the lab. The repetition rate of the input laser is stabilized to 890.4 MHz.

The coefficient of thermal expansion for fused silica, $\alpha$=5.5×10$^{-7}$/°C [40], can be used to calculate the thickness of the VIPA as a function of temperature

$$t(T) = t_0 + \alpha t_0 (T - T_0) \tag{5.1}$$

Where T is the temperature of the VIPA, and $t_0$ is the thickness of the VIPA at a temperature $T_0$. The index of refraction of fused silica also changes as a function of temperature

$$n(T) = n_0 + \beta n_0 (T - T_0) \tag{5.2}$$

Where $n_0$ is the index of refraction at $T_0$ and the thermal coefficient of the index of refraction $\beta$=1.26×10$^{-5}$/°C at 800nm [41]. Combining equations (5.1), (5.2) and (4.5) yields the temperature dependent VIPA FSR

$$FSR(T) = \frac{c}{2n(T)t(T)\cos(\theta_i)} = \frac{c}{2\left[n_0 + \beta n_0(T - T_0)\right]\left[t_0 + \alpha t_0(T - T_0)\right]\cos(\theta_i)} \quad (5.3)$$

The change in FSR is dominated by the change in index of refraction. The FSR after a temperature increase of 0.1° can now be calculated to be 24.93116 GHz using values from the experiment: $t_0$ = 4.14×10$^{-3}$ m, $T_0$=23.3°C, $T$=23.4°C and $\theta_i$ = 1.01°. Since this value is so close to the FSR at $T_0$, FSR$_0$= 24.9312 GHz, it makes more sense to look at the change in FSR, ΔFSR = 32.784 kHz. To investigate how this change affects the placement of modes in the VIPA output the change in FSR is converted to change in repetition rate of the laser

$$\Delta f_{rep} = \frac{\Delta FSR}{N} \quad (5.4)$$

where the number of modes in a VIPA FSR, N = 28, which results in $\Delta f_{rep}$ = 1.17 kHz. Although the actual repetition rate of the laser is the same, this shows how the change in FSR affects the location of the modes. The change in frequency and thereby location of the modes can be calculated from $\Delta f_{rep}$. This effective change in $f_{rep}$ is converted into change in optical frequency, $\Delta\upsilon$, by the relation

$$\Delta\nu = \nu \frac{\Delta f_{rep}}{f_{rep}} \quad (5.5)$$

where the optical frequency $\upsilon = c/\lambda$ = 370.37 THz and the repetition rate of the laser $f_{rep}$=890.4 MHz. $\upsilon$ / $f_{rep}$ is the number of repetition rates in the optical frequency so this yields the multiplication factor used in calculating $\Delta\upsilon$ = 487 MHz. Since each mode is separated by 890.4

MHz when the temperature changes by 0.1°C, the output is shifted by approximately half a period.

To relate this to the power measurements made in Figure 5.6 it is important to consider how much of the resolved Gaussian modes is coupled into the fiber as the mode is shifted. The width, *w*, of the resolved modes is calculated from the FWHM by the relation

$$w = \frac{FWHM}{2\sqrt{2\ln(2)}} \approx \frac{FWHM}{2.35482} \tag{5.6}$$

Using the measured FWHM = 357 MHz from the 2-D brush setup, the width $w$ = 151.6 MHz. The power coupled into the fiber from a single mode can be calculated by integrating the Gaussian equation

$$P_1 = \int_{-c}^{c} e^{-\frac{(x)^2}{2w^2}} dx \tag{5.7}$$

where the $c$ is the acceptance frequency bounds of the integral are set by the acceptance angle of the fiber, $x$ is a measure of frequency as it is spread out in space (image of the VIPA) hence why $x$ is used. The lens used to couple into the single mode fiber is one of the lenses in a microlens array used to couple adjacent groups of modes into separate fiber channels as described in detail later in section 7.1 . When imaging frequencies that are too far away from the optical axis of the microlens array the numerical aperture (NA) is too large for the fiber and the light is not coupled into the fiber. The numerical aperture is calculated by

$$NA = n\sin(\theta) \tag{5.8}$$

Where $n$ is the index of refraction of the medium being focused through and $\theta$ is the angle of the focus with respect to the optical axis. The acceptable NA of the SM fiber being used is 0.11 and this setup focuses through air, $n$ = 1, so the focus angle is calculated to be 6.31°. Since the

microlens array is placed a distance, $d$ = 826 μm from the fiber, the radius of accepted light, $r$, is calculated to be

$$r = \tan(\theta)d \tag{5.9}$$

This spatial radius must be converted into an acceptable frequency difference. This is done by noting that each lenslet is spaced by 250 μm and the spacing of the modes is $f_{rep}$ = 890.4 MHz this yields a frequency sensitivity of 3.56 MHz / μm. By multiplying the acceptable radius by the frequency sensitivity the acceptance frequency bound, $c$, is calculated to be 325.5 MHz.

The power from adjacent modes should also be considered. For the centered case this becomes

$$P_c = \int_{-c}^{c} e^{-\frac{(x-f_{rep})^2}{2w^2}} dx + \int_{-c}^{c} e^{-\frac{(x)^2}{2w^2}} dx + \int_{-c}^{c} e^{-\frac{(x+f_{rep})^2}{2w^2}} dx \tag{5.10}$$

The contribution from adjacent modes in the centered case is very small since the modes are well separated from one another. What is more interesting is when this pattern of Gaussian modes is shifted where the mixing of adjacent modes is more substantial and must be taken into account

$$P_s = \int_{-c}^{c} e^{-\frac{(x-f_{rep}-\Delta\nu)^2}{2w^2}} dx + \int_{-c}^{c} e^{-\frac{(x-\Delta\nu)^2}{2w^2}} dx + \int_{-c}^{c} e^{-\frac{(x+f_{rep}-\Delta\nu)^2}{2w^2}} dx \tag{5.11}$$

where $\Delta\upsilon$ is the shift in Guassian modes calculated to be 487 MHz due to temperature fluctuation of the VIPA. By taking the ratio of the shifted Gaussian mode coupled into fiber over the centered Gaussian mode, the loss in coupling efficiency can be calculated.

$$\frac{P_s}{P_c} = \frac{\int_{-c}^{c} e^{-\frac{(x-f_{rep})^2}{2w^2}} dx + \int_{-c}^{c} e^{-\frac{(x)^2}{2w^2}} dx + \int_{-c}^{c} e^{-\frac{(x+f_{rep})^2}{2w^2}} dx}{\int_{-c}^{c} e^{-\frac{(x-f_{rep}-\Delta\nu)^2}{2w^2}} dx + \int_{-c}^{c} e^{-\frac{(x-\Delta\nu)^2}{2w^2}} dx + \int_{-c}^{c} e^{-\frac{(x+f_{rep}-\Delta\nu)^2}{2w^2}} dx} \tag{5.12}$$

Using the values $w$ = 151.6 MHz, $f_{rep}$ = 890.4 MHz, and $\Delta\upsilon$ = 487 MHz the loss in coupling efficiency is calculated to be 0.461. In Figure 5.6 the coupled power drops by 0.10 of the original signal in approximately 8 minutes. This drop in power is less than the calculated drop in power from a temperature fluctuation of 0.1°C. This is likely due to the thermal mass of the VIPA keeping the internal temperature of the VIPA more stable than the air temperature in the lab.

To mitigate the effects of a changing VIPA FSR a box was built to thermally insulate the VIPA from lab temperature fluctuations. The results of this passive temperature stabilization are shown in by the blue line in Figure 5.6. Clearly, the power fluctuation over 8 min lab thermal cycle is reduced to only 5% of peak power as compared to 10% from the non-insulated VIPA. It is estimated from these results that the VIPA now only fluctuates by .01°C.

## 5.4 Detection: cross-correlation setup

To get the sensitivity and high temporal resolution necessary to resolve the output of the VIPA-only line-by-line pulse shaper, a cross-correlator was built. Cross-correlation is a process of signal detection that uses a short pulse as a reference to sample a signal at different times. By using a translation stage to change the delay of the reference pulse, different times of the signal can be measured, see Figure 5.7.

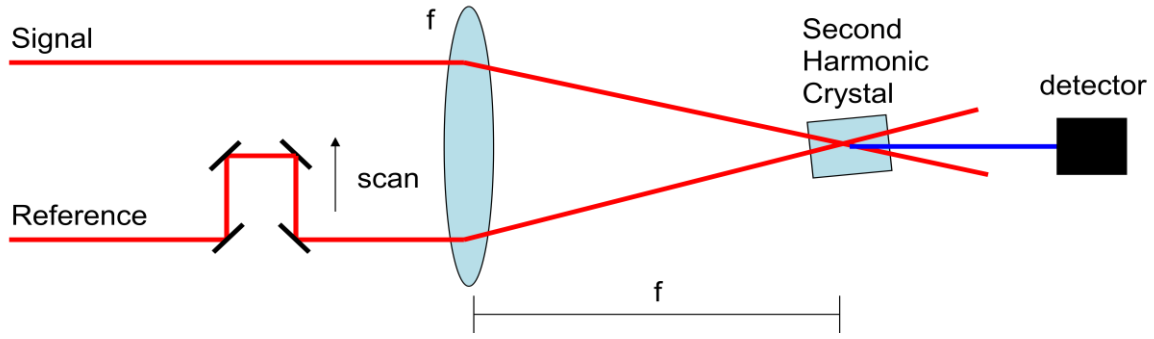


Figure 5.7: Cross-correlation diagram. The SHG signal is generated only when the signal and a short pulse reference is present. By scanning a translation stage in the reference path, the time response of the signal can be measured with high temporal resolution.

In this experiment, the signal being measured is the output of the VIPA-only pulse shaper and the reference is simply the original pulse train from the 890 MHz repetition rate Ti:sapphire laser. Using a 50/50 beam splitter half of the Ti:sapphire laser output is used as a reference and the other half is used as input for the VIPA-only pulse shaper. A long translation stage of over 66 cm is used in the experiment to allow the cross-correlator to scan through more than just one period of the output pulse train. Since pulses are spaced by 33.68 cm for a 890 MHz pulse train, over 4 pulse periods can be scanned through (change in path length = 2X translation stage distance). Note, that in order to only have only one reference pulse over this time window it would be necessary to pulse pick only one out of every four pulses in the reference arm. This was not done since in the static case the output pulse train simply repeats every period. A focusing lens of 10 cm is used to focus the two beams into 5mm thick β-$BaB_2O_4$ (BBO) crystal and is then detected using a photomultiplier tube (PMT) to maximize sensitivity.

Cross-correlation relies on creating a signal only when both signal and reference pulses are present. Although each pulse train individually creates a second harmonic signal that propagates with the beams, only when signal and reference pulses overlap in time is another signal created between the two as illustrated in Figure 5.7. Commonly, a BBO crystal works

well for this due to its large non-linear coefficient and convenient indexes of refraction. The BBO crystal generates a detection signal at twice the frequency of the signal and the reference pulse, but only when the pulses interact with one another inside the crystal (arrive at the same time and are spatially overlapped). BBO makes such an excellent choice for a doubling crystal because the extraordinary index of refraction at 800 nm can be made equal to the ordinary index of refraction at 400 nm (doubled frequency). This means as the reference and signal pulses propagate inside the crystal they continually add to the second harmonic generation (SHG) detection signal. This type I phase matched condition [42]

$$n_{eff}^{2\omega} = n_o^{\omega} \cos(\theta) \tag{5.13}$$

where $n_{eff}$ is the effective extraordinary index of refraction and $n_o$ is the ordinary index of refraction, and $\theta$ is the angle of the incident beams from the optical axis as illustrated in Figure 11.1 in appendix D. The effective index of refraction as a function of $\theta$ is calculated

$$n_{eff}(\theta) = \frac{n_e n_o}{\sqrt{n_o^2 + (n_e^2 - n_o^2)\cos^2(\theta)}} \tag{5.14}$$

where $n_e$ is the extraordinary index of refraction on the optical axis. To visualize how the index of refraction changes as a function of angle see Figure 5.8a.

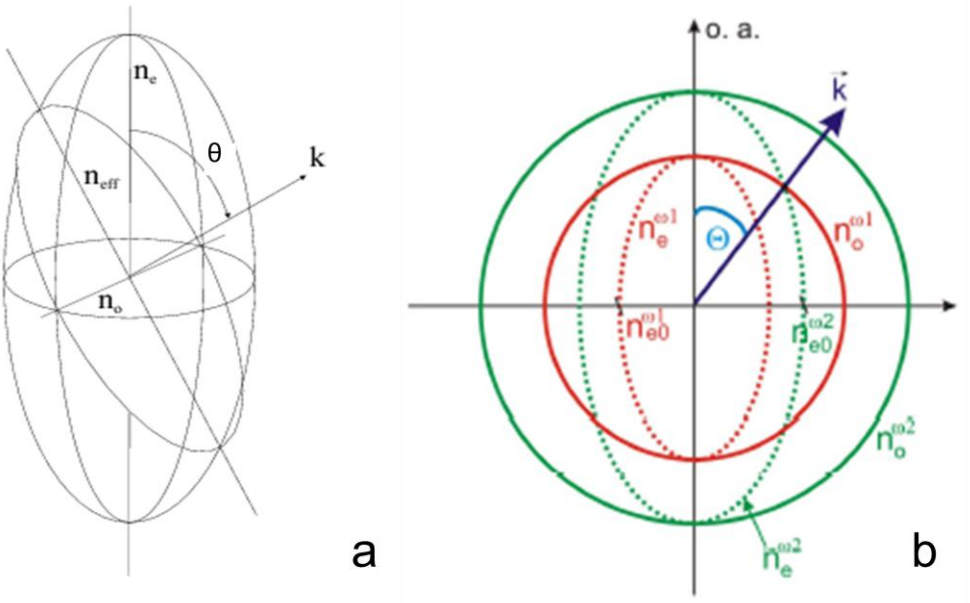


Figure 5.8: Ordinary and Extraordinary index of refraction as a function of angle from the optical axis (a). k-space diagram of ordinary index of refraction at 800 nm ($\omega_1$) and extraordinary index of refraction at 400 nm ($\omega_2$), showing necessary angle from optical axis to achieve collinear type I phase matching (b). Images from [42]

The BBO crystal used in the experiment was cut so that its optical axis is 26.6° from the normal so that it achieves this phase matching condition for 880 nm light at normal incidence. For this experiment we need to double 810 nm light. Using equation (11.2) from appendix D an angle of 28.7° from the optical axis will meet the phase matching condition at 810 nm. This angle is also made clear by the k-space diagram in Figure 5.8b. So that means the crystal must be tilted 2.1° from normal incidence to adjust the optical axis to the angle necessary for colinear type I phase matching. Since the two beams inside the BBO crystal are not collinear, rather offset from the optical axis by 0.1 rad, special care must be taken to calculate the interaction length of the two beams inside the crystal. The phase matching condition is still very close to the collinear case since the angle is so small at .1 rad so the optimum tilt of the BBO crystal is still

2.1°. For more details on interaction length of pulses inside the BBO crystal and its effect on bandwidth see appendix D.

When detecting such a small signal as is the output of the pulse shaper, it is essential that the SHG signal be isolated from any other signals. This is achieved in three different ways. The signal is isolated spatially due to the geometry of the cross correlator the cross-correlation SHG signal propagates directly to the right, not the reference and signal beams as seen in Figure 5.7. After the BBO crystal, an iris is used to block the off axis signal and reference beams and only pass the SHG signal of interest. The signal is isolated spectrally through the use of Schott glass filter placed in front of the detector which absorbs light with a wavelength larger than 500 nm, but passes the SHG light around 400 nm. Finally, through the use of a lock-in amplifier, further noise can be rejected by only measuring the response of the PMT at a specific frequency. The signal beam is modulated using a beam chopper. By using the modulation rate of the signal as a reference for the lock-in amplifier, only signals that correlate to that frequency and phase are measured. This isolation further increases the PMT's sensitivity and allows very weak signals (10 μW) to be detected. Since the reference and signal pulses are so narrow in time, I can achieve very high temporal resolution.

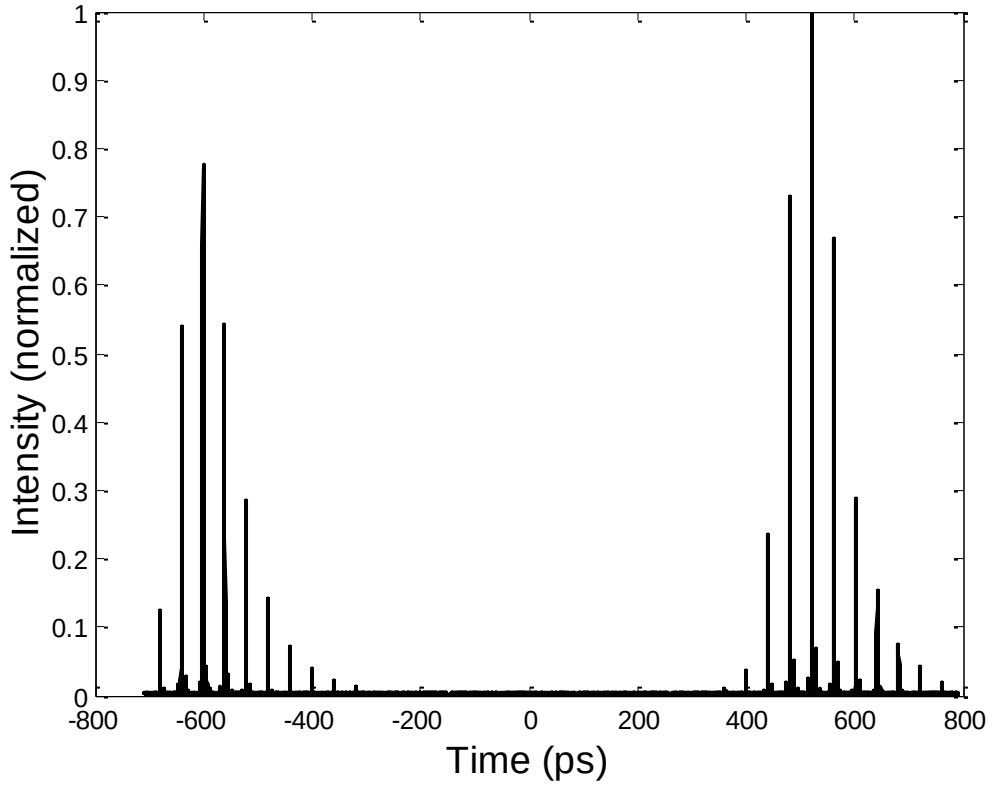


Figure 5.9: Typical cross correlation signal. Observe the high temporal resolution shows the detail of pulse shaper output

The pulses measured in Figure 5.9 show the fine details of the output of the VIPA-only pulse shaper. The high temporal resolution of the cross-correlator, the result of a convolution of the reference pulse and the signal pulse gives a cross correlation FWHM of 600 fs as shown in Figure 5.10.

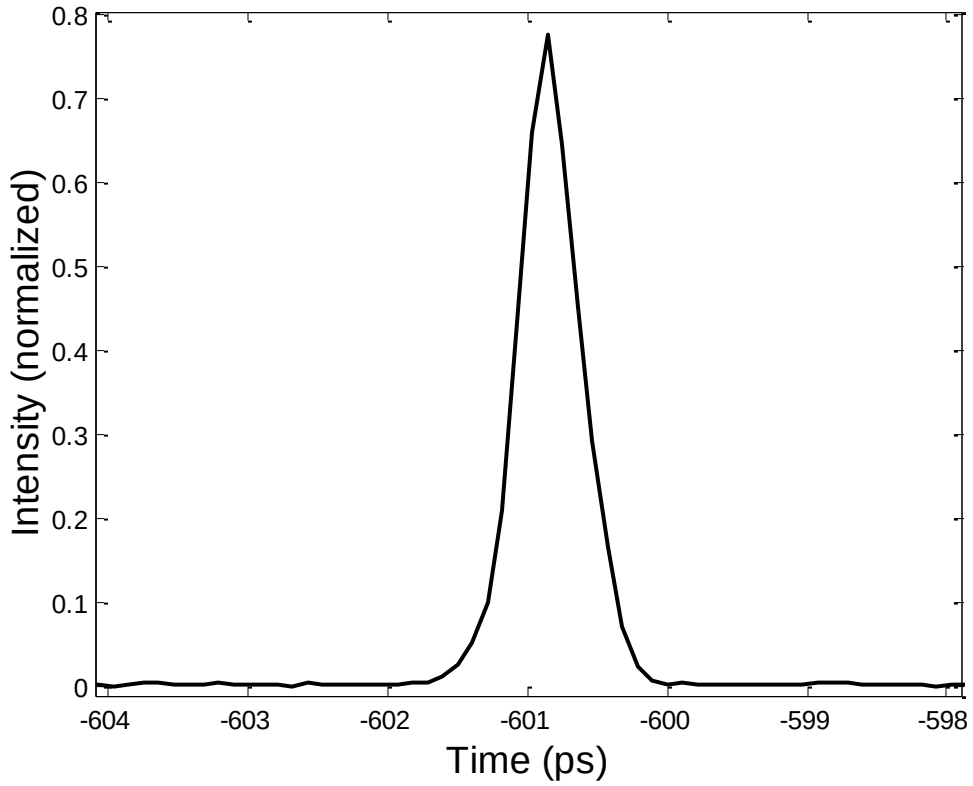


Figure 5.10: Cross-correlation zoomed in view showing high temporal resolution. The width of the narrow pulses shown in Figure 5.9 is shown here to have a FWHM of 600 fs.

## 5.5 Optimization of pulse shaper dispersion

Inside every Fourier pulse shaper there must be some spectrally dispersive element that separates different colors of the spectrum to enable some form of masking to take place which controls the shape of the beam. Simply by having the spectral components of a pulse train separated from one another allows for the possibility of introduced dispersion. Any difference in the path length between the separated colors inside the pulse shaper results in a time delay between different colors, dispersion. This idea is analogous to the use of a prism pair used to introduce anomalous dispersion by first separating out the spectrum and by geometry forcing red light to take a longer path than blue light before reflecting back through the prism pair to

reconstruct the pulse train. Similarly, pulse shapers can be used to correct for dispersion [43]. A line-by-line pulse shaper allows for control of the delay of each individual frequency that makes up the pulse train, allowing for programmable dispersion [44].

In this experiment, there is not any significant source of dispersion that the pulse shaper needs to correct. Rather it is desired that the pulse shaper not introduce dispersion on the pulse train which would have the effect of broadening the width of the narrow pulses. So the goal is to reduce any dispersion introduced by the pulse shaper as much as possible. To achieve this, the geometric details inside the VIPA-only pulse shaper, illustrated in Figure 5.11, must be carefully controlled and optimized to prevent different groups of modes from taking different length paths inside the pulse shaper [45].

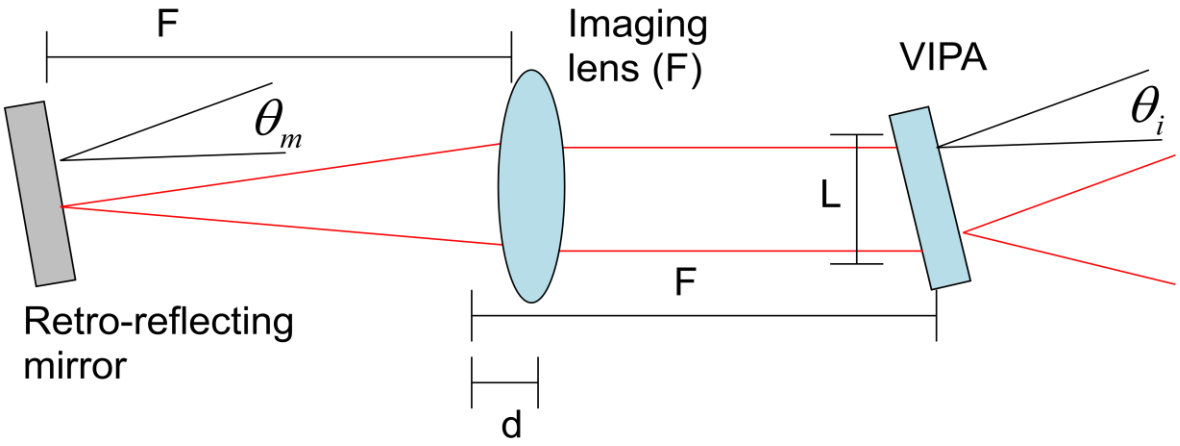


Figure 5.11: VIPA-only pulse shaper dispersion management parameters. Red lines show light focused into the VIPA-only pulse shaper and black lines show dimensions and angles of interest. The input angle of the VIPA, $\theta_i$, focal length of the imaging lens, $F$, angle of the retro reflecting mirror, $\theta_m$, the distance the focusing lens is closer than $F$ to the VIPA, $d$, and the height of the beam after the VIPA, $L$ all need to be carefully controlled to manage dispersion from the VIPA-only pulse shaper.

Inside a VIPA-only pulse shaper the zero dispersion condition is [45]

$$L + \frac{F}{2}\tan 2\theta_m - d\tan\theta_i = 0 \tag{5.15}$$

where the input angle of the VIPA is $\theta_i$, the focal length of the imaging lens is $F$, angle of the retro reflecting mirror is $\theta_m$, the distance the imaging lens is closer than $F$ to the VIPA is $d$, and the height of the beam after the VIPA is $L$. The height of the beam after the VIPA depends on the length of the VIPA as well as the location of the input window and the input angle of the VIPA. In the VIPA-only pulse shaper, this height is measured to be 0.7 cm. The focal length of the imaging lens is chosen to be 50 cm. The input angle of the VIPA is set to 1.2 to get maximum resolution and the retro reflecting mirror angle is set to 0.1 degrees to maximize the output power of the VIPA. $d$ can be adjusted to minimize the dispersion inside the pulse shaper while not having an adverse affect on the pulse shaper resolution or efficiency. Using the measured values from the experiment, the optimum position $d$ is calculated to be 7.5 cm. Experimentally, the smallest dispersion was observed when $d$ = 7 cm which agrees well with the calculated value.

## 5.6 Experimental simulation

Under ideal conditions there is no difference between the 1-D VIPA-based pulse shaper and one that separately resolves the individual comb lines from one another and uses a mask that repeats every VIPA FSR. In either case, dispersion inside the pulse shaper causes oscillations in the output spectrum with a period equal to the VIPA FSR. Although essentially dispersion free operation can be achieved [46], our results suggest some dispersion remained in the current experiments. A simulation illustrates the spectral and temporal effects that dispersion has on the pulse shaper output.

The input to the simulation is an optical frequency comb with a Gaussian envelope. The blue comb in Figure 5.12c shows a 50 GHz section of this input spectrum; since the width of the Gaussian envelope is very broad (1.2 THz) compared to the spacing between comb lines (890 MHz), the comb lines appear to have the same intensity. A figure that captures the full spectrum would show the overall Gaussian envelope, but comb lines would not be resolved. In the 1-D VIPA-based pulse shaper, every 25 GHz section is treated the same. Thus only 50 GHz of the full spectrum is shown for each spectrum in Figure 5.12.

Taking the Fourier transform of this simulated optical comb with constant phase, blue comb and green line illustrated in Figure 5.12c, yields the ideal time domain pulse train shown in Figure 5.12a. As expected, this ideal pulse train is identical to the input pulse train. To simulate how dispersion inside the pulse shaper affects the output pulse train, the input optical comb spectrum is multiplied by a phase mask that repeats every 28 spectral lines, or 25 GHz, as shown by the black curve in Figure 5.12c. The product is then Fourier transformed into the time domain (Figure 5.12b). The effects of this phase mask that repeats every VIPA FSR is consistent with previous work on 1-D VIPA-based pulse shapers where dispersion is present [45]. Due to the geometry of the pulse shaper, different groups of comb lines separated by the VIPA FSR take different paths. This results in a phase shift in the spectrum that repeats every VIPA FSR. The periodic nature of this modulation results in a temporal output that consists of bursts of pulses, as shown in Figure 5.12b. The pulses in each burst are separated by 40 ps, which is the inverse of the VIPA FSR. The peaks of the pulses map out an envelope that corresponds to what the output would be if the spectral width were restricted to one VIPA FSR.

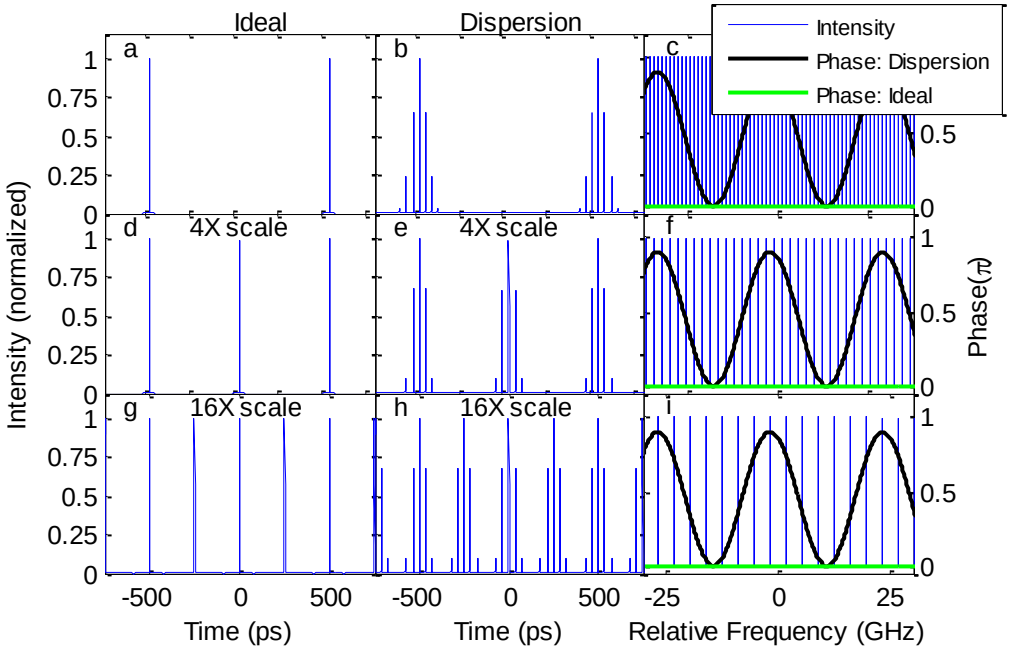


Figure 5.12: Simulation of the temporal (first two columns) and spectral (last column) output of the 1-D VIPA-based pulse shaper under ideal and nonideal conditions for several masks. No mask (a-c), alternating comb mask (d-f), and a mask that blocks 3 out of every 4 comb lines (g-i) are shown. Time zero is chosen to be the time half-way between two pulses of the original pulse train. Under ideal conditions there is no phase modulation of the spectrum (flat phase illustrated in green) and when dispersion is present inside the pulse shaper there is periodic phase in the spectrum (illustrated in black).

Figure 5.12d and Figure 5.12f show the ideal temporal and spectral effects of a mask that blocks every other comb line. As expected, the separation in frequency doubles, which halves the time between pulses in time. Likewise, an ideal mask that blocks 3 out of every 4 comb lines quadruples the separation in frequency and quarters the separation of pulses in time, Figure 5.12i and Figure 5.12g respectively. The time domain response of the output when dispersion is present for the alternating comb mask, Figure 5.12e, is realized by taking the Fourier transform of the spectrum with periodic phase, blue comb and black curve shown in Figure 5.12f. Each output pulse becomes a burst of narrow pulses under a Gaussian envelope similar to what was seen previously with dispersion in the no mask case. Since the mask doubles the comb spacing,

we see half the time between pulse bursts. The time between the narrow pulses that comprise the pulse burst is still inverse the VIPA FSR, 40 ps. Finally, the Fourier transform of Figure 5.12i with the periodic phase represented by the black curve is taken to produce the output pulse train for the mask that blocks 3 out of every 4 comb lines with dispersion, Figure 5.12h. Again we see the characteristic broadening of the pulses due to dispersion.

## 5.7 Static line-by-line pulse shaping

Figure 5.13 shows the intensity cross-correlations for the 1-D VIPA-based pulse shaper described in Figure 5.4. A beam splitter is used to send 50% of the input train of 217 fs pulses (reference) to a delay stage which is then focused into a 5 mm thick BBO crystal along with the output of the pulse shaper to generate a second harmonic cross-correlation signal only when two pulses are present. As described in detail in appendix D, the geometry of the cross-correlator, the length of the overlap region inside the large BBO crystal is only 0.164 mm, corresponding to a phase matching bandwidth of 262 nm, more than enough to capture the full 10 nm FWHM spectrum of the pulse shaper output. By scanning the delay stage of the reference pulse, different time positions can be sampled. The cross-correlation data is then normalized by dividing the data by the peak intensity of the unmasked output.

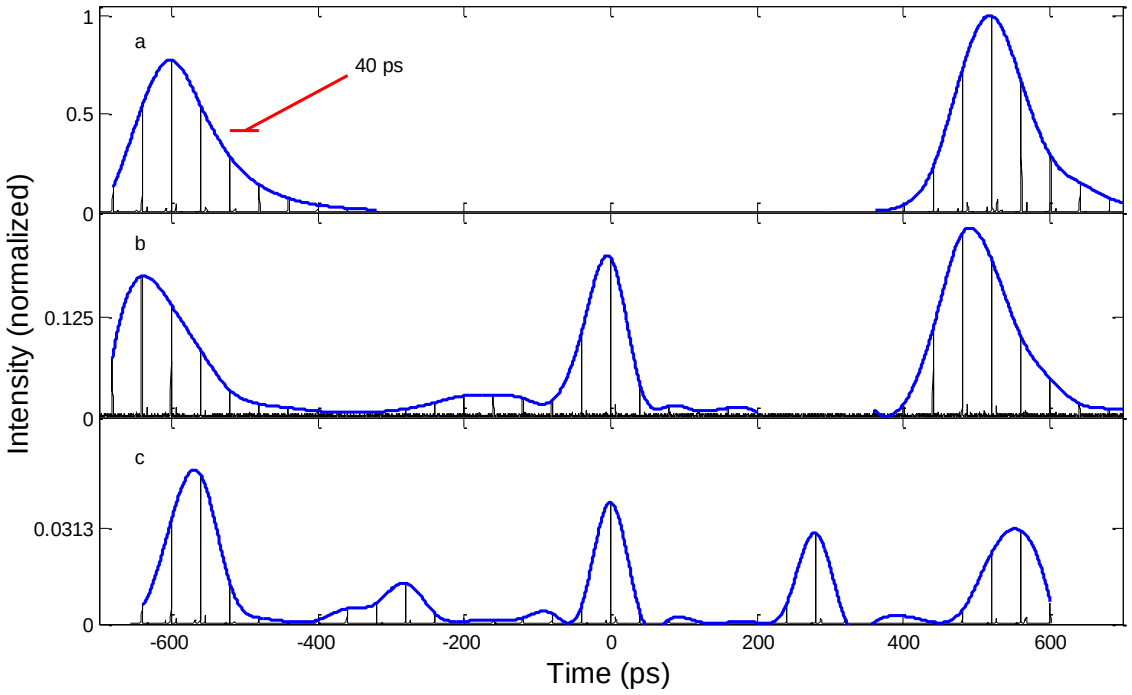


Figure 5.13: Cross-correlation scans of pulse trains shaped by different line-by-line masks. Time zero is chosen to be the time half-way between two pulses of the unmasked pulse train. The first row (a) shows the output of the pulse shaper with no mask in place. An alternating comb line mask is used for the second row trace (b). The last row shows the output of the pulse shaper where 3 out of every 4 comb lines are blocked (c).

The output pulse train with no mask, Figure 5.13a, is not simply a reproduction of the input pulse train. As explained above by the simulation, the broadening of the pulse can be attributed to dispersion inside the pulse shaper. Similar to the simulation results, there is a burst of 600 fs pulses separated by 40 ps, the inverse of the VIPA FSR, under a Gaussian envelope. The smaller sidebands on each of these narrow pulses are the result of reflections in the reference beam. While dispersion inside the pulse shaper can be managed by adjusting the position of the retro-reflecting mask and the imaging lens [45], it is difficult to remove completely.

Figure 5.13b illustrates the effect of a mask that blocks alternating comb lines in the plane of the mirror. The retro-reflecting mirror mask was created using photolithography to deposit an

array of 150 μm wide by 3 cm long chrome rectangles separated by 150 μm onto an anti-reflection-coated piece of glass. This combination reflects every other group of frequencies within a single VIPA FSR. The peak intensity of the Gaussian envelope is close to the expected value of 1/4 the intensity of the no mask case. Figure 5.13b has a double pulse structure as well as discrete broadening of the pulse due to dispersion as was seen previously with the no mask case. The additional structure of the pulses can be attributed to the effect of imperfect mode matching of all 28 modes in the VIPA FSR to the mask. The dispersion law that defines how the VIPA separates adjacent comb lines from one another makes some adjacent comb lines closer together than others [32]. Since this difference in separation is minor, the static mask used in this experiment is a simple linear mask with a constant spatial period. However, spectral lines near the edges of every VIPA FSR are likely attenuated due to this mismatch between the mask and the spectral modes.

Other masks also demonstrate line-by-line pulse shaping. As demonstrated in Figure 5.13c, by blocking 3 out of every 4 comb lines, the expected quadruple pulse output is obtained. As expected, the peak intensity of the Gaussian envelope is approximately 1/16 of the intensity of the no mask case. Again, the effects of dispersion and imperfect mask matching is evident on the output pulse train.

A high resolution spectral disperser with resolution of 357 MHz has been demonstrated and used to resolve individual lines from an optical frequency comb. Line-by-line pulse shaping has been demonstrated for a mode-locked Ti:sapphire laser at 890 MHz repetition rate, the lowest rate for which line-by-line pulse shaping has yet been achieved. Such low repetition rate pulse shaping is an important step toward OAWG as it would potentially allow waveform

updating to be achieved on a pulse-by-pulse basis with modulator arrays with relaxed speed requirements.

# Chapter 6

# Modulator Technology

## 6.1 Modulator overview

A key component to dynamic line-by-line pulse shaping is the type of dynamic mask used to modulate the signal. Commonly, spatial light modulators SLMs are used to control the phase of individual modes as they pass through separate pixels. However, this liquid crystal technology is limited by the milliseconds of time it takes for the liquid crystal molecules to move into position and change the phase, meaning SLM technology can only modulate up to kHz speeds. This results in static OAWG since the mask cannot be changed from pulse to pulse.

Several modulation technologies exist that are capable of the modulation speeds necessary to achieve OAWG in our setup. Using a 890 MHz frequency source, a modulation speed of 445 MHz is required to modulate every other pulse. An ideal modulator would be one that can operate as fast as 445 MHz, but with enough modulation bandwidth to operate down to direct current (DC) so that static-OAWG waveforms can be created in addition to fully OAWG waveforms. In addition to the lofty speed performance, the modulator must also be as efficient as possible. Inside the VIPA-based pulse shaper described in section 5.2 there is only 24 μW of average power in each mode group,. Any attenuation of the signal further increases the high insertion loss of the pulse shaper making detection difficult. Several of the following technologies rely on the confinement afforded by coupling of the signal into fiber to operate at the speed required.

## 6.2 Saturable Bragg Reflector

A pulse shaper operating in reflection geometry, such as in section 5.2 , has a retro-reflecting mirror at the location of the spectral mask. Clearly, the placement of a mirror mask enables control of the reflected spectrum. The idea behind the saturable Bragg reflector is a mirror that can be modulated quickly creating the dynamic mask necessary for OAWG. One cannot simply use a microelectromechanical system (MEMS) device since the time required for micro mirrors to change position is on the order of milliseconds. This means only kHz modulation speeds can be obtained. Instead, a saturable Bragg mirror relies on a control laser to quickly saturate an absorbing medium, such as Gallium Arsenide (GaAs), allowing an incident signal to be retro-reflected as illustrated in Figure 6.1. When the control laser is turned off, the GaAs absorbs the incident signal and no light is reflected. The saturable Bragg reflector was made at NIST by Kevin Silverman.

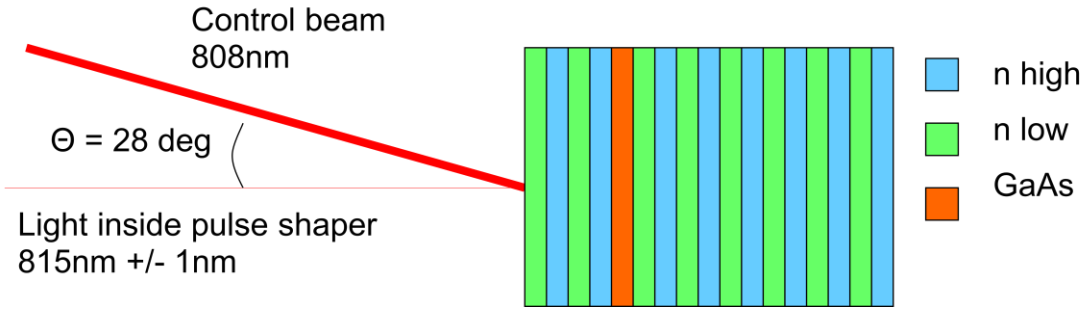


Figure 6.1: Saturable Bragg reflector, showing how a control beam can be used to control the amount of the retro-reflected light inside the pulse shaper.

To investigate how quickly the GaAs layer responds to the control beam, a pump-probe experiment is constructed. Using pulses 66 fs in duration from a mode-locked Ti:sapph laser with a repetition rate of 100 MHz, pump and probe pulse paths are formed and imaged to the same location on the saturable Bragg reflector. By translating a delay stage in the probe path and

measuring the reflected probe light, the temporal response of the saturable Bragg mirror is measured (see Figure 6.2). The control laser to be used in the pulse shaper has a center wavelength of 810 nm. To more accurately test the response of the saturable Bragg reflector under operating conditions, the pulsed pump is spectrally filtered down to 810 +/- 5 nm. Note, that the pump is different from the actual control beam. The pump is a short pulse that only lasts 66 fs as opposed to the CW control beam that is modulated like a square wave. This is important as the modulator needs to be able to hold a state for at least the time between pulses of the input pulse train, 1.1 ns. Meaning that if the CW beam had the same average power as the control beam, it will have approximately $10^5$ times the peak power in the pulse. The details on power needed to saturate the saturable Bragg reflector will be explained later.

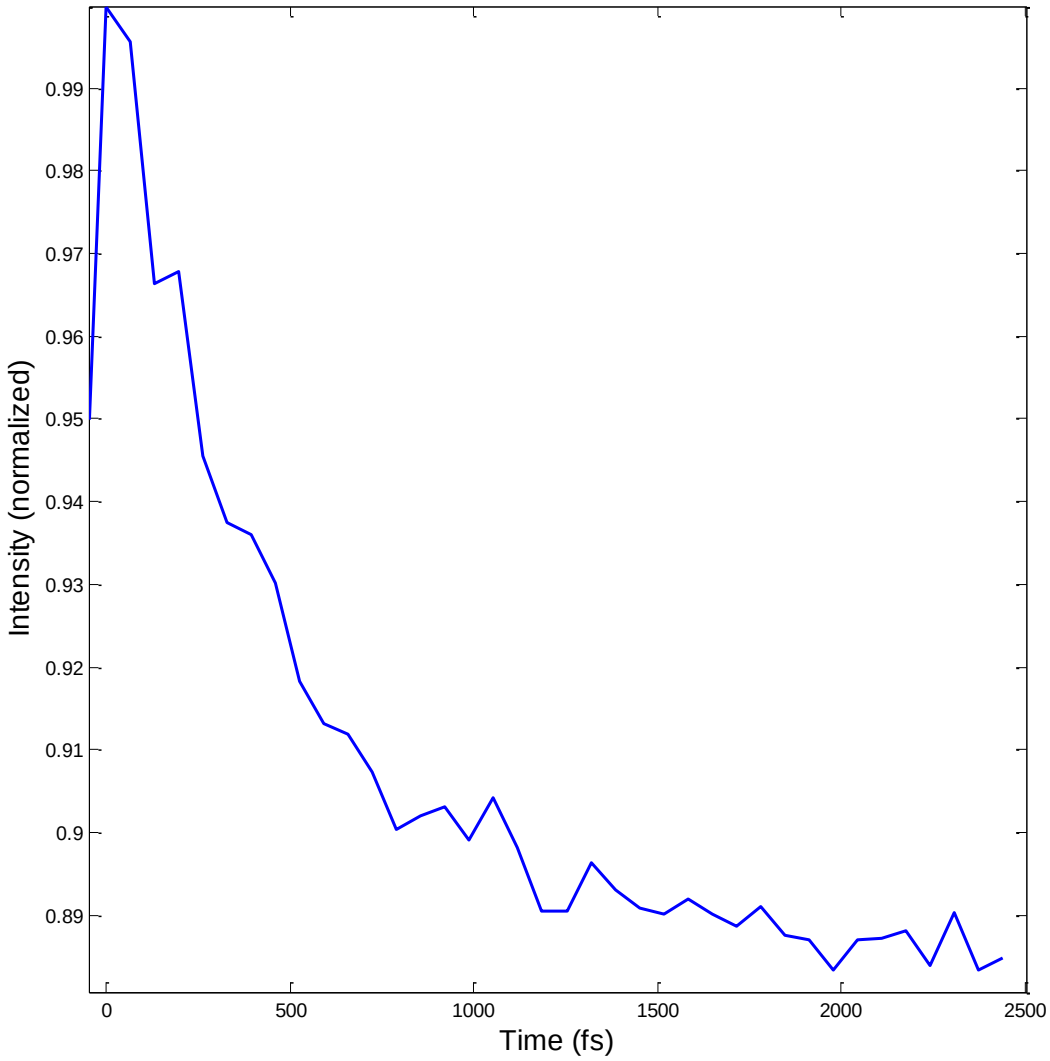


Figure 6.2: Saturable Bragg reflector pump-probe data.

The pump-probe data, in Figure 6.2, show a fast decay constant of 518 fs. This is much faster than the necessary response time of 1 ns to shape each pulse independently from the next at 1 GHz.

Observe how in Figure 6.1 the saturable Bragg reflector has Bragg stack layers both above and below the saturable layer. Having a partial reflector on top of the GaAs allows the control beam to have a greater effect at lower power on the absorption, but at the cost of the spectral bandwidth of the saturable Bragg reflector. The enhancement cavity also helps achieve a good contrast ratio (on vs. off intensity) of the signal incident to the saturable Bragg reflector. This enhancement is important because the high speed CW laser diode that was to be used as a control laser has a maximum output power of 100 mW. When focused to a very small waist diameter of 5.6 μm (core of single mode fiber at 800 nm), this corresponds to a maximum control beam intensity of 400 $kW/m^2$. This CW intensity is much smaller than the peak intensity of a pulse with the same average power. To fully saturate the saturable Bragg reflector, it was found that approximately 200 mW average power from a 100 MHz Ti:sapph laser focused to a 5.6 μm diameter spot is needed. This corresponds to a peak intensity of nearly 81.2 $GW/m^2$. This high intensity is what was used in the pump probe experiment to examine the fast response of the saturable Bragg reflector. In the pulse shaping setup it is important that the saturable Bragg reflector be saturated for 1.1 ns, the entire period of the input pulse train. It is not practical to use a pulsed source to generate the high intensity needed to saturate the saturable Bragg reflector. Further note that if this high of an intensity was not from a pulse but from a CW source, the spot would heat up and thermally damage the saturable Bragg reflector. So for the saturable Bragg reflector to be feasible, the enhancement cavity effect needs to be exaggerated to reduce the intensity of the control beam needed for effective saturation. Increasing the reflectivity of the partial reflector on the top surface of the saturable Bragg reflector would accomplish this; however, it would also further limit the bandwidth of the reflector. The reflectivity of the saturable Bragg reflector at normal incidence can be seen in Figure 6.3. Using the existing

saturable Bragg reflector, the 10 nm optical bandwidth of the pulse shaper would have to be reduced to 2 nm. This limitation to the pulse shaper bandwidth would reduce the available power by a factor of 5. As mentioned at the beginning of section 6.1 it is already difficult to measure the output of the pulse shaper with the full 10 nm of bandwidth. Constructing a new saturable Bragg reflector with an enhancement cavity with a higher quality factor, so that less control power is required would also result in further narrowing this bandwidth.

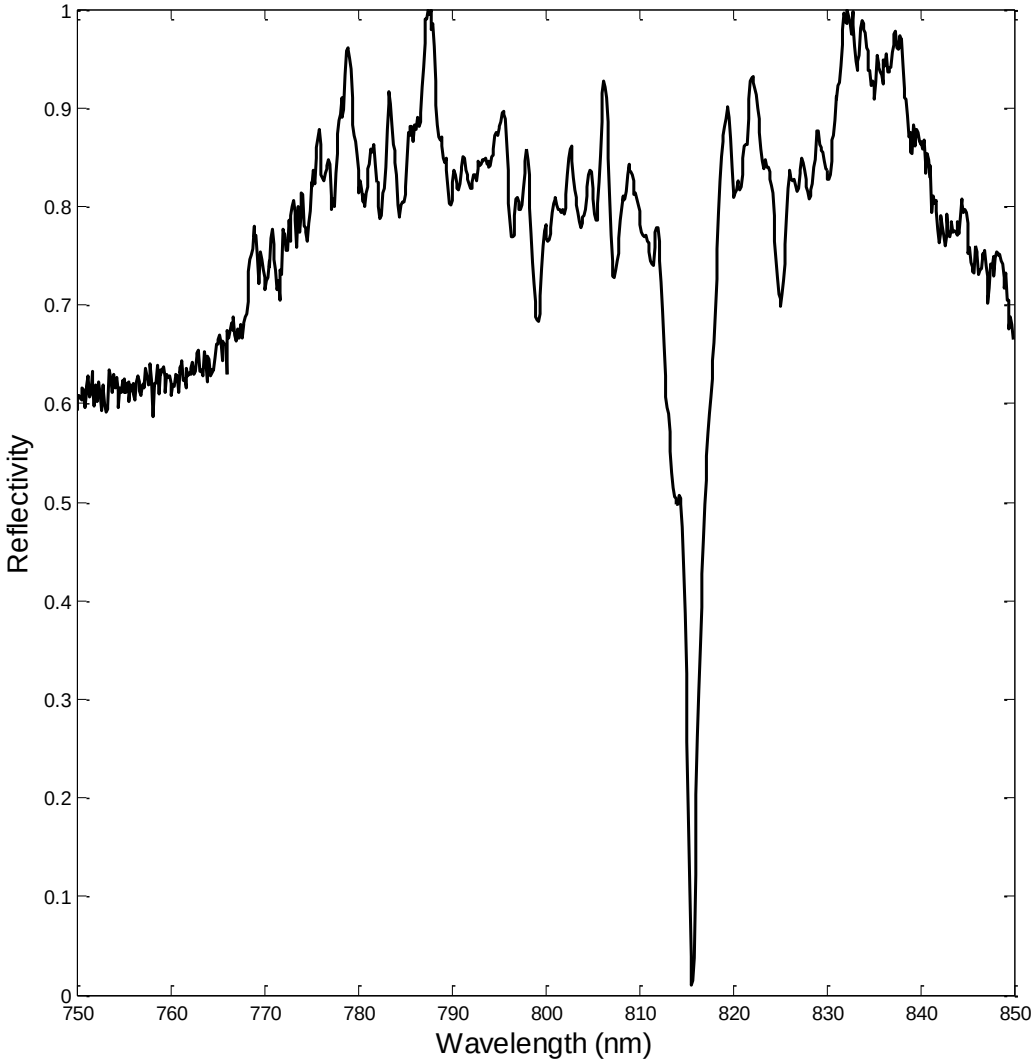


Figure 6.3: Saturable Bragg reflector reflectivity spectrum at normal incidence showing absorbance at 815 +/- 1 nm, 2 nm of bandwidth.

In conclusion, the saturable Bragg reflector will not work as a modulator for a dynamic line-by-line pulse shaper. The existing saturable Bragg reflector requires a control beam of 200 mW from a Ti:sapph laser source to saturate the absorber. This power requirement is significantly greater than the high speed diode laser output power of only 100 mW. While

adding more layers to the Bragg stack above the saturable absorber increases the enhancement effect and reduces the amount of power needed to saturate it, it also further reduces the bandwidth of the saturable Bragg reflector from the already limiting bandwidth of 2 nm.

## 6.3 Vertical cavity surface emitting laser

Another device that can be used as a high speed modulator is a vertical cavity surface emitting laser (VCSEL). These laser diodes typically have a fast response (easily up to 3 GHz modulation) due to the miniature size of around 100 μm. Also, since the laser cavity is grown vertically, many devices can be grown on a single wafer. Instead of using the VCSEL array as a light source, they can be used as a modulator. In place of a mirror in the reflection geometry VIPA-based pulse shaper described in section 5.2 one can place an array of VCSELs. Each group of modes can be imaged onto different VCSELs in the array. The phase of the retro-reflected light from the VCSEL array is sensitive to the voltage applied to the VCSEL is powered to and thanks to the rapid response of the VCSEL it can be modulated very quickly. Previous research [10] successfully uses VCSELs to modulate up to 1 GHz speeds. When the a VCSEL is used as a modulator the phase modulation is limited by only being able to swing from $-\pi/2$ to $\pi/2$ [18]. This limits the full arbitrary nature of the waveforms that can be produced. To be fully arbitrary, one would like to be able to control the phase of each mode from $-\pi$ to $\pi$.

Both VCSELs and the saturable Bragg reflector described in the previous section do not require that the individual groups of modes be coupled into fiber. However, due to the limitations of each of these methods the following technologies are explored which do require coupling groups of modes into fiber.

## 6.4 Gain chip

A gain chip is a laser diode that has an anti-reflection coating on its output facet. This coating effectively eliminates the mirror required to make the laser diode a laser. When the laser diode is turned on it does not lase, rather the gain medium inside the diode laser can now provide amplification for light injected into the laser. The gain chip can then be used as an amplitude modulator through electrical control of the gain. Working with Qphotonics, a laser diode with a center wavelength of 811.5 and a rise time of 0.5 ns was chosen so that the gain chip could be modulated up to the necessary 445 MHz. An anti-reflection coating was applied to the front facet of the laser diode reducing the backward reflection to less than 0.05 %. Finally, since these gain chip diodes are not on a single wafer as in the case of VCSELs, it is necessary to fiber couple them so adjacent groups of modes can be sent to one gain chip separately from another.

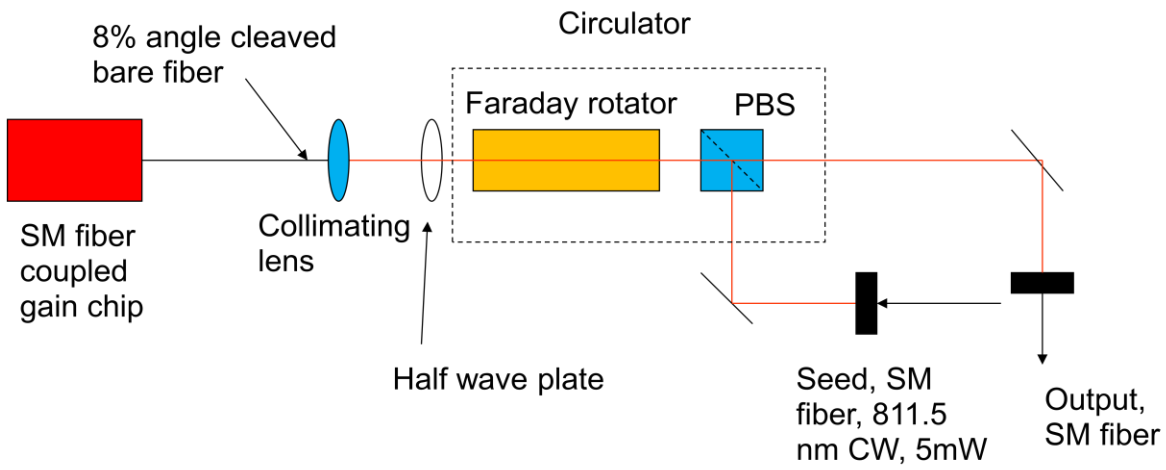


Figure 6.4: Gain chip testing setup.

In testing the gain chip, any backward propagating reflection to the gain chip will cause it to lase. Therefore it is critical that all sources of backward reflection be removed. Since the laser is coupled into SM fiber, the first obvious source of reflection is from the use of any fiber-

optic connector / physical contact (FC/PC) fiber connections. The flat surface from fused silica to air results in a 4% reflection which is more than enough to work as a front mirror for the gain chip and cause it to lase. Of course this reflection is reduced when two fiber surfaces are brought into direct contact with one another; however, back reflection can be reduced even further through the use of angle cleaved fiber. The gain chip fiber was cleaved at an angle of 8% reducing the backward reflection to more than -60 db, while only reducing the power coupled through the fiber by 40% or -2 db. As pictured in Figure 6.4, a free-space circulator is then used to eliminate any further backward reflections explained in section 5.2 . Seed light from a Toptica DL-100 external cavity is tuned to precisely the gain chip center frequency of 811.5 nm and passed into the gain chip. The output spectrum of the gain chip is then monitored using a HP7000 optical spectrum analyzer. At full power the output spectrum of the gain chip can be seen in Figure 6.5. At full power the gain chip ignores the seed and produces the same spectrum with or without a seed input.

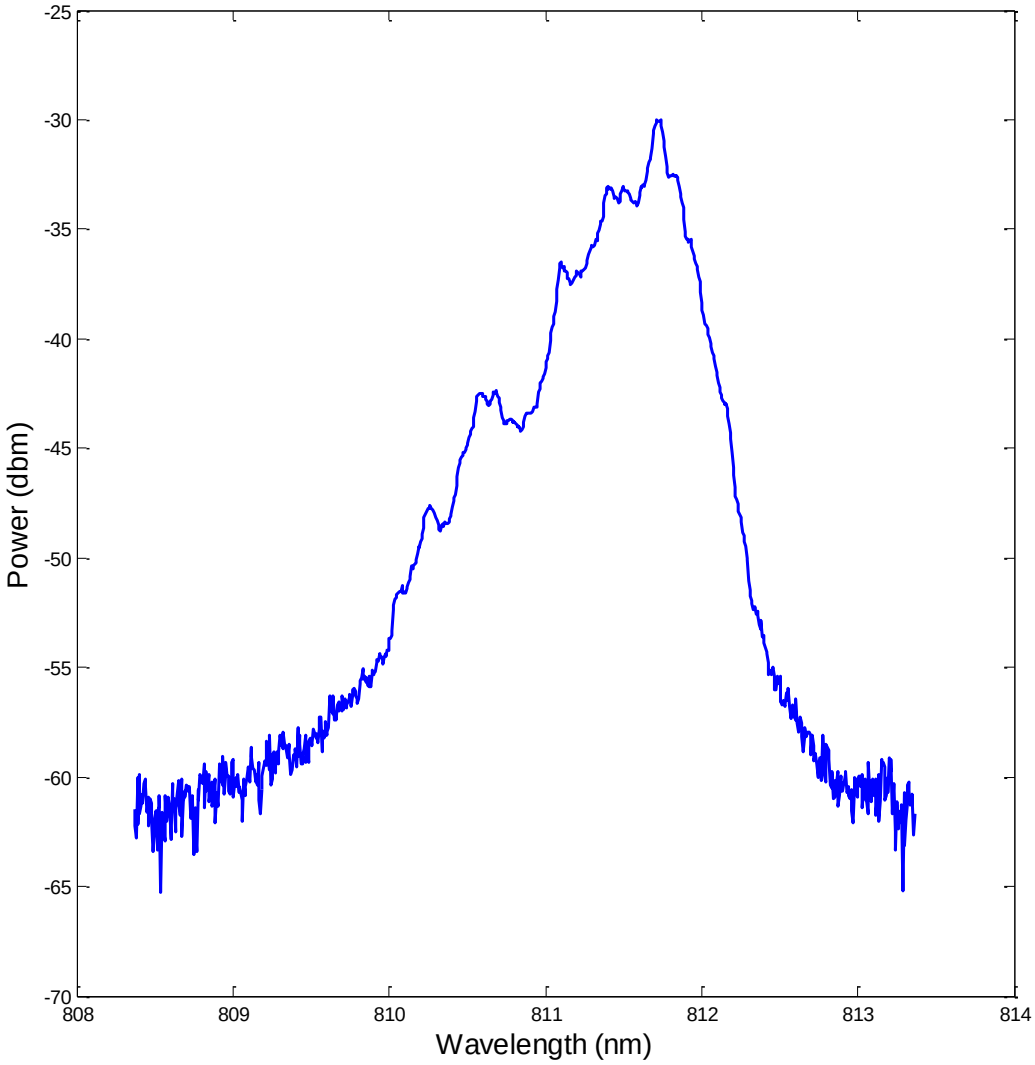


Figure 6.5: Gain chip output with no seed at full power

This lack of sensitivity to the input seed is expected when the gain chip is fully powered. When the gain medium is fully powered (injection current is 43 mA) amplified spontaneous emission (ASE) dominates the output of the gain chip. The ASE depletes the population that would ordinarily amplify the seed light. Typically, this type of gain chip is powered with an injection current around threshold of the laser diode before the anti-reflection coated was added to make it

a gain medium (20 mA). Threshold is also the maximum current the gain chip can be powered to before ASE dominates the output of the gain chip. This way maximum population inversion can be achieved without ASE dominating the output. Figure 6.6 shows the spectrum of the gain chip when powered at threshold without seed light. Notice the peak power at only -55 dbm and the 4 nm bandwidth of the gain chip. The spectrum at threshold shows how the gain chip will not amplify all wavelengths with the same gain; the closer the wavelength is to the center of the spectrum at 811 nm, the more gain it will receive. Also, with the ASE gone, there is a clear ripple in the spectrum with a period of 0.118 nm. This type of interference is typical when some reflection of the gain chip output interferes with itself. A quick calculation of the distance that would cause such a period shows that a double passed spacing of about 2 mm is enough to cause this effect. It is reasonable to picture that there is some spacing of that magnitude between the gain chip itself and the fiber pigtail assembled by Qphotonics. Simply not having the fiber angle cleaved before coupling light out of the gain chip is enough to cause this type of reflection and result in the ripple shown in Figure 6.6.

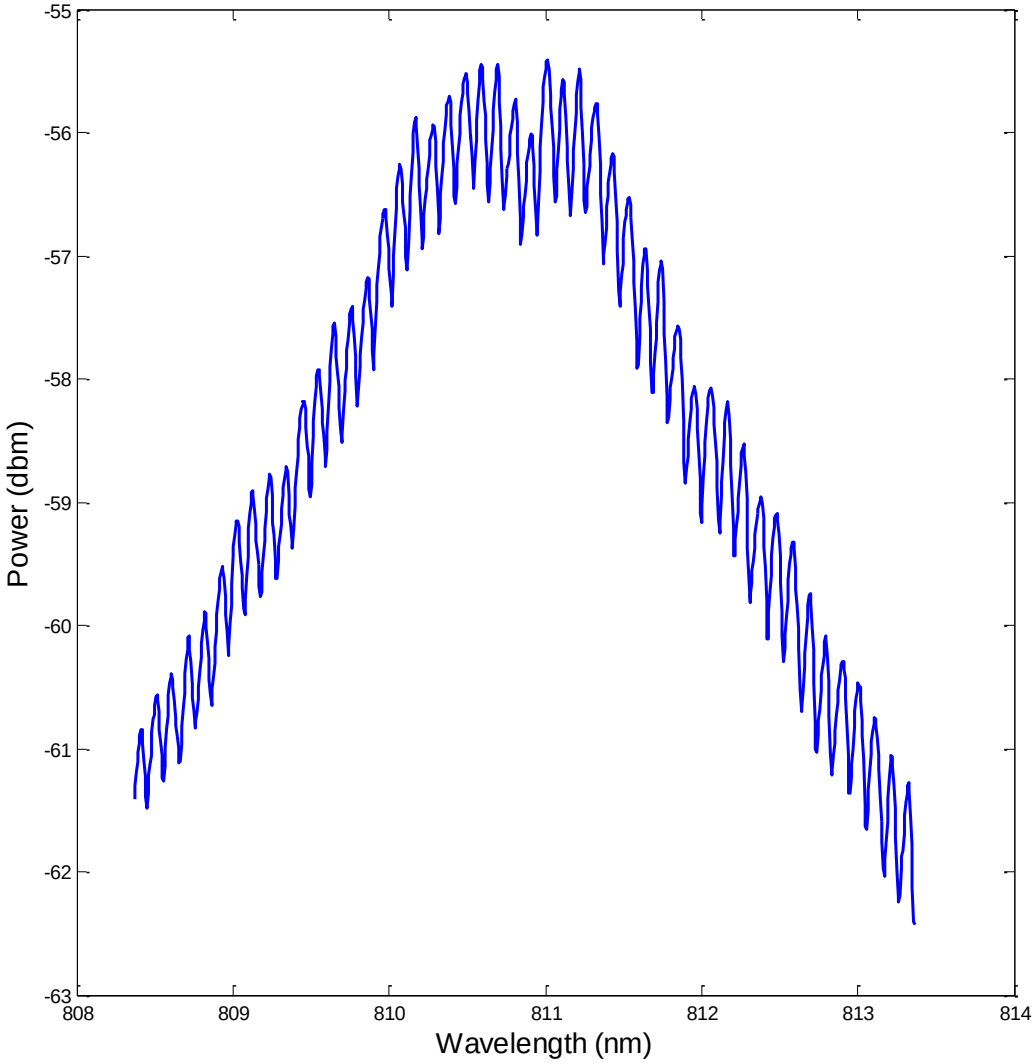


Figure 6.6: Gain chip output with no seed at threshold. The ripple in the spectrum has a period of 0.118 nm

Figure 6.7 shows the response of the gain chip to a 5 mW seed input circulated into the gain chip. Notice here that with the gain chip turned off the seed is absorbed by the gain media of the gain chip, as is expected, reducing the circulated signal to merely -67 dbm. Keep in mind that when measuring the seed directly (mirror in place of gain chip) using the same OSA the

peak power is -18 dbm, with the seed FWHM of 0.3 nm and the resolution bandwidth of the OSA set to 0.1 nm. This is considerably less than the 5 mW fed into the system, but this reading is due to loss in double passing the Faraday rotator (only 90% transmission), any coupling losses in the system, and the OSA measurement. When using the OSA to measure power the peak power measured for a CW signal is typically 7% of the total power when measured using a power meter. This is because the OSA measures optical power as a function of wavelength and the power meter measures the spectrally integrated total power. With the gain chip off, the signal is attenuated by 49 db. This loss can be controlled by powering the gain chip to threshold to get maximum population inversion before ASE dominates the gain chip output. The green line in Figure 6.7 shows the gain chip spectrum when powered at threshold. The seed peak power is now -43 dbm, which is 24 db larger than when the gain chip is turned off. This increase in power still is not enough to provide gain to the seed which was originally -18 dbm. So in conclusion, the gain chip provides the ability to rapidly modulate an incident signal between 49 db of loss to 25 db of loss with 4 nm of optical bandwidth centered at 811 nm. Although this provides the speed necessary for modulating pulse to pulse, the overall loss of 25 db is unacceptable for use in the pulse shaper.

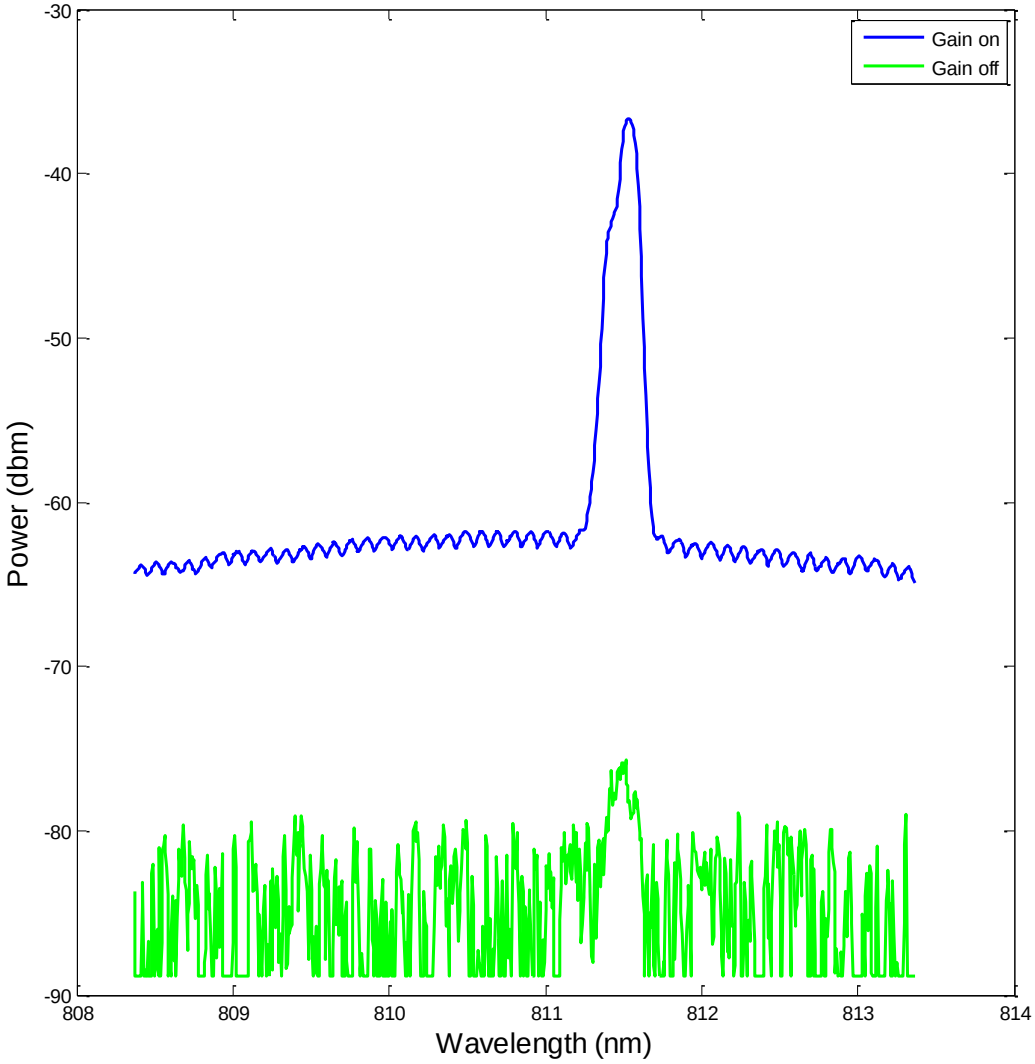


Figure 6.7: Gain chip response to a 5 mW seed. The green line shows the gain chip spectrum when powered at threshold and the blue line shows the retro-reflected seed light from the gain chip when turned off. This shows controllable loss, but not gain of the original seed.

## 6.5 Lithium niobate modulators

Due to the large electro optic coefficient of Lithium niobate ($LiNbO_3$), it is often used in electro-optic modulators. The change in index of refraction of $LiNbO_3$ due to an electric field is very fast, so the speed of $LiNbO_3$ is limited by the size of the device and the electrodes that provide the changing electric field. The smaller the $LiNbO_3$, the lower the voltage that is required to provide the necessary electric field inside the $LiNbO_3$. For this reason, the fastest $LiNbO_3$ modulators (up to 40 GHz) couple light into a $LiNbO_3$ waveguide where electrodes can be placed very close to the waveguide to provide a phase shift of $\pi$ with only around 1 V.

Since this project requires that several modulators be used in very close proximity to one another, it makes sense to create a custom waveguide that allows groups of modes to be individually modulated. The idea is by placing a reflective (mirror the back surface of the waveguide) $LiNbO_3$ waveguide array where a reflective mirror mask would be in the VIPA-only pulse shaper, the individual groups of modes can be phase modulated and reflected back to the VIPA. This means a traveling wave modulator [47] design will not work for this setup, since the signal will propagate in both the forward and backward directions inside the modulator. So a lumped type [47] electrode is the logical choice for electrode type as shown in Figure 6.8.

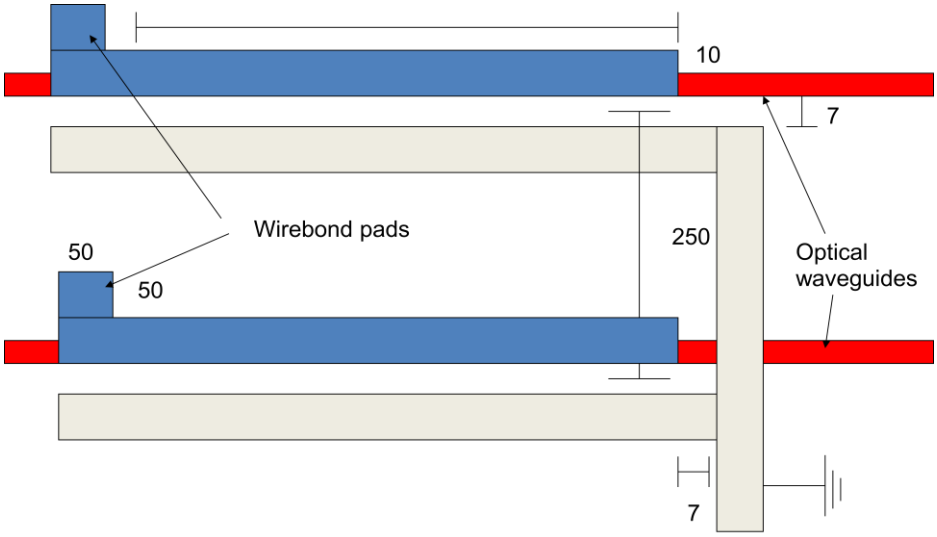


Figure 6.8: $LiNbO_3$ electrode design where all units are all in microns.

The specifics of the electrode design must be chosen carefully to provide enough bandwidth and lowering of the voltage required to create a phase shift of π ($V_\pi$). To calculate modulation bandwidth of the $LiNbO_3$ modulator one must consider how the impedance of the electrodes affects the voltage at the modulator $V_m$ given by [47]

$$V_m = \frac{V_s}{2 + j\omega CR} \tag{6.1}$$

where $V_s$ is the voltage of the source, $C$ is the capacitance of the electrodes, $R$ is the resistance of the electrodes, and $\omega$ is angular frequency of the electrical signal. The bandwidth of the signal, $\Delta f$ can then be calculated by the frequency that reduces $V_m$ by $\sqrt{2}$

$$\Delta f = \frac{1}{\pi RC} = \frac{1}{\pi RC_0 L\varepsilon} \tag{6.2}$$

Where $C$ is the net capacitance of the electrode, which is equal to the capacitive constant $C_0$ times the length, $L$, times the dielectric constant $\varepsilon=n^2$ [47]. Plugging in reasonable values $R$ = 50Ω, $\varepsilon$=28 (value for z-cut $LiNbO_3$), the width of the electrodes is set to 10 μm and the gap

between electrodes 7 μm which gives a capacitance per unit length of electrode 3 pF / cm [47]. This yields a bandwidth of 2 Ghz cm length of electrode. The shorter the electrode, the faster it can be modulated. However this requires $V_\pi$ to be larger, calculated by

$$V_\pi = \frac{\lambda}{2\Delta n L} \tag{6.3}$$

where $\Delta n$ is the change in index of refraction of $LiNbO_3$ given by

$$\Delta n = \frac{r_{33} n_e^2 E_z}{2} \approx 1.5 \cdot 10^{-4} \left( \frac{V}{\mu m} \right) \tag{6.4}$$

when converted into units of volts per micron. The double pass geometry of this waveguide creates an active region of 4 cm while only using a 2 cm long electrode. Allowing lower $V_\pi$ while maintaining high bandwidth. So for an active region of 4 cm and physical length of only 2 cm, $V_\pi$ = 0.6 V (easy to modulate at 500 MHz) and $\Delta f$ =1 GHz (twice the necessary bandwidth).

Other high speed $LiNbO_3$ modulator waveguides have been made by diffusing titanium into the $LiNbO_3$ creating a slightly higher index of refraction region that guides the beam inside the $LiNbO_3$. The process required to diffuse the titanium into the $LiNbO_3$ requires baking the $LiNbO_3$ wafer at 1000° C for 8 hours. When this process was performed on the waveguide array, the extreme heat destroyed the $LiNbO_3$. A temperature gradient from the baking process created internal stresses that were great enough to crack the waveguide. The edges of this cracked waveguide were tested to see how well light could be coupled into each waveguide. In general, the oblong spatial mode shape of light in a $LiNbO_3$ waveguide typically causes around 3 db of loss when coupling from a $TEM_{00}$ mode as in the pulse shaper. However, in testing the waveguide it was found to have around 7 db of coupling loss. The depth of the titanium doped waveguide depends on the length of time and temperature to which it is baked. The depth of the waveguide array was more shallow at only 4 μm deep as compared to the ideal 7 μm. Even if the

waveguide array had not been destroyed, this coupling loss is unacceptable for pulse shaping where the high loss of double passing the VIPA already introduces 15.2 db typically. Further losses from coupling into and out of modulators would cause the insertion loss to be too great to measure the pulse shaper output. Since the loss of the commercial $LiNbO_3$ modulators can be guaranteed to be less than 2 db (each pass), commercial fiber units were purchased to be used in place of the waveguide array.

# Chapter 7

# Coupling adjacent modes into fiber

The confinement of the signal beam when it is coupled into fiber makes it possible for several modulation technologies discussed in chapter 6 to impart a phase and / or amplitude modulation to the signal. Specifically, the commercial fiber coupled phase modulators and the gain chip modulation techniques require single mode confinement of the individual groups of modes.

## 7.1 Optical system design

Separating adjacent mode groups only 890 MHz from one another and coupling into fiber is no simple task. Careful consideration of the separation of the mode groups as well as the mode shape of the beams needs to be taken into account for efficient coupling. First, Figure 7.1 shows the spatial size and separation of groups of modes when imaging the VIPA using a 50 cm focal length lens as was done in chapter 5. Due to the resolution of the VIPA (357 MHz) and how close adjacent modes are in frequency (890 MHz), the width of each group (88 μm) of modes is roughly equal to half the separation distance (175 μm) between modes. Clearly, if this mode shape profile is scaled down to 5.6 μm to couple into SM fiber, adjacent modes will be only 11.2 μm away from one another. Given that the cladding diameter of SM fiber is 125 μm, it is not easy to put the cores of the fibers close enough together.

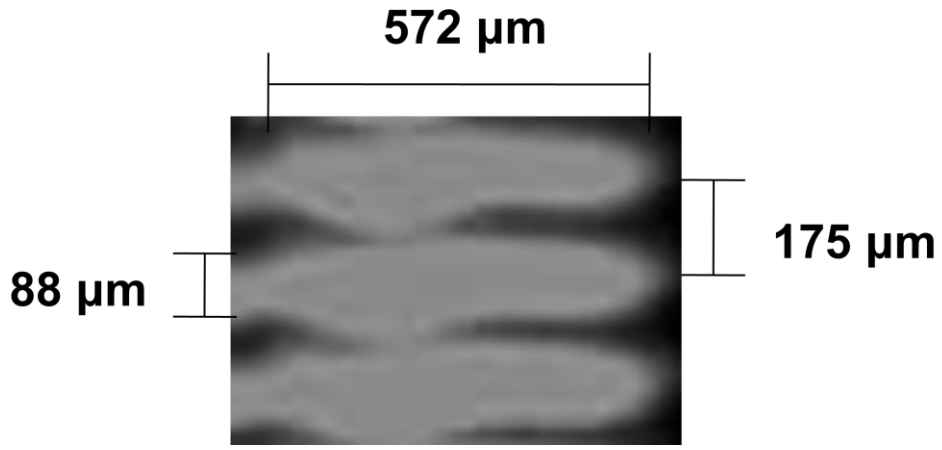


Figure 7.1: Mirror mask plane of the VIPA-only-based pulse shaper using a 50 cm focal length lens.

Even if a custom multi-core fiber were made to have 11.2 µm core separation to suit our needs, there would be issues with coupling of one mode into another mode. Reducing the distance between cores of the two fibers and controlling the length of fiber the cores interact over, one can mix one fiber signal into another. A 11.2 µm core separation is very close and will certainly mix the two signals. In order to achieve line-by-line pulse shaping, adjacent modes must be separated from one another and modulated separately. The VIPA image cannot simply be scaled down to be imaged into fiber, but individual modes need to be focused separately. The necessary separation is accomplished using a microlens array.

The design for the optical system necessary to couple adjacent groups of modes into separate fibers begins with a fiber array. The 8 channel custom fiber array is made out of Quartz by Senko Advanced Components Inc. with a 250 µm pitch. To image individual modes into separate fiber channels, an anti-reflection coated microlens array with 250 µm pitch and NA of 0.18 corresponding to a focal length of 684 µm made by Suss Microoptics is used. It is necessary to separate adjacent modes from one another by the 250 µm pitch so individual

microlenses in the array are able to separate adjacent mode groups into different fiber channels shown in Figure 7.2. The separation of the modes is achieved using a 75 cm focal length imaging lens. The greater focal length not only increases the separation of the modes but as expected increases their width.

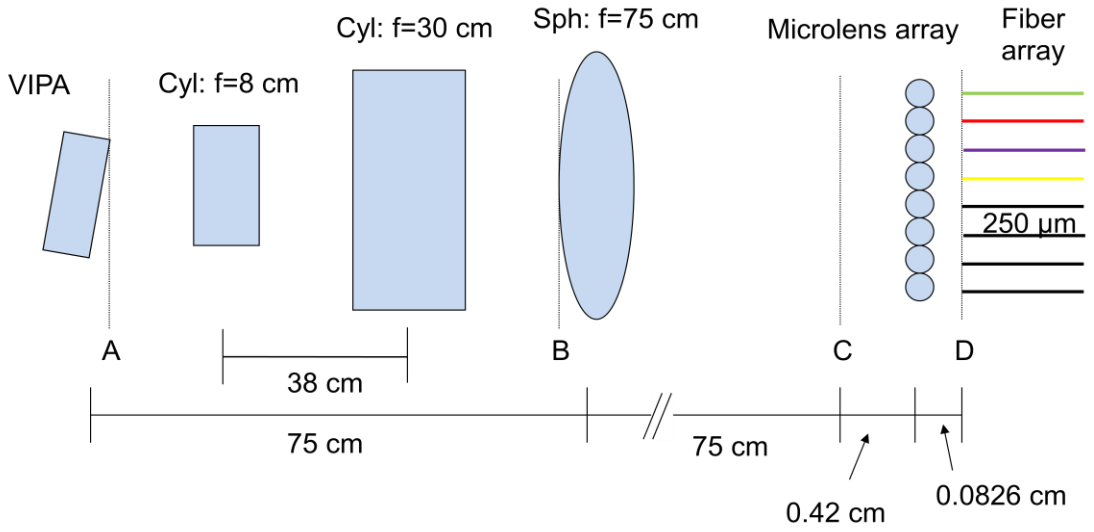


Figure 7.2: Optical layout separating adjacent groups of modes into separate SM fiber. Letters denote locations where the mode shape is measured see Figure 7.3.

If the imaging lens is used without the horizontal beam expansion, shown in Figure 7.3, the result is a scaled up mode shape shown in Figure 7.1. The *x-y* asymmetric Gaussian (oval shape) beam profile as shown in Figure 7.1 would suffer considerable loss when coupled into the x-y symmetric beam profile of the fiber. To correct for this, the asymmetry of the beam profile before the imaging lens is fixed by expanding the beam in *x* to match the spread of the beam in y (due to the VIPA). Two cylindrical lenses separated by the sum of their focal lengths accomplish this task (8 cm + 30 cm = 38 cm separation) providing a magnification in the horizontal direction of 30/8 = 3.7 times. This expands the beam from 10 mm to 37 mm in *x*, roughly correcting for the difference in mode shape at the imaging lens as pictured in Figure 7.3.

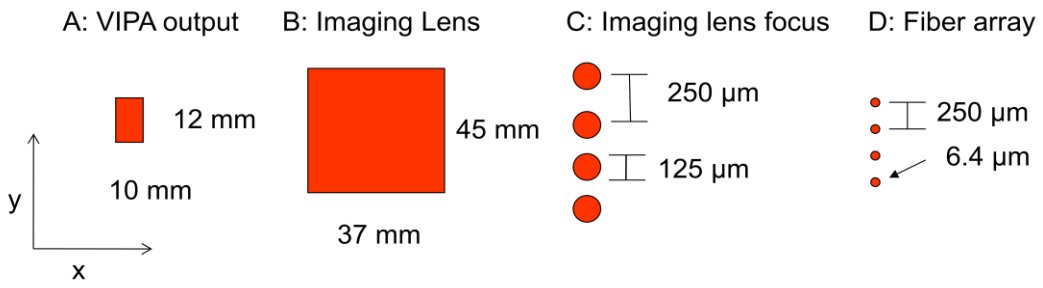


Figure 7.3: Mode shape profiles at various locations in the optical layout separating adjacent groups of modes in Figure 7.2.

The physical dimensions of the optical layout are calculated using the thin lens approximation for the lenses and the standard imaging equation. The output from the VIPA comes to a focus 75 cm after the imaging lens, at this location the groups of modes are separated by the necessary 250 μm with a width of approximately 125 μm as illustrated by C in Figure 7.3. The roughly *x*-*y* symmetric modes now need to be imaged down to a spot size of the SM fiber core of 5.6 μm, but maintain the separation of 250 μm. The microlens array with a focal length of 694 μm is placed a distance 0.42 cm away from the imaging lens focus creating an image of the groups of modes at the fiber array a distance 0.0826 cm after the microlens array. The diameter of the formed image at the fiber array is approximately 6.4 μm in diameter with a NA of 0.15 (reasonable NA for SM fiber input). Also, note that the location of the microlens array from the imaging lens focus of 0.42 cm is as far away as the micro lens can be such that the width of each mode does not surpass the 250 μm separation of the modes. If the microlens were placed any further away, some of the power of adjacent groups of modes would be mixed into adjacent channels.

## 7.2 Coupling efficiency results

When measuring the amount of power coupled into a channel of the fiber array it is important to note that the location of the modes on the fiber array is very sensitive to the repetition rate of the mode-locked Ti:sapph laser. This is an expected result given that the frequency of a given comb line depends so heavily on the repetition rate of the laser given by equation (2.6). Figure 7.4 shows a plot of the power coupled into a single channel of the fiber array while the repetition rate of the laser is increased by about 7 kHz by steadily decreasing the size of the laser cavity. The power coupled into the fiber oscillates with a period of 2150 Hz because changing $f_{rep}$ by that amount will change the frequency of the $n^{th}$ mode by the $f_{rep}$ resulting in imaging the next group of modes into the fiber channel.

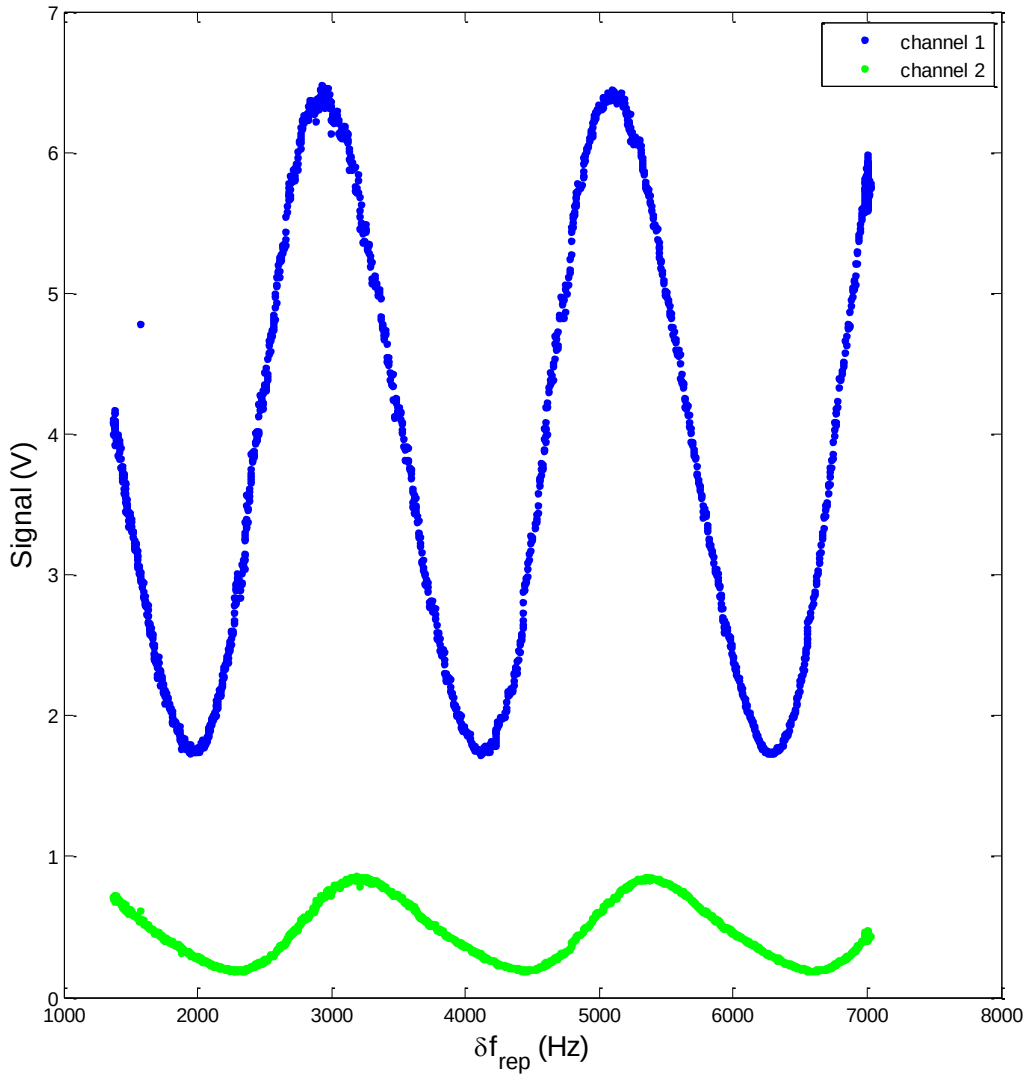


Figure 7.4: Power coupled into fiber array channels: 1 in blue and 4 in green as a function of change in the repetition rate, $\Delta f_{rep}$.

The sensitivity of the location of modes to $f_{rep}$ is used to fine tune the periodicity of the modes to match the periodicity of the lenslet array so maximum power is obtained for four channels of the fiber array simultaneously. By changing $f_{rep}$ and monitoring the power in channels simultaneously it is clear that only when all the channels are at a maximum for the

same $f_{rep}$ is the periodicity of groups of modes the same as the spacing between fibers in the array. Small changes to the VIPA input angle (less than 0.1°) alter the spacing of the modes at the lenslet array so this can be tuned to the desired 250 μm mode separation. Shown in Figure 7.4 the phase difference between channel 1 and channel two is merely 0.7 radians. This corresponds to the shift in period over all four channels of the fiber array. So it makes sense that when looking at the center two channels in Figure 7.5, the phase difference (.2 radians) is approximately 1/3 that over all the channels.

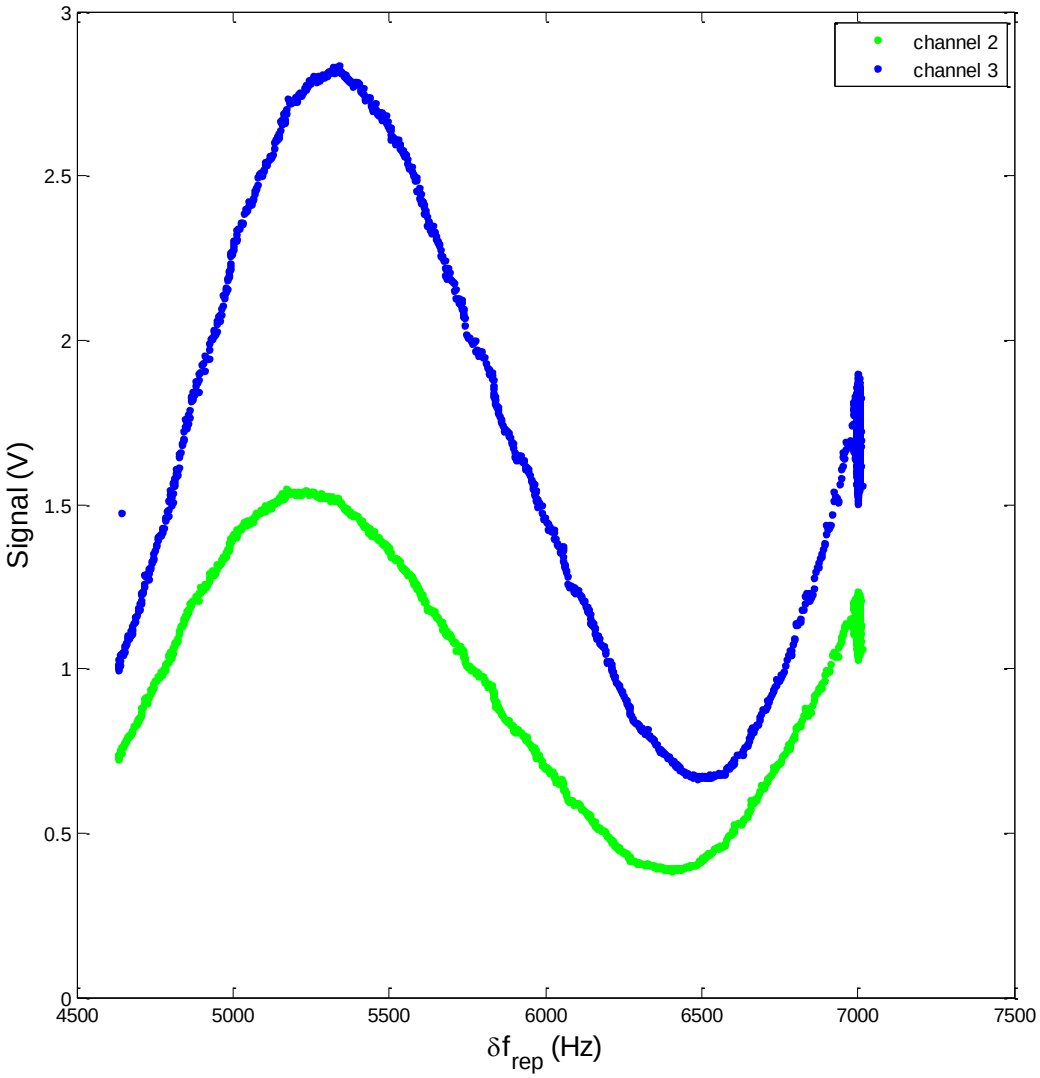


Figure 7.5: Power coupled into fiber array cannels: 2 in green and 3 in blue as a function of change in the repetition rate, $\Delta f_{rep}$.

The coupling efficiency of this setup can be calculated by comparing the power coupled into each channel as compared to the total power of a single channel. First the total power of a single group of modes needs to be measured. Using a slit at the focus of the 75 cm focal length lens, as shown in Figure 7.2, a single group of modes is isolated and the power measured by focusing the light into a power meter. The optical power of a single group of modes is measured to be 24

μW. The measured voltages in Figure 7.4 and Figure 7.5 can then be converted into optical power, *P*, using the relation

$$P = \frac{V}{rR} \tag{7.1}$$

where *R* is load, *r* is the responsivity of the detector, and *V* is the voltage detected. The voltages were measured using the alternate inputs to a Stanford Research Systems 830 Lock-in which have an input impedance of 1 MΩ. The detector used to measure channels 1 and 3 is a Thorlabs DET210 with a responsivity of 0.35 A/W at 810 nm and the detector used to measure channels 2 and 4 is a Thorlabs DET10c with a responsivity of .2 A/W at 810 nm. Using these values the maximum power coupled into each power is calculated:

| Channel number | Peak voltage (V) | Power (μW) | Efficiency (%) | Coupling loss (db) |
|---|---|---|---|---|
| 1 | 6.5 | 18.5 | 77 | -1.1 |
| 2 | 1.5 | 7.5 | 31 | -5.1 |
| 3 | 2.8 | 7.8 | 32 | -4.9 |
| 4 | 1 | 5 | 20 | -7.0 |

## 7.3 Fiber thermal drift and phase control

As seen previously in section 5.7 any difference in path lengths of the groups of modes to be shaped inside the pulse shaper introduces dispersion in the pulse shaper. In other words it is critical that the phase between these modes be controlled for pulse shaping to occur. Now that these modes have been separated into individual fibers, stabilizing this phase becomes an important issue that needs to be addressed.

Small changes in temperature cause small changes to the length and index of refraction of the glass that makes up the fiber. This in turn, causes the phase between separated modes to drift with respect to one another. To better study this effect, a test setup is built which uses CW 810 nm light as a source and a 50/50 fiber coupler to split the beam into two fiber paths and then after traveling 1 m another 50/50 fiber coupler is used to recombine the light as shown in Figure 7.6.

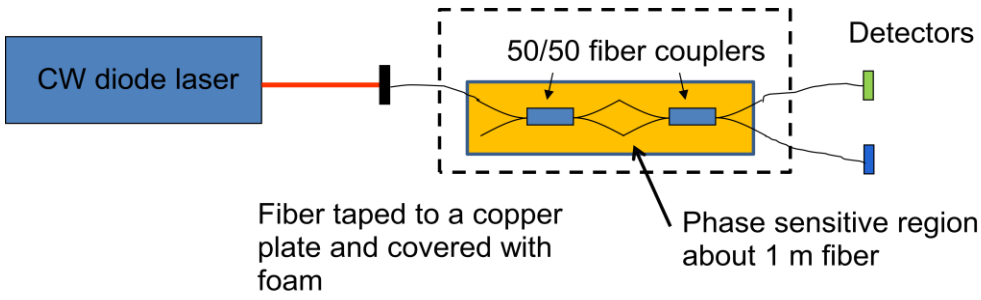


Figure 7.6: CW phase drift test setup, used to test phase stabilizing solutions necessary for control in the pulse shaper.

Cleary, any drift in the phase between the split modes will result in constructive or destructive interference of the source causing the power to shift from one output to the other output of the final 50/50 coupler. Figure 7.7 illustrates the natural phase drift in fiber. Observe the expected effect of how as the phase drifts between the two fibers, power shifts from one channel to the other. Keep in mind that the entire phase sensitive region of fiber is wrapped together, taped to a

copper plate, and insulated on all sides with 2 inch thick foam. This was done in an attempt to minimize the difference in temperature between the two fibers, to reduce the measured phase drift. There is still a substantial drift in the phase by $2\pi$ approximately every 5 seconds, the period of both of the measured signals in Figure 7.7.

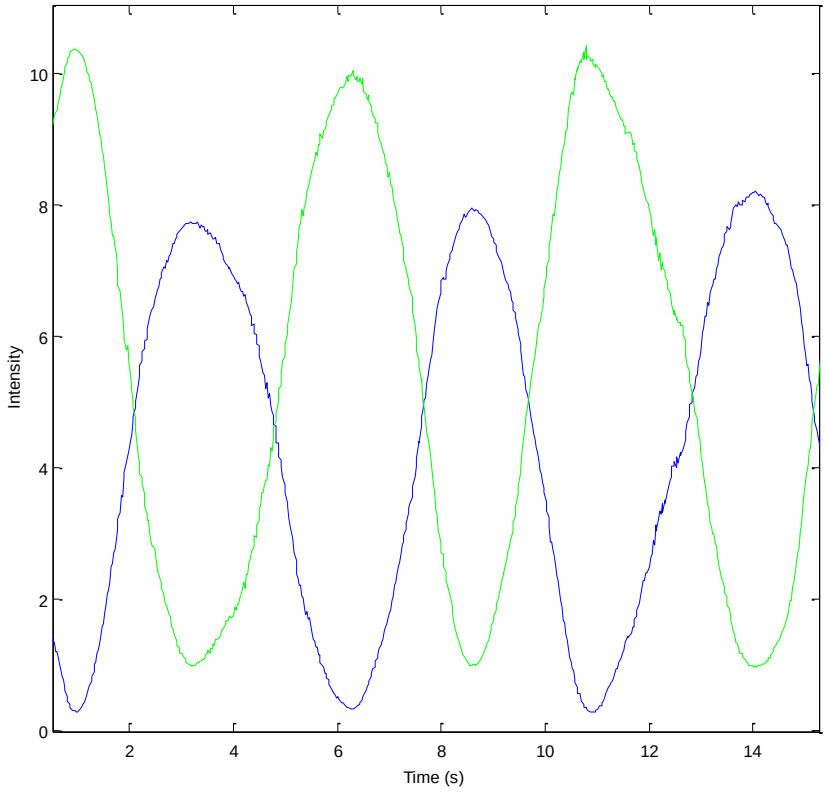


Figure 7.7: Free running CW phase drift setup data. The blue and green signals show the power detected in each output as a function of time. If the phase were constant between the two separate paths these signals would not fluctuate.

To solve this problem many techniques were explored. One technique takes advantage of the index of refraction's temperature dependence and by actively controlling the temperature of a section of phase sensitive fiber. To study this, a nichrome heater wire was wrapped very tightly to a 2 cm section of the phase sensitive fiber. By controlling current through the wire, the

temperature of the wire can be controlled. Changing the temperature of this section of fiber slowly affects the phase. It takes about half a second for the phase to start changing due to a change in the current in the nichrome wire and about 40 seconds for the temperature in the wire to reach thermal equilibrium. The slow response makes using this heater wire alone for active phase control a poor choice. To achieve a tight phase lock faster control is needed. Another technique explored was a fiber stretcher which makes use of a piezoelectric ceramic to physically stretch the optical fiber and alter its length. This much faster control over the length of the fiber enables much tighter phase locks to be obtained; however, the additional length of fiber (around 20 m) introduces unwanted normal dispersion to the groups of modes when used in the pulse shaper. So finally, a high speed delay and phase control device was designed and constructed using a fiber bench. A fiber bench couples fiber into free-space and then back into fiber, useful for placing free-space optics into a fiber system. In the setup shown in Figure 7.8 the space between the collimators of the fiber bench is used to control the delay and phase.

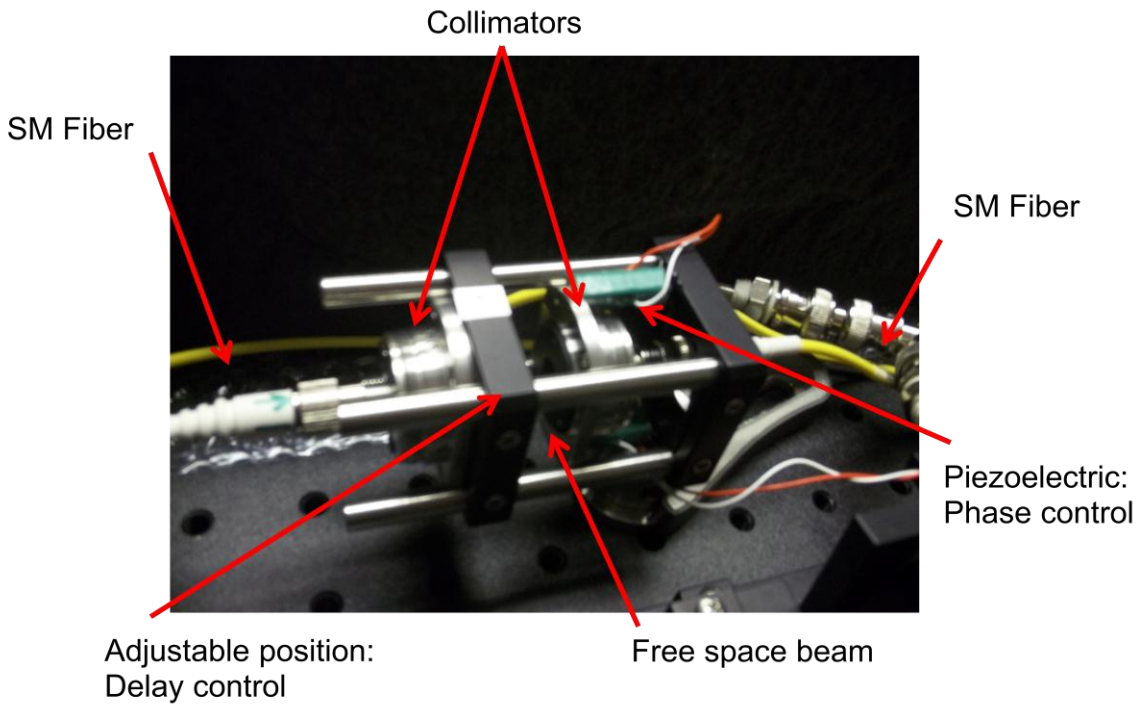


Figure 7.8: Fiber bench illustrating delay and phase control over a fiber line.

The delay of the free-space region is set by the adjustable placement of the fiber bench mounts and the phase is controlled by adjusting the voltage of a piezoelectric device attached to one of the collimators. Of all these techniques, the fiber bench provides the most robust control of the delay and phase of a fiber line.

To test the ability of the fiber bench to maintain a constant phase, a phase locked loop is constructed where the difference between voltages measured by the two outputs of the CW phase drift setup is used as an error signal. This error signal is then passed through a loop filter and used to control the voltage of the piezoelectric ceramic to maintain constant phase between the two phase sensitive fibers. Figure 7.9 shows data taken while stressing the loop.

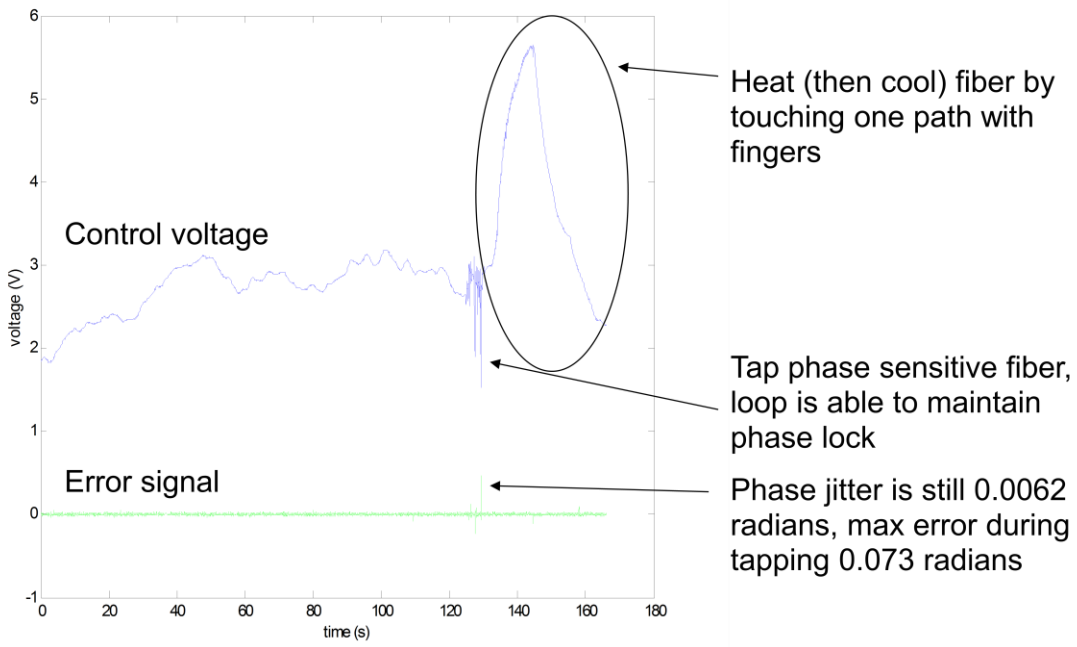


Figure 7.9: Phase locked loop data using the fiber bench in the CW phase drift test setup. The control voltage in blue is 1/15 the actual voltage applied to the piezoelectric transducer and the error signal in green is the difference between each measured output of the CW phase drift setup.

At 130 seconds the phase sensitive fiber is jostled; while this does propagate into some noise in the error signal, the phase locked loop is able to maintain lock. Then by heating the path of phase sensitive fiber that is not connected to the fiber bench with simply the warmth from two fingers, the voltage applied to the piezoelectric device is increased to expand the other path thereby maintaining phase lock. To verify the range of the piezoelectric device (17 μm) is adequate the phase sensitive setup is tested without insulation. The insulation from the CW phase drift setup is removed and the phase locked loop is again used to maintain the phase of the output. Results shown in Figure 7.10 show that the control voltage swings a maximum of 4 V, corresponding to 60 V applied to the piezo which is only 40% of the maximum 150 V that can be

applied. In other words, the piezo only needs to stretch 7.2 μm to maintain the phase locked loop accounting for laboratory thermal fluctuations.

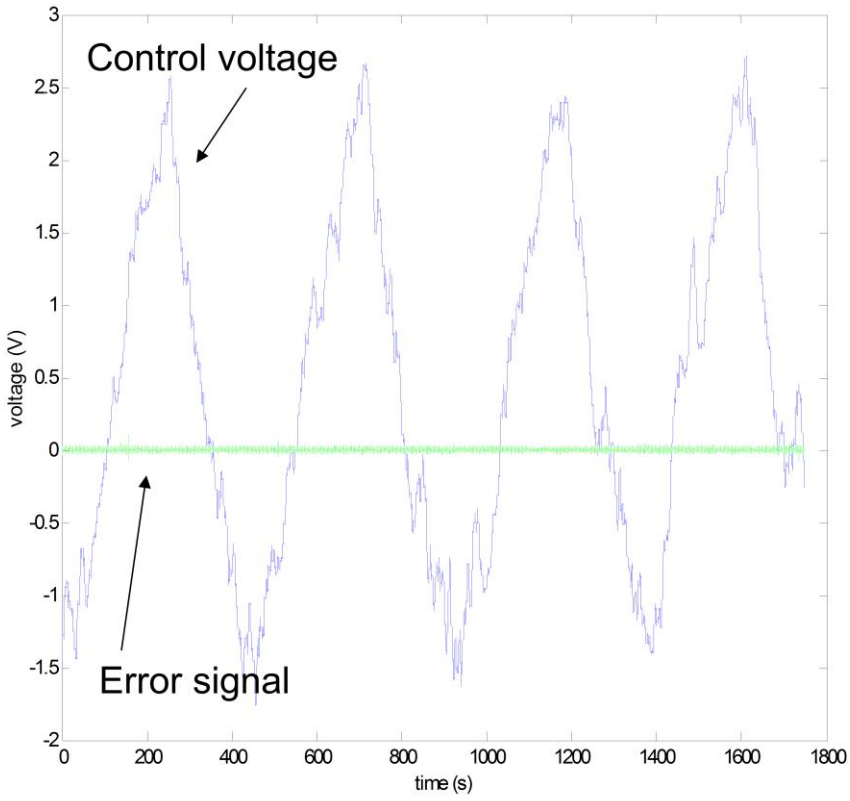


Figure 7.10: Phase locked loop data using the uninsulated fiber bench in the CW phase drift test setup. The swing in control voltage of 4 V corresponds to the piezoelectric device stretching by 7.2 μm.

# Chapter 8

# Conclusion and future work

## 8.1 Conclusion

Dynamic line-by-line pulse shaping is a useful technique in creating optical arbitrary waveform generation (OAWG). Having control over an optical waveform is a useful tool in a variety of fields. For instance, the accuracy of light detection and ranging (LIDAR) systems would be improved if custom tailored light waveforms were available. This is similar to what is already done with radio waves in radar systems.

This thesis has covered many aspects of dynamic line-by-line pulse shaping. Beginning with the basics of pulse shaping and frequency combs, the dynamic pulse shaping theory is developed. Then simulations are used to illustrate the nontrivial relationship between waveform fidelity and response speed of a dynamic line-by-line pulse shaper. Lowering the repetition rate of an input laser relaxes the high speed modulation requirements, but to achieve line-by-line pulse shaping, the individual modes that make up the frequency comb must be spectrally resolved from one another. The high spectral resolution required to achieve this for an 890 Mz repetition rate Ti:sapph source is achieved using a VIPA. This thesis presents the design, analysis and simulation of the VIPA used in the high spectral resolution line-by-line pulse shaper. Nonideal VIPA behavior is discussed as well as its effects on the VIPA-based pulse shaper. In working toward making the pulse shaper dynamic, several modulation technologies are explored and discussed. The VIPA-based pulse shaper is then modified to couple adjacent groups of comb lines into separate SM fibers in preparation for high speed modulation. Once groups of modes are coupled into separate fibers phase stabilization becomes necessary. The

custom fiber bench designed to control the delay and phase of a fiber path is shown to provide the necessary phase stabilization in a phase-locked loop.

Substantial progress has been made towards OAWG, although it has not been demonstrated due to the difficulty of simultaneously achieving high spectral resolution and high modulation rate. A combination of this project's success with high spectral resolution and work done with high speed VCSELs [10] would result in OAWG.

## 8.2 Future work

The next step for this project is to demonstrate static line-by-line pulse shaping using the optical setup where adjacent groups of comb lines are coupled into SM fibers. This requires that the phase between modes is locked using the aforementioned fiber bench so the intended output waveform can be created. Once successful, high speed fiber modulators can be installed to generate dynamic line-by-line pulse shaping. Note the high insertion loss of the VIPA in addition to its bandwidth limitations result in very low power (24 μW) in each group of modes. Successful amplification of the optical signal would not only help account for the loss of power due to losses in the high speed modulators, but provide additional signal strength to more easily measure the dynamic response of the pulse shaper.

As expounded upon in section 3.1 the compromise that must be made between waveform fidelity and response speed is a result of the high resolution spectral recombination of the pulse. It is here that the high speed sidebands of the modulated individual comb lines are filtered out reducing the response speed of a dynamic line-by-line pulse shaper. A solution to circumvent this limitation is to build a pulse shaper in transmission geometry. This means instead of retro-reflecting shaped comb lines back to the original spectrally dispersive device, the individual

modes of the pulse are recombined using non-spectral means, for example using beam splitters or fiber couplers. This has the advantage of not filtering out the high speed sidebands, thereby enabling instantaneous control over the pulse shaper output with fully arbitrary waveform capability provided by line-by-line pulse shaping.

In general this enhanced response comes at the price of pulse shaper efficiency. By the constant radiance theorem, as the modes are spatially recombined using spectral independent methods, half of the power is lost at each 50/50 coupler. This would devastate the signal if each individual mode were recombined with every other mode, however the VIPA-only pulse shaper described in section 5.2 already groups modes together (separated by the VIPA FSR) over the entire spectrum and many useful waveforms can be created by simply modulating 4 adjacent groups of modes (section 5.6 ) Remember that the insertion loss through the VIPA is approximately 9 db, if only 4 modes need to be recombined, this can be done at a cost of only 6 db of loss using simple 50/50 fiber couplers (3 db loss per 50/50 coupler) as illustrated in Figure 8.1. In the case that only 4 modes are recombined, it is more power efficient to recombine the pulse train using standard 50/50 beam splitters than it is to use the VIPA.

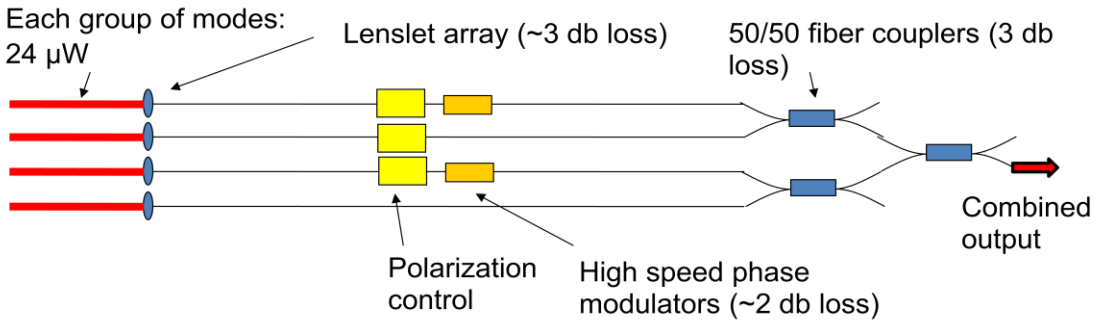


Figure 8.1: Transmission geometry of a dynamic pulse shaper, where the pulse shaped output is combined using standard 50/50 fiber couplers instead of a spectrally dispersive device.

Removing the constraint of spectral recombination enables the transmission geometry pulse shaper to circumvent the limitations imposed by the dynamic pulse shaping theory (based on spectral recombination). However, a transmission type pulse shaper is only efficient when few modes (or groups of modes) are used for shaping. The constant radiance theorem dictates that non spectral recombination of the pulse will result in an output that has only as much power as a single mode or mode group, limiting the scalability of this scheme.

# Bibliography

[1] A. M. Weiner, “Femtosecond pulse shaping using spatial light modulators,” Rev. Sci. Instrum., vol. 71, pp. 1929–1960, (2000).

[2] Shijun Xiao, Andrew M. Weiner, and Christopher Lin, “Experimental and Theoretical Study of Hyperfine WDM Demulitplexer Performance Using the Virtually Imaged Phased- Array (VIPA),” J. Lightwave Technol 23, ( 2005).

[3] S. A. Diddams, L. Hollberg, and V. Mbele, “Molecular fingerprinting with the resolved modes of a femtosecond laser frequency comb,” Nature 445, 627-630 (2007).

[4] Z. Jiang, D.-S. Seo, D. E. Leaird, and A. M. Weiner, “Spectral line-by-line pulse shaping,” Opt. Lett. 30, 1557-1559 (2005).

[5] Z. Jiang, C.-B. Huang, D. E. Leaird, and A. M. Weiner, “Optical arbitrary waveform processing of more than 100 spectral comb lines,” Nat. Photonics 1, 463-467 (2007).

[6] S. T. Cundiff and A. M. Weiner, “Optical arbitrary waveform generation,” Nat. Photonics (11), 760–766 (2010).

[7] J. T. Willits, A. M. Weiner, and S. T. Cundiff, “Theory of rapid-update line-by-line pulse shaping,” Opt. Express 16(1), 315–327 (2008).

[8] D. J. Jones, S. A. Diddams, J. K. Ranka, A. Stentz, R. S. Windeler, J. L. Hall, and S. T. Cundiff, "Carrier envelope phase control of femtosecond mode-locked lasers and direct optical frequency synthesis," Science 288, 635-639 (2000).

[9] J. Ye and S. T. Cundiff, eds., *Femtosecond Optical Frequency Combs Technology: Principle, Operation, and Application* (Springer, New York, 2004).

[10] M. Akbulut, S. Bhooplapur, I. Ozdur, J. Davila-Rodriguez, and P. J. Delfyett, "Dynamic line- by-line pulse shaping with GHz update rate," Opt. Express Vol. 18, No. 17 (2010).

[11] R. P. Scott, N. K. Fontaine, J. P. Heritage, and S. J. B. Yoo, “Dynamic optical arbitrary waveform generation and measurement,” Opt. Express 18(18), 18655–18670 (2010).

[12] J. T. Willits, A. M. Weiner, and S. T. Cundiff, "Line-by-line pulse shaping with spectral resolution below 890 MHz," Opt. Express Vol. 20, No 3 (2012).

[13] A. Artels, T. Dekorsy, and H.Hurz, “Femtosecond Ti:sapphire ring laser with 2-GHz repetition rate and its application in time-resolved spectroscopy,” Optics Letters Vol. 24 No. 14 (1999).

[14] J. P. Heritage, R. N. Thurston, W. J. Tomlinson, A. M. Weiner, and R. H. Stolen, Appl. Phys. Lett. 47, 87 (1985).

[15] J. P. Heritage, A. M. Weiner, and R. N. Thurston, Opt. Lett. 10, 609 (1985).

[16] A. M. Weiner, D. E. Leaird, J. S. Patel, and J. R. Wullert, IEEE J.Quantum Electron. 28, 908 (1992).

[17] W. Kaiser, *Ultrashort Laser Pulses and Applications* Springer, Berlin, (1988).

[18] N. Hoghooghi, I. Ozdur, M. Akbulut, J. Davila-Rodriguez, and P. J. Delfyett, "Resonant cavity linear interferometric intensity modulator," Opt. Lett. 35(8), 1218–1220 (2010).

[19] O. E. Martinez, "Grating and prism compressors in the case of finite beam size," J. Opt. Soc. Am. B 3, 929-934 (1986).

[20] R. N. Thurston, J. P. Heritage, A. M. Weiner, and W. J. Tomlinson, "Analysis of picoseconds pulse shape synthesis by spectral masking in a grating pulse compressor," IEEE J. Quantum Electron. 22, 682-696 (1986).

[21] M. M. Wefers and K. A. Nelson, "Space-time profiles of shaped ultrafast optical waveforms," IEEE J. Quantum Electron. 32, 161-172 (1996).

[22] J. Paye and A. Migus, "Space-time Wigner functions and their application to the analysis of a pulse shaper," J. Opt. Soc. Am. B 12, 1480-1491 (1995).

[23] R. D. Nelson, D. E. Leaird, and A. M. Weiner, "Programmable polarization-independent spectral phase compensation and pulse shaping," Opt. Express 11, 1763-1769 (2003).

[24] H. P. Sardesai, C-.C Chang, and A. M. Weiner, "A femtosecond code-division multiple-access communication system testbed," J. Lightwave Technol. 16, 1953-1964 (1998).

[25] J. W. Goodman, *Introduction to Fourier Optics* (McGraw-Hill, New York, 1968).

[26] H. A. Haus, *Waves and Fields in Optoelectronics* (Prentice-Hall, Englewood Cliffs, New Jersey, 1984).

[27] Z. Bor and B. Racz, Opt. Commun. 54, 165-170 (1985).

[28] F.J. Harris, "Spectral analysis windowing," Wiley Encyclopedia of Electrical and Electronics Engineering, (Wiley, New York Vol. 20, pp. 88-105. 1999).

[29] M. Shirasaki, "Large angular dispersion by a virtually imaged phased array and its application to a wavelength demultiplexer," Opt. Lett., vol. 21, pp. 366–368, (1996).

[30] J. M. Vaughan, "The Fabry-Perot Interferometer: History, Theory, Practice and Applications," Taylor and Francis Group (1989).

[31] R. C. Hansen, "Phased Array Antennas, Second Edition," John Wiley and Sons, Inc. (2009).

[32] S. Xiao, A. M. Weiner, C. Lin. “A dispersion law for virtually imaged phased array spectral dispersers based on paraxial wave theory.” IEEE Journal of Quantum Electronics, vol. 40, no. 4, pp 420-426, (2004).

[33] S. Xiao, and A. M. Weiner, “An Eight-Channel Hyperfine Wavelength Demultiplexer Using a Virtually Imaged Phased-Array (VIPA)” IEEE Photonics Tech. Let., 17, 372-374 (2005).

[34] S. Xiao, A. M. Weiner, and C. Lin, “Experimental and Theoretical Study of Hyperfine WDM Demulitplexer Performance Using the Virtually Imaged Phased-Array (VIPA),” J. Lightwave Tech. 23 ( 2005).

[35] R.P. Scott, N. K Fontaine, D.J. Geisler, T. He, J.P. Heritage, and S.J.B. Yoo, “Demonstration of dynamic optical arbitrary waveform generation with 5-ns record lengths and 33-ps features,” CLEO 2011, paper CWH5 (2011).

[36] T.K. Chan, J. Karp, R. Jiang, N. Alic, S. Radic, C.F. Marki, J.E. Ford, "1092 channel 2-D array demultiplexer for ultralarge data bandwidth," Journal of Lightwave Technology, 25 719-725 (2007).

[37] S. Xiao and A. Weiner, "2-D wavelength demultiplexer with potential for $\geq$ 1000 channels in the C-band," Opt. Express 12, 2895-2902 (2004).

[38] C. Lin, M. Shirasaki. “Analysis of coating design in a virtually imaged phased array (VIPA) chromatic dispersion compensator.” Proceedings, Photonics West (2001).

[39] Fleming, J.W.; , "Material dispersion in lightguide glasses," Electronics Letters , vol.14, no.11, pp.326-328, May 25 (1978).

[40] G. K. White “Thermal expansion of reference materials: copper, silica and Silicon,” J. Phys. D 6, 2070 (1973).

[41] T. Toyoda and M. Yabe, "The Temperature Dependence of the Refractive Indices of Fused Silica and Crystal Quartz," J. Phys. D 16, L97 (1983).

[42] A. M Weiner, *Ultrafast optics* John Wiley & Sons (2009).

[43] H. P. Sardesai, A. M. Weiner, "Higher-order fiber dispersion compensation using a pulse shaper with programmable phase-modulator array," OFC '98., Technical Digest (1998).

[44] Anatoly Efimov and David H. Reitze, "Programmable dispersion compensation and pulse shaping in a 26-fs chirped-pulse amplifier," Opt. Lett. 23, 1612-1614 (1998).

[45] V. R. Supradeepa, Ehsan Hamidi, Daniel E. Leaird, and A. M. Weiner, "New Aspects of Temporal Dispersion in High Resolution Fourier Pulse Shaping: A Quantitative Description with Virtually Imaged Phased Array Pulse Shapers." J. Opt. Soc. Am. B, 27 1833-1844 (2010).

[46] G. H. Lee, A. M. Weiner, "Programmable Optical Pulse Burst Manipulation Using a Virtually Imaged Phased Array (VIPA) Based Fourier Transform Pulse Shaper," J. Lightwave Tech., 23 3916-3923 (2005).

[47] O. Mitomi, *High-Speed LiNbO3 Optical Modulators* (Taylor and Francis Group, LLC 2007).

[48] Ivan P. Kaminow, *Handbook of Optical Constants of Solids Volume 4* (Academic Press, 1998).

# Appendix A: Dynamic pulse shaping simulation

```
% General Pulse Shaping Simulation
% Double Integral implementation

clear all
close all

% Input spectrum
sample = 256;
width=sample/16;
A=(rem(((1:sample)-sample/2-1),8)==0).*exp(-((1:sample)-1*sample/2-
1).^2/width^2);

% create indexes for plotting
timestep=0.0313*10^-9;
xi=1:sample;
xt=xi*timestep;                                    %in s
xw=(xi-sample/2-1)/(sample*timestep);              %in Hz  center freq = 0
but in reality everything is offset by 375THz since we are at 800nm
xx=(xi-sample/2-1)*2.5*10^-6;                      %20um spacing between
modes

% View the input
figure(1)
plot(xw,A)
title('Input A(w)');

figure(2)
plot(xt,real(fftshift(ifft(fftshift(A)))))
title('At: real');

% Create a space-time mask Mst and the temporal fft Msw
Msw=zeros(sample);  % frequency response in time
Mst=zeros(sample);  % time diagnostic

% Modulate in time

%better F tranform if in fractions of 1/8 so we get an integral number of
cosine functions and therefore a repeating pattern
%timemodulationfrequency=10^9*2*pi*2/(8);        %2/8*10^9=250MHz

Mt=1*(1-cos(10^9*2*pi*3/(8)*xt))/2;

figure(10)
plot(xt, real(Mt))
title('Mt: real');

% Turn off time modulation by uncommenting the next line
% Mt=ones(sample,1);
```

```
% Convert to phase modulation by uncommenting the next line
% Mt=exp(i.*Mt);

Mtempw=fftshift(fft(fftshift(Mt)));

figure(11)
plot(xw, real(Mtempw))
title('Mtempw: real');

%static combline in time needs to be converted to frequency for the mask
Mxs=ones(sample,1)';
% Convert to phase modulation by uncommenting the next line
% Mxs=exp(i.*Mxs);
Mxsw=fftshift(fft(fftshift(Mxs)));

% Create spatial frequency mask
flip=1;
for ci=1:sample
    if(rem(ci-sample/2-1+3,8)==0)
        if flip==1
            flip=0;
        else
            flip=1;
        end
    end
    if flip == 0
       Msw(ci,:)=Mtempw(:)';
       Mst(ci,:)=Mt(:)';
   else
        Msw(ci,:)=Mxsw;
        Mst(ci,:)=Mxs(:)';
    end
end

% View the mask
figure(70)
pcolor(xw,xx,real(Msw))
title('Msw real');

figure(71)
pcolor(xw,xx,imag(Msw))
title('Msw imaginary');

figure(72)
pcolor(xt,xx,real(Mst))
title('Mst real');

figure(73)
pcolor(xt,xx,imag(Mst))
title('Mst imaginary');

figure(74)
plot(xx,Mst(:,1))
hold on
plot(xx,A)
```

```
hold off


% PULSE SHAPER VALUES

%Mask that is always on  (make more effiecent)
Mon=zeros(sample);
for ci=1:sample
    Mon(ci,:)=fftshift(fft(fftshift(ones(sample,1)')));
end

% gaussian values
alpha=20*10^-6/(1*10^9);       %frequency to um conversion 20um to 1GHz for
example
w0=5*10^-6;                  %spot size radius

%spectral smear squash, this value reduces the effect of spectral smearing
ss=1;

dw = abs(xw(1)-xw(2));
dx = abs(xx(1)-xx(2));   %abs(1/256);

% SHAPER EVALUATION
pi=10;
for ci=1:pi
    w0=ci*2.5*10^-6;
    Aout = shaper(A,Msw,sample,alpha,w0,ss,dw,dx,Mon);
    sideband(ci)=abs(Aout(sample/2+1+8+3));
    sideband_c(ci)=abs(Aout(sample/2+1+8));
end

sideband_p=sideband/abs(A(sample/2+1+8))*100;
sideband_cp=sideband_c/abs(A(sample/2+1+8))*100;

% SHAPER OUTPUT
figure(4)
plot(xw, real(Aout))
title('Aout real')

figure(40)
plot(xw, abs(Aout))
title('Aout abs')

figure(5)
plot(xw, imag(Aout))
title('Aout imag')

figure(6)
plot(xt, real(fftshift(ifft(fftshift(Aout)))))
title('Aout_t: real');

figure(7)
plot(xt, imag(fftshift(ifft(fftshift(Aout)))))
title('Aout_t: imag');
```

```
figure(8)
plot(xt, real(fftshift(ifft(fftshift(Aout)))).^2)
title('Aout_t: intensity');

% Smearing Function
smear = exp(-(0-alpha.*((1:sample)-sample/2-1).*dw).^2/(w0^2));
smear2 = exp(-ss*(0-alpha.*((1:sample)-sample/2-1).*dw).^2/(w0^2));
figure(9)
plot(xw,smear.*smear2)
title('Smearing Function at x=0, w shift=0');

figure(10)
plot(5*10^-6*(1:pi),sideband_p)
title('sideband power vs w0')

figure(11)
plot(5*10^-6*(1:pi),sideband_cp)
title('center power vs w0')


--------------------------------------------------------------------------


%shaper.m
%Heart of the pulse shaping simulation
%performs the double integral

function [Aout]=shaper(A,Mst,sample,alpha,w0,ss,dw,dx,Mon)

Aout=zeros(sample,1);

for q=1:sample
    total=0;
    norm=0;
    for qw=1:sample
        if((q-(qw-sample/2-1))>=1 & (q-(qw-sample/2-1)) <= sample)
            total=total+dx*dw*A(q-(qw-sample./2-1))*sum(exp(-(((1:sample)-
sample/2-1)*dx-alpha*(q-sample/2-1)*dw).^2/(w0^2)).*exp(-ss*(((1:sample)-
sample/2-1)*dx-alpha*((q-sample/2-1)*dw-(qw-sample./2-
1)*dw)).^2/(w0^2)).*Mst((1:sample),qw)');
            norm=norm+dx*dw*                          sum(exp(-(((1:sample)-
sample/2-1)*dx-alpha*(q-sample/2-1)*dw).^2/(w0^2)).*exp(-ss*(((1:sample)-
sample/2-1)*dx-alpha*((q-sample/2-1)*dw-(qw-sample./2-
1)*dw)).^2/(w0^2)).*Mon((1:sample),qw)');
        end
    end
    Aout(q)=total/norm;
end
```

# Appendix B: Gaussian beam VIPA construction

```
%John Willits
%VIPA simulation
%setup an array of Gaussian images to reproduce a VIPA

% close all
% clear all
clear x z E

%%%%%%%%%%%%%%%%%%%%%%%%%%%%%%

%set constants

lambda = .815;                  %value in microns
%lambda = .81500022;               %value in microns for adjacent mode
(100MHz) calculated from: (3*10^8/(3*10^8/(815*10^-9)+100*10^6))*10^6
%lambda = .815002;                %value in microns adjacent mode (about 1
GHz)
%lambda = .815052;                %value in microns a full VIPA FSR
difference (25GHz)

thickness = 4.1*10^3;       %VIPA thickness in um (4.1 orig value vs 42)

index=1.44;                 %index of refraction for fused silica, eventually
make this dep on wavelength to show dispersion 1.44

d=10*10^3;                 %a bit less than 1 inch long surface (23.5*10^3
for Aero-VIPA)

w0 = sqrt(thickness*lambda/(pi*index))     %calculate ideal input spot size
on back mirror of VIPA
%w0 = 27;                     %Gaussian waist input (27 orig value)

edge = 100;                 %transition on window
safety = 1;                 %safety factor on the window 1 = 1/e value for
both input and first reflection
theta_in=atan((2*sqrt(2)*w0*safety+edge)/(thickness*2))         %calculate
ideal input angle in rad
theta_in*180/pi
theta_in=1.01*pi/180;                                            %set input
angle into the VIPA in radians (1.21 deg orig value)


spatial_delay=2*index*thickness*cos(theta_in)  %*299792458*1/(FSR)*10^6;
%distance in z to offset images in um
x_offset = 2*index*thickness*sin(theta_in)  %distance in x to offset images
in um (this should work), but sometimes it isn't the same as the other
x_offset0 = (2*sqrt(2)*w0*safety+edge)

% bounces = 57;               %number of VIPA spots to image (57 orig value)
% d = bounces*x_offset        %distance between upper and lower most images
```

```
bounces = floor(d/x_offset)         %calculate number of bounces for a given
input angle...

last_image = (bounces-1)*spatial_delay   %location of end of VIPA in um

boundary = 1;               %value 1 turns absorbing boundary on, 0 for off

z0 = last_image+1.55*10^6                  %Distance to travel in z in
microns

expon = 6;

nx = 2^12;                   %number of samples in x helpful in powers of 2
(old value 2^13)
delta_x = 8;%lambda;           %sample spacing (old value = 4)

nz = 2^11;                   %number of samples in z (10 = old value)
delta_z = z0/nz          %step size in z

focus=0.75*10^6;                %imaging focal point in um
lplace=last_image+0.75*10^6;                %lens placement in um

%%%%%%%%%%%%%%%%%%%%%%%%%%%%%%

%array of x and z values used for graphing
x=delta_x.*(-nx./2):delta_x:delta_x.*(nx./2-1);
z=0:delta_z:delta_z.*(nz-1);

%air
n1(1:nx)=1;

%
% figure
% plot(x,n1)

%step function
ko = 2*pi/lambda;   %maybe use an n here?
delta_kx = 2*pi*n1/(nx*delta_x);
kx=delta_kx.*(-nx./2):delta_kx:delta_kx.*(nx./2-1);
kz = sqrt(ko^2-kx.^2);

%non-paraxial
H=exp(-i*kz*delta_z);

%first image
E(1,:) = exp(-(x-d/2).*(x-d/2)/(w0)^2);

%E(1,:) = exp(-(x).*(x)/(w0)^2);

w = 20;         %taper value for boundary conditions (10 original value)
```

```
qq=1;           %image number

correction = 0;


for n=1:1:nz-1
    if(abs((n)*delta_z-(lplace+focus+correction))<delta_z)
        if(((n)*delta_z-(lplace+focus+correction)) < 0)
            %just before image plane
            %transition perfectly to the plane (different delta_z)
            E(n+1,:) = ifft(ifftshift(fftshift(fft(E(n,:))).*exp(-
i*kz*abs((n)*delta_z-(lplace+focus+correction)))));
            iplane=n+2  %I thought it should be just n+1..
        else
            %transition to next slice (rest of the way), second hit
            E(n+1,:) = ifft(ifftshift(fftshift(fft(E(n,:))).*exp(-
i*kz*(delta_z-abs((n-1)*delta_z-(lplace+focus+correction))))));
            n
        end
    else
        %normal propagation
        %Diffraction
        E(n+1,:) = ifft(ifftshift(fftshift(fft(E(n,:))).*H));
    end

    %multiply by pos_dep_phase (resulting from inhomogenous part of n)
    Refraction
    E(n+1,:) = E(n+1,:).*exp(-i*2*pi/lambda*delta_z*n1);

    %simulate a lens to focus the VIPA
    %http://www.iue.tuwien.ac.at/phd/kirchauer/node51.html
    %phase change: exp(-i*ko*(x^2+y^2)/(2F)), we only have the x axis, F=(n-
1)(1/r1-1/r2)  (but we only care about f)

%     if(n==nz*3/4)
    if(abs(n*delta_z-lplace)<=delta_z/2)
        %place lens
        n
        %perfect lens
        E(n+1,:) = E(n+1,:).*exp(i*ko*((x).*(x))/(2*focus));
        correction = n*delta_z-lplace;
        %spherical lens
        %E(n+1,:) = E(n+1,:).*exp(-i*ko*(sqrt((focus)^2-((x).*(x)))-
(focus)));
    end




    %Boundary code
    if (boundary == 1)
        for c=1:1:floor(nx/20)
            E((n+1),c) = E((n+1),c)*exp(-(c-floor(nx/20))^2/w);
        end
        for c=(nx-ceil(nx/20)):1:nx
```

```
            E((n+1),c) = E((n+1),c)*exp(-(c-(nx-ceil(nx/20)))^2/w);
        end
    end

    %add another image
    if(mod(n*delta_z,spatial_delay)< delta_z & (qq*x_offset<d))
        E(n+1,:)=E(n+1,:)+exp(-(x-d/2+x_offset*qq).*(x-
d/2+x_offset*qq)/(w0)^2);
        qq=qq+1;
        if (qq == bounces)
            disp('end VIPA, location:')
            n*delta_z
            n
        end
    end

end


%make plots
figure
pcolor(z,x,abs(E)'); colormap((gray)); shading interp;


figure
plot(abs(E(iplane,:)))
title('abs(E) at image plane')
xlabel('distance (um)')
ylabel('magnitude of E')
```

# Appendix C: VIPA spectral and temperature dependence

```
%VIPA FSR changes due to fused silica index of refraction changes
%spectral (fused silica dispersion)
%temperture (index of refraction change with temp and VIPA thickness)

close all
clear all

lambda=0.750:.0001:0.850;

for ci=1:length(lambda)
    n(ci)=sqrt(1+0.696166300*lambda(ci)^2/(lambda(ci)^2-4.67914826*10^-
3)+0.407942600*lambda(ci)^2/(lambda(ci)^2-1.35120631*10^-
2)+0.897479400*lambda(ci)^2/(lambda(ci)^2-97.9340025));
end

lambda0=0.810;
n0=sqrt(1+0.696166300*lambda0^2/(lambda0^2-4.67914826*10^-
3)+0.407942600*lambda0^2/(lambda0^2-1.35120631*10^-
2)+0.897479400*lambda0^2/(lambda0^2-97.9340025));
```

```
c=3*10^8;

FSR0=890.4*10^6*28

t0=c/(FSR0*2*n0)

FSR=c./(2.*t0.*n);

delta_FSR=FSR-FSR0;

figure
plot(lambda,n)
ylabel('index of refraction')
xlabel('wavelength (\mum)')
set(gcf,'position',[700,100,800,800])

figure
plot(lambda,n-n0)
ylabel('\delta index of refraction')
xlabel('wavelength (\mum)')
set(gcf,'position',[700,100,800,800])

figure
plot(lambda,FSR)
ylabel('VIPA FSR')
xlabel('wavelength (\mum)')
set(gcf,'position',[700,100,800,800])

figure
plot(lambda,delta_FSR)
ylabel('\delta VIPA FSR')
xlabel('wavelength (\mum)')
set(gcf,'position',[700,100,800,800])

Show how change in VIPA FSR affects mixing of modes in VIPA-only pulse
shaping

clear n,ci,FSR

lambda0=0.810;
c=3*10^8;
n0=sqrt(1+0.696166300*lambda0^2/(lambda0^2-4.67914826*10^-
3)+0.407942600*lambda0^2/(lambda0^2-1.35120631*10^-
2)+0.897479400*lambda0^2/(lambda0^2-97.9340025));
FSR0=890.4*10^6*28
t0=c/(FSR0*2*n0)
lambda2=zeros(1000,1);     %array length determines how many steps to take in
the horizontal direction (each step is another mode of the VIPA)

lambda2(1) = lambda0;   %start at the center

%manually calculate first values
```

```
n(1)=sqrt(1+0.696166300*lambda2(1)^2/(lambda2(1)^2-4.67914826*10^-
3)+0.407942600*lambda2(1)^2/(lambda2(1)^2-1.35120631*10^-
2)+0.897479400*lambda2(1)^2/(lambda2(1)^2-97.9340025));
FSR(1)=c./(2.*t0.*n(1));
%delta f calculations
delta_f(1)=(FSR(1)/(890.4*10^6)-28)*(890.4*10^6);
total_f(1)=delta_f(1);

for ci=2:length(lambda2) %VIPA step number (horizontal motion)
    %calculate next wavelength (from changing VIPA FSR)
    v=c/(lambda2(ci-1)*10^-6);                %calculate last optical
frequency from wavelength in um
    lambda2(ci)= (c/(v-FSR(ci-1)))*10^6;      %add VIPA FSR and calculate
next wavlength in um
    delta_lambda(ci)=lambda2(ci)-lambda2(ci-1);


    n(ci)=sqrt(1+0.696166300*lambda2(ci)^2/(lambda2(ci)^2-4.67914826*10^-
3)+0.407942600*lambda2(ci)^2/(lambda2(ci)^2-1.35120631*10^-
2)+0.897479400*lambda2(ci)^2/(lambda2(ci)^2-97.9340025));
    FSR(ci)=c./(2.*t0.*n(ci));
    %delta f calculations
    delta_f(ci)=(FSR(ci)/(890.4*10^6)-28)*(890.4*10^6);
    total_f(ci)=total_f(ci-1)+delta_f(ci);
end


figure
plot(delta_lambda)
set(gcf,'position',[700,100,800,800])

figure
plot(lambda2)
set(gcf,'position',[700,100,800,800])

figure
plot(lambda2,n)
xlabel('wavelength (\mum)')
ylabel('frequency (Hz)')
set(gcf,'position',[700,100,800,800])

figure
plot(lambda2,FSR)
xlabel('wavelength (\mum)')
ylabel('frequency (Hz)')
set(gcf,'position',[700,100,800,800])

figure
plot(lambda2,delta_f)
xlabel('wavelength (\mum)')
ylabel('frequency (Hz)')
set(gcf,'position',[700,100,800,800])

figure
plot(lambda2,total_f)
```

```
xlabel('wavelength (\mum)')
ylabel('frequency (Hz)')
set(gcf,'position',[700,100,800,800])
```

# Appendix D: Calculating β-$BaB_2O_4$ phase matching bandwidth

The beta barium borate, $\beta$-$BaB_2O_4$, (BBO) crystal used in the cross-correlation setup is 5 mm thick. This thick crystal was used to increase the sensitivity of the cross-correlator since the output of the VIPA-only line-by-line pulse shaper is so weak at only 30 μW. The longer the interaction length of the signal and reference beams, the less optical bandwidth of the signal that is detected. This reduction in bandwidth is due to differences in the index of refraction between the generated second harmonic light and the signal and reference. To begin this analysis, the geometry of the BBO crystal is examined.

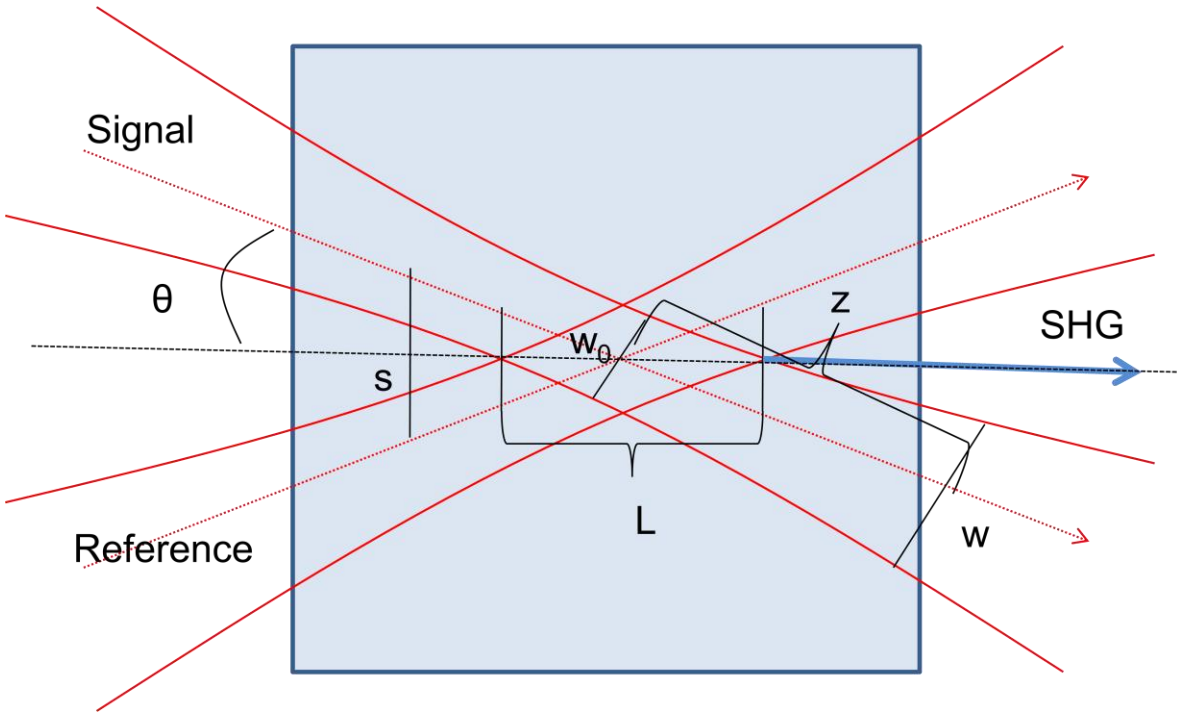


Figure 11.1: Beam geometry inside BBO crystal. The details of how these beams are imaged inside the BBO crystal are used to calculate the active region, *L*, inside the crystal.

The full length of the crystal alone does not determine the bandwidth of the cross-correlation signal. Imagine a long crystal with beams propagating through it, only when these beams overlap one another, or interact with one another, is a cross-correlation signal created. The beams interact with one another while the separation between the beams is less than the radius, *w*, of the beam. Gaussian beam propagation yields the spot size as a function of the propagation direction, *z*, to be

$$w(z) = w_0\sqrt{1+\frac{z^2}{Z_R^2}} \tag{11.1}$$

where $w_0$ is the beam waist radius of the spot at the focus and $Z_R$ is the Rayleigh range of the signal and reference calculated by

$$Z_R = \frac{\pi w_0^2}{\lambda} \tag{11.2}$$

where λ is the wavelength. The separation, *s*, between the modes is calculated geometrically to be

$$s = z\sin(\theta) \tag{11.3}$$

Equations (11.1) and (11.3) are set equal and rearranged to solve for *z*

$$z = \frac{w_0}{\sqrt{\sin^2(\theta)-\frac{w_0^2}{Z_R^2}}} \tag{11.4}$$

Note that this relation is valid only when $\theta > \lambda/\pi$. The interaction length, *L*, can now be solved from *z*

$$L = 2z\cos(\theta) \tag{11.5}$$

This calculation for $L$ assumes that the crystal is thicker than $L$. If the crystal is thinner than $L$, then the crystal itself limits this interaction length.

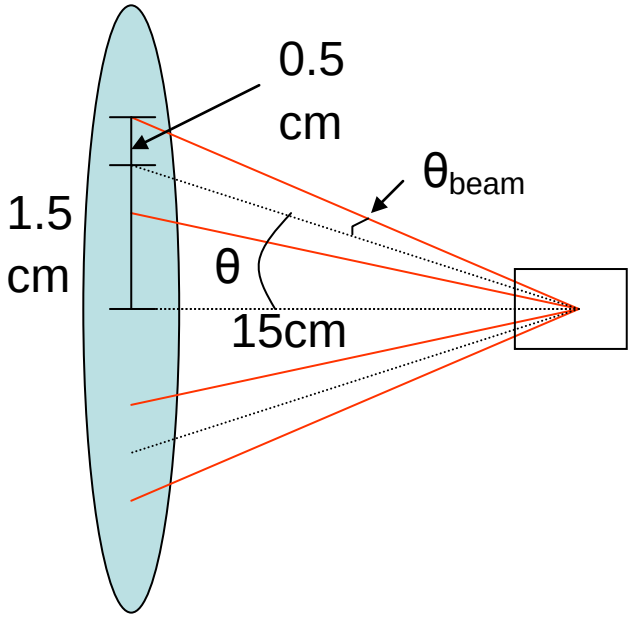


Figure 11.2: Details of signal and reference beams as they are focused to the BBO crystal. The physical dimensions of the beams in addition to the converging angle of each beam $\theta_{beam}$ are used to calculate the Rayleigh Range of the beams inside the BBO crystal.

From the beam geometry, we can calculate the beam converge angle ($\theta_{beam}$ = 0.033 rad) and the angle each beam is from the optical axis ($\theta$ = .1 rad). The spot size at the focus can be calculated to be

$$w_0 = \frac{\lambda}{\pi\theta_{beam}} = 7.77\,\mu m \qquad (11.6)$$

Where $\lambda$ is the wavelength equal to 810 nm. From this we can calculate the Rayleigh range using equation (11.2) to get $Z_R$ =0.234 mm. These values can now be used to calculate the active length using equation (11.5) to yield $L$ = 0.1642 mm. This interaction length can then be used to calculate the phase matching bandwidth. Note that spherical aberration and non-paraxial

imaging effects have been ignored in this analysis which is a reasonable approximation since the signal and input beams are close to the optical axis and imaged using a lens with an f number of 6.

The phase mismatch between the generated second harmonic light and the signal and reference beam is [42]

$$\Delta k = \frac{2\omega_0}{c}[n(2\omega) - n(\omega)] \tag{11.7}$$

where $\omega_0$ is the input frequency, c is the speed of light, $n(2\omega)$ is the index of refraction for the doubled frequency and $n(\omega)$ index of refraction for the input frequency. Convert this to a function of wavelength using the relation

$$\omega = 2\pi \frac{c}{\lambda} \tag{11.8}$$

This yields the expression for phase mismatch as a function of wavelength

$$\Delta k = \frac{4\pi}{\lambda_0}[n(\lambda_0) - n(\lambda_0/2)] \tag{11.9}$$

Consider what the phase mismatch will be at $\lambda=\lambda_0+\delta\lambda$. Keep in mind that for a given change in wavelength $\delta\lambda$ there will only be a change of $\delta\lambda/2$ in the second harmonic signal so the phase mismatch becomes

$$\Delta k = \frac{4\pi}{\lambda_0}[n(\lambda_0) + \delta\lambda \frac{dn(\lambda_0)}{d\lambda} - n(\lambda_0/2) - \frac{\delta\lambda}{2}\frac{dn(\lambda_0/2)}{d\lambda}] \tag{11.10}$$

If it is assumed that the process is phase matched at $\lambda_0$, then $n(\lambda_0)-n(\lambda_0/2) = 0$ and the above equation simplifies to

$$\Delta k = \frac{4\pi\delta\lambda}{\lambda_0}[\frac{dn(\lambda_0)}{d\lambda} - \frac{1}{2}\frac{dn(\lambda_0/2)}{d\lambda}] \tag{11.11}$$

The intensity of the generated second harmonic signal is

$$I_{2\omega} = \Gamma^2 I^2 \omega_0 L^2 \sin c^2(\frac{\Delta kL}{2}) \tag{11.12}$$

where $I$ is the intensity of the input, $L$ is the interaction length and $\Gamma$ contains constants that scale the intensity correctly such as the effective nonlinear coefficient for BBO [42]. The phase matching bandwidth can now be calculated from this intensity by finding what wavelength causes this peak intensity to be attenuated by a factor of 2. This yields half of the FWHM. By doing this for both sides of the center, the FWHM can then be calculated. To do this, consider the argument of the sinc squared function. Solve for what value of the argument of the sinc squared function is equal to 0.5 ((sin(1.39)/1.39)^2 =0.5). This means we have half the intensity when the argument of the sinc squared function becomes

$$\frac{\Delta kL}{2} = 1.39 \tag{11.13}$$

To solve for the phase matching bandwidth of the BBO crystal, set the phase mismatch when $\lambda=\lambda_0+\delta\lambda$ and solve for $\delta\lambda$. This occurs when the intensity is at half yielding

$$\frac{4\pi\delta\lambda}{\lambda_0}[\frac{dn(\lambda_0)}{d\lambda} - \frac{1}{2}\frac{dn(\lambda_0/2)}{d\lambda}] = \frac{1.39\square 2}{L} \tag{11.14}$$

$$\delta\lambda = \frac{1.39\square 2}{4\pi L}\frac{\lambda_0}{[\frac{dn(\lambda_0)}{d\lambda} - \frac{1}{2}\frac{dn(\lambda_0/2)}{d\lambda}]}. \tag{11.15}$$

Finally, as mentioned before, to turn this into FWHM we must double it ($\delta\lambda$ is only one side away from $\lambda_0$).

$$\delta\lambda_{FWHM} = \frac{2\square 1.39\square 2}{4\pi L}\frac{\lambda_0}{[\frac{dn(\lambda_0)}{d\lambda} - \frac{1}{2}\frac{dn(\lambda_0/2)}{d\lambda}]} = .442\frac{\lambda_0}{L}\frac{1}{[\frac{dn(\lambda_0)}{d\lambda} - \frac{1}{2}\frac{dn(\lambda_0/2)}{d\lambda}]} \tag{11.16}$$

To calculate how the index of refraction varies as a function of wavelength we need the Sellmeier equations for a BBO crystal [48]

$$n_o^2(\lambda) = 2.7359 + \frac{0.01878}{\lambda^2 - 0.01822} - 0.01354\lambda^2$$
$$n_e^2(\lambda) = 2.3753 + \frac{0.01224}{\lambda^2 - 0.01667} - 0.01516\lambda^2 \qquad (11.17)$$

Where λ is in microns. Solve for *n* and take the derivative with respect to wavelength to get the relation

$$\frac{dn_o(\lambda)}{d\lambda} = \frac{1}{2}\left(2.7359 + \frac{0.01878}{\lambda^2 - 0.01822} - 0.01354\lambda^2\right)^{-\frac{1}{2}}\left[-\frac{0.01878}{(\lambda^2 - 0.01822)^{-2}}2\lambda - 2\square 0.01354\lambda\right] \qquad (11.18)$$
$$\frac{dn_e(\lambda)}{d\lambda} = \frac{1}{2}\left(2.3753 + \frac{0.01224}{\lambda^2 - 0.01667} - 0.01516\lambda^2\right)^{-\frac{1}{2}}\left[-\frac{0.01224}{(\lambda^2 - 0.01667)^{-2}}2\lambda - 2\square 0.01516\lambda\right]$$

The second harmonic light will use the ordinary index of refraction $n_0$ while the fundamental will use the extraordinary index of refraction so we need to solve

$$\frac{dn_o(\lambda/2)}{d\lambda} = \frac{dn_o(0.405)}{d\lambda} = \text{-}0.0034$$
$$\frac{dn_e(\lambda)}{d\lambda} = \frac{dn_e(0.810)}{d\lambda} = \text{-}0.0096 \qquad (11.19)$$

Use these values to calculate the FWHM of the phase matching bandwidth

$$\delta\lambda = .442\frac{\lambda_0}{L}\frac{1}{\left[\frac{dn(\lambda_0)}{d\lambda} - \frac{1}{2}\frac{dn(\lambda_0/2)}{d\lambda}\right]} = \left|.442\frac{.810}{164}\frac{1}{\left[-0.0096 + \frac{1}{2}0.0034\right]}\right| = 262nm \qquad (11.20)$$

The absolute value is taken since only the magnitude of the difference between the dn/dλ values is needed. The calculated phase matching bandwidth (262 nm) is 26 times broader than the bandwidth of our pulse shaper output (10 nm FWHM) so the full output is measured. This means the measured SHG signal from the cross correlation is an accurate representation of the signal being measured by the reference. Or to put this another way, the spectral filter function

$H(\Omega)$ [42] that represents the SHG process is sufficiently broad in comparison to the signal so there is minimal distortion in the measurement.